Towards Robust and Scalable Supercooling for Sub-Zero Ice-Free Biopreservation

By

Tony Consiglio

A dissertation submitted in partial satisfaction of the

requirements for the degree of

Doctor of Philosophy

in

Engineering – Mechanical Engineering

in the

Graduate Division

of the

University of California, Berkeley

Committee in charge:

Professor Boris Rubinsky, Chair
Professor Costas Grigoropoulos
Professor Ahmad Omar

Summer 2023

Towards Robust and Scalable Supercooling for Sub-Zero Ice-Free Biopreservation

Abstract

Towards Robust and Scalable Supercooling for Sub-Zero Ice-Free Biopreservation

By

Tony Consiglio

Doctor of Philosophy in Engineering – Mechanical Engineering

University of California, Berkeley

Professor Boris Rubinsky, Chair

Organ transplantation represents one of the greatest medical advancements of the past century and is often the final option for patients suffering from end-stage organ disease. Despite our ability to perform these lifesaving operations, our simple inability to preserve organs for extended periods during *ex vivo* handling has caused immense logistical constraints that result in a majority of otherwise healthy donor organs not being transplanted. The current clinical standard for organ preservation, static cold storage, takes advantage of the Arrhenius temperature dependence of metabolism by placing organs on ice in order to slow expiration but enables just a few hours of viable preservation. Lower temperatures could further suppress metabolism and extend preservation, however ice crystallization results in irreversible damage.

Being an activated process, freezing does not occur immediately at the equilibrium phase transition temperature, allowing water to remain metastably supercooled below 0°C. By preserving an organ in a supercooled state, the metabolism suppressing benefits of lower temperature can be attained while entirely avoiding ice formation. Ice crystallization is initiated by heterogeneous nucleation however, which is an inherently random process whose rate scales unfavorably with temperature, volume, and supercooled duration. This unpredictability poses significant challenges to the advancement and ultimate clinical translation of supercooled preservation techniques.

This thesis has two primary objectives. The first is to identify methods, such as aspects of device and preservation solution design, that increase stability of supercooled systems. This involves both the development of new experimental tools necessary for probing supercooling stability and accompanying mathematical models for contextualizing key observations, such as the effect of rigid confinement. The second objective is to develop models to characterize the inherent stochastic nature of heterogeneous nucleation. These models enable prediction of freezing probability as a function of temperature, supercooled duration, volume, and solution composition. Ultimately, by applying engineering methods to understand the underlying molecular processes and model stochastic nucleation processes, these efforts establish a framework that enables the rational design of robust supercooled preservation protocols.

To my family.

Table of Contents

List of Figure Descriptions

List of Table Descriptions

Acknowledgements

Over the course of my studies, which span the better part of the past decade, I have become intimately familiar with the role of random chance in both science and daily life. Just as supercooling is enabled by the inherent stochastic nature of nucleation, the path I've taken has been marked by many unpredictable turns. Despite this pervasiveness of chance, I undoubtedly owe an enormous debt to the unwavering and enduring support of many friends, family, peers, and mentors. Without their presence in my life, none of this would have been possible. Thank you.

Chapter 1

Introduction

1.1 The promise and challenges of supercooled biopreservation

More than 700,000 deaths annually in the US are attributed to end-stage organ disease (ESOD), wherein an organ such as the heart, liver, kidney, pancreas, etc. is no longer able to provide life sustaining function [1]. Organ transplantation is often the final option for patients suffering from ESOD and represents one of the great medical advances of the past century. Despite our ability to conduct these lifesaving operations, it is estimated that globally only 10% of the need for organ transplantation is met [1]. Ranking near the top of the many factors responsible for this shortage is our simple inability to preserve donor organs for sufficient periods of time between procurement from the donor and transplantation in the recipient. This logistical challenge results in a large portion of otherwise healthy donor organs not being transplanted. In the absence of current supply constraints, it is estimated that greater than 30% of deaths in the US could be substantially postponed [2].

Taking advantage of its Arrhenius temperature dependence, organ preservation has generally involved the use of low temperatures in order to suppress metabolic activity and prevent deterioration during *ex vivo* handling. Static cold storage on ice is the most widely employed method for solid organ preservation and enables storage durations on the order of a few hours for most solid organs [1]. Preservation at lower temperatures could theoretically suppress metabolism further and enable longer periods of viability, however, water tends to freeze below 0°C and ice crystallization is known to cause excessive damage to biological systems [3].

Freezing is a first-order liquid to solid phase transition that begins with the process of nucleation. In the absence of impurities, water can be supercooled to temperatures below -30C before the nucleation of ice [4]. This scenario is termed homogeneous nucleation and generally does not occur since most volumes of water contain large numbers of minute impurities. These impurities reduce the energetic barrier of ice nucleus formation and can result in nucleation at much higher temperatures. For instance, certain proteins and macromolecules are unusually efficient nucleating agents and can initiate freezing just below 0°C [5], [6].

The tendency of water to unpredictably freeze below its equilibrium phase transition temperature has led historically to the development of sub-zero preservation techniques that leverage equilibrium effects to lower the equilibrium freezing point [7], ameliorate the damage of ice crystallization [8], [9], or achieve stability through glass formation at cryogenic temperature (i.e. through vitrification) [10]. The first application of metastable supercooling for the preservation of biological systems spawned from efforts to study the kinetics of ice nucleation

during cooling and freezing of cells [11]–[16]. These studies prepared cells in aqueous-oil emulsions to reduce the likelihood for heterogeneous nucleation and achieve stable supercooling. Much of the subsequent studies continued to focus on cells due the challenges associated with supercooling larger volumes; however, a handful of recent studies have begun investigating supercooling in full organs [17], [18].

Ultimately, driven by random molecular fluctuations, nucleation is inherently stochastic, not occurring at the same temperature or time in independent and identical samples. The presence of uncharacterized impurities possessing varying abilities for catalyzing heterogeneous nucleation imparts an additional level of randomness. The combined unpredictability represents the greatest barrier to clinical translation of supercooled preservation. In light of this, the focus of this thesis is to develop methods to enhance supercooled stability and estimate freezing probability.

1.2 Organization of the thesis

This thesis is organized into three main sections. Chapter 2 presents three studies that attempt to probe and understand the limit of stability in supercooled systems. Section 2.1 presents a mathematical model of ultrasonically driven bubble cavitation, a principal destabilization mechanism in supercooled systems. This study unifies divergent aspects of bubble dynamics, thermodynamics, and nucleation theory to explore the influence of confinement on cavitation-induced nucleation. This section is based on work presented in reference [19]. Section 2.2 presents an experimental campaign which aimed to identify methods for improving the stability of supercooling of aqueous solutions and to characterize this stability. This section is based on work presented in reference [20]. Section 2.3 presents a follow up study that leverages the systems and methods developed in the study of Section 2.2 in order investigate the influence of a carbohydrate polymer on supercooling stability. This section is based on work presented in reference [21].

Chapter 3 of this thesis presents two studies aimed at developing statistical models for informing the rational design of supercooled biopreservation protocols. In Section 3.1, nucleation statistics are combined with models for the temperature dependence of the metabolic rate in order to estimate the additional metabolic reduction that can be achieved at supercooled temperatures with minimal probability for freezing. This section is based on work presented in reference [22]. In Section 3.2, a statistical model of heterogeneous nucleation is developed, which accounts for the two primary sources of randomness: molecular stochasticity and random heterogeneous catalysis. This study enables prediction of supercooling stability in arbitrary systems as a function of temperature, volume and supercooled duration. This section is based on work presented in reference [23].

Chapter 4 concludes this thesis by contextualizing the five principal studies presented and offering perspectives on the extension of this work and potential impacts for clinical translation of supercooling technology.

Chapter 2

Investigations into supercooling stability

This chapter presents three studies that investigate methods for enhancing the stability of supercooled aqueous systems. Section 2.1 presents a mathematical model of cavitation, a principle destabilizing mechanism, in rigidly confined systems. Sections 2.2 and 2.3 present the development of an experimental platform for conducting nucleation experiments. This platform enables the investigation of the effect of different system parameters and configurations such as thermodynamic boundary condition and surface coating, as well as various solutes on nucleation kinetics.

2.1 Suppression of cavitation-induced nucleation in systems under isochoric confinement

2.1.1 Motivation of this study

Efforts to mediate the nucleation of solid phases in supercooled liquids are ubiquitous in fields ranging from materials science [24] to food science [25], and nucleation suppression has recently emerged as an essential route towards long-term organ and tissue preservation [26]–[28]. Nucleation is difficult to avoid in mobile or industrial contexts however [29], because acoustic agitations of any kind can cause the liquid phase to cavitate, resulting in ultrarapid, high-pressure nucleation events[30], [31]. Here, we explore the effects of isochoric (constant-volume) confinement on the cavitation dynamics and nucleation kinetics of aqueous systems exposed to ultrasonication, one of most reliable sources of rapid nucleation [32]. We unify bubble dynamics, thermodynamics, and classical nucleation theory to demonstrate that confinement across multiple volume scales can dramatically decrease peak cavity collapse pressures and dampen cavitation-induced nucleation under a wide range of operating conditions. Furthermore, we demonstrate the existence of a critical confinement volume, on the order of 10^8 times larger than the cavitating bubble itself, beneath which cavitation-induced nucleation becomes entirely kinetically prohibited. Our results reveal fundamental insights into the effects of confinement on kinetic phase change processes, and suggest that confinement could provide a compelling route towards high-stability supercooling.

Mechanical and acoustic stimuli have long been known to induce ice nucleation[33], and the works of Hickling[30], [31] clarified the mechanism to be the collapse of cavitating bubbles within the liquid. Collapse events occur over the span of nanoseconds, and can cause local pressure excursions on the order of several gigapascals in the surrounding medium. In low-thermal-diffusivity media such as water, this dynamic compression is sufficiently rapid to be considered

quasi-isentropic [7], and will result in liquid water rapidly traversing the equilibrium domains of several high-pressure ice polymorphs. Ice VII clusters will form almost instantaneously during such dynamic compression processes[31], [34], [35], and it is assumed that these short-lived clusters then serve as ultra-potent nucleation sites for ice-1h upon return of the water to its initial temperature and pressure[30], producing the macroscopic result of rapid ice-1h formation associated with sonic agitation of supercooled water[32].

Given the extreme consistency of cavitation-induced nucleation, ultrasonicated systems (which aggressively cavitate) provide an excellent platform for the study of nucleation suppression. In our recent experimental work[36], we observed that macroscopic volumes of supercooled water (~100 mL) confined in an isochoric container were resistant to nucleation via ultrasonication as well as other mechano-acoustic stimuli, suggesting the absence or dampening of cavitation-induced nucleation processes. In the present work, we conduct a fundamental analysis of the effects of multiscale confinement on cavitation-induced ice nucleation, and in the process uncover fundamental limiting behaviors relevant to cavity collapse, nucleation, and the broader spectrum of kinetic processes under confinement. We unify divergent aspects of bubble dynamics, thermodynamics and nucleation theory to explore the influence of confinement on cavitation-induced nucleation, a principal destabilization mechanism in supercooled systems. We demonstrate that confinement can suppress cavity collapse even in remarkably large systems and reveal the existence of critical volumes at which cavitation-induced nucleation becomes entirely kinetically prohibited, suggesting confinement as a compelling route towards modulation of kinetic phase change processes.

2.1.2 Cavitation dynamics in confined systems

In formulating this analysis, we must first acknowledge that the nucleation phenomena of interest are mathematically linked to cavitation via quasi-isentropic compression, the magnitude of which is dependent upon the pressure excursions encountered during cavity collapse. Thus, we begin by analyzing the dependence of cavity collapse dynamics on confinement.

We develop a modified spherical finite-domain Gilmore model [37] to describe the collapse dynamics of a single spherical air bubble of initial radius R_0 within a confined spherical body of water of radius R_c exposed to ultrasonic stimulation. A detailed derivation of the physical model is presented in Section 2.1.6 and results in an equation of the form

$$\left[-r\left(1-\frac{u}{c}\right)\frac{Du}{Dt}-\frac{3}{2}\left(1-\frac{u}{3c}\right)u^2+\frac{rc}{K}\left(1-\frac{u}{c}\right)\frac{Dp}{Dt}+\left(1+\frac{u}{c}\right)\int_{p_0}^{p}\frac{dp}{\rho}\right]_{R_b}^{R_c}=0 \tag{2.1}$$

which describes the motion of the liquid phase between the boundary of the cavitating bubble and the confined container, and reduces to the classical Gilmore equation in the limit of infinite container volume. Here, r is the radial coordinate, u is the radial velocity, p is the pressure, c is the speed of sound in the liquid, ρ is the density of the liquid, K is the bulk modulus of the liquid, and R_b is the transient bubble radius. The material properties of water are evaluated at the initial

bulk temperature of the system, according to the multiparameter equation of state maintained by the International Association for the Properties of Water and Steam (IAPWS)[38].

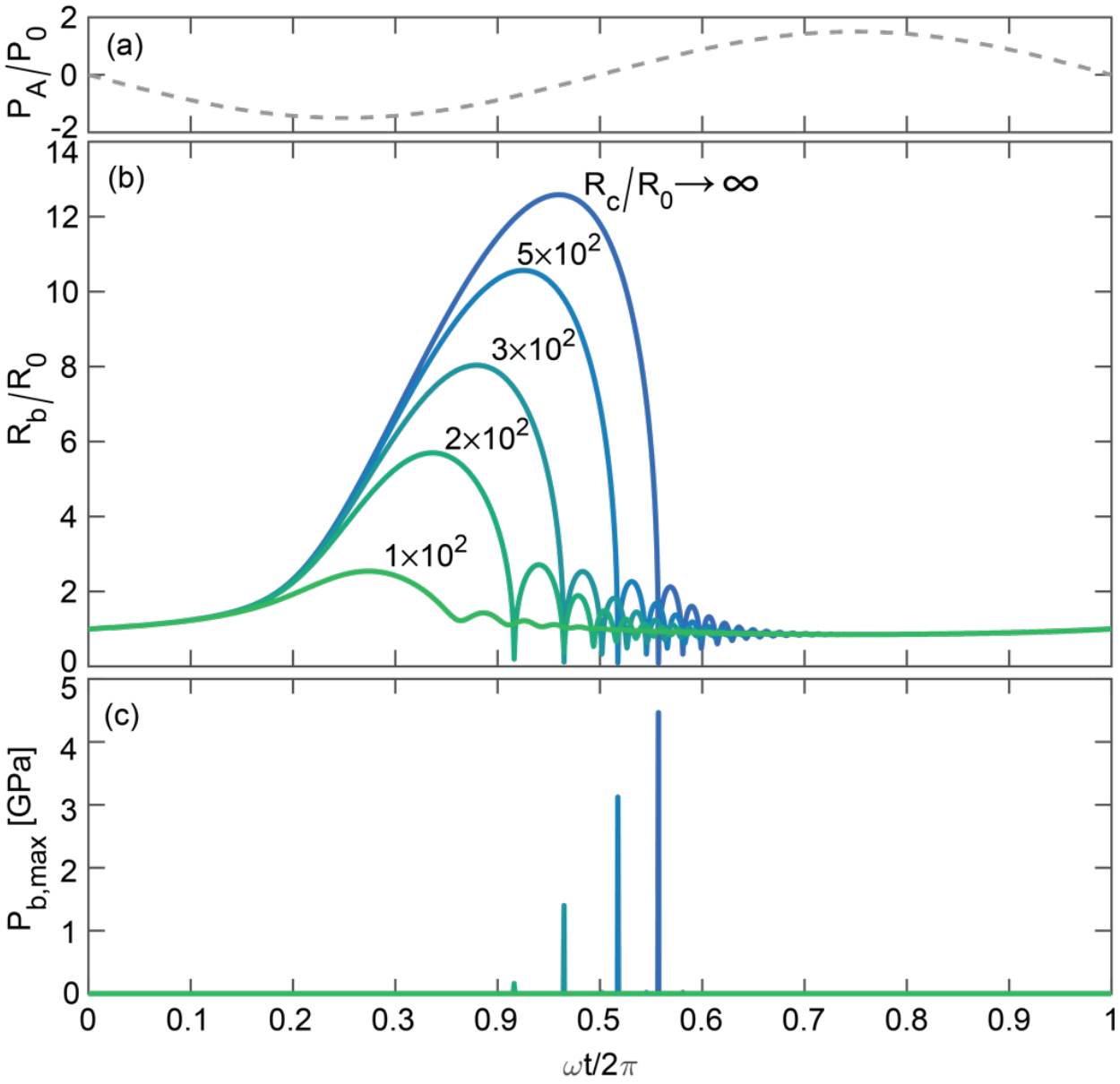

Figure 2.1: Transient excitation of a gas bubble in 0°C water under an ultrasonic pressure field. (a) Acoustic pressure signal of frequency 40 kHz and amplitude 1.5 bar as a function of cycle period, $\omega t/2\pi$. (b) Time evolution of relative bubble radius, R_b/R_0, for various values of relative confinement radius, R_c/R_0. Equilibrium bubble radius, $R_0 = 2.09\mu$m. (c) Pressure of water at bubble interface.

The resulting bubble growth and collapse dynamics are depicted in Figure 2.1 for varying confinement volumes. The bubble initially grows as tension is applied by the pressure field (shown in Figure 2.1a), reaching a maximum size following the point of minimum applied pressure. As the applied tension is then released, a force imbalance at the interface of the oversized bubble causes violent collapse (Figure 2.1b), during which the bubble radius may recoil to less than one tenth its equilibrium size. Given that the pressure within the bubble varies as $R_b{}^{-3\gamma}$ (in which γ is the ratio of specific heats for air), these collapse events result in brief periods (0.5 – 2 ns) of extreme pressure, as shown in Figure 2.1c.

The degree to which the system is confined (i.e. the ratio of the total confined system volume to the initial bubble volume) significantly alters bubble dynamics, acutely reducing the maximum bubble size reached and the peak pressure experienced during collapse (Figure 2.1b/c). Physically speaking, this reduction is driven by the finite compressibility of the confined liquid phase; as the bubble grows, the reduction of the volume occupied by water must be accompanied by an increase in hydrostatic pressure, which retards further growth of the bubble.

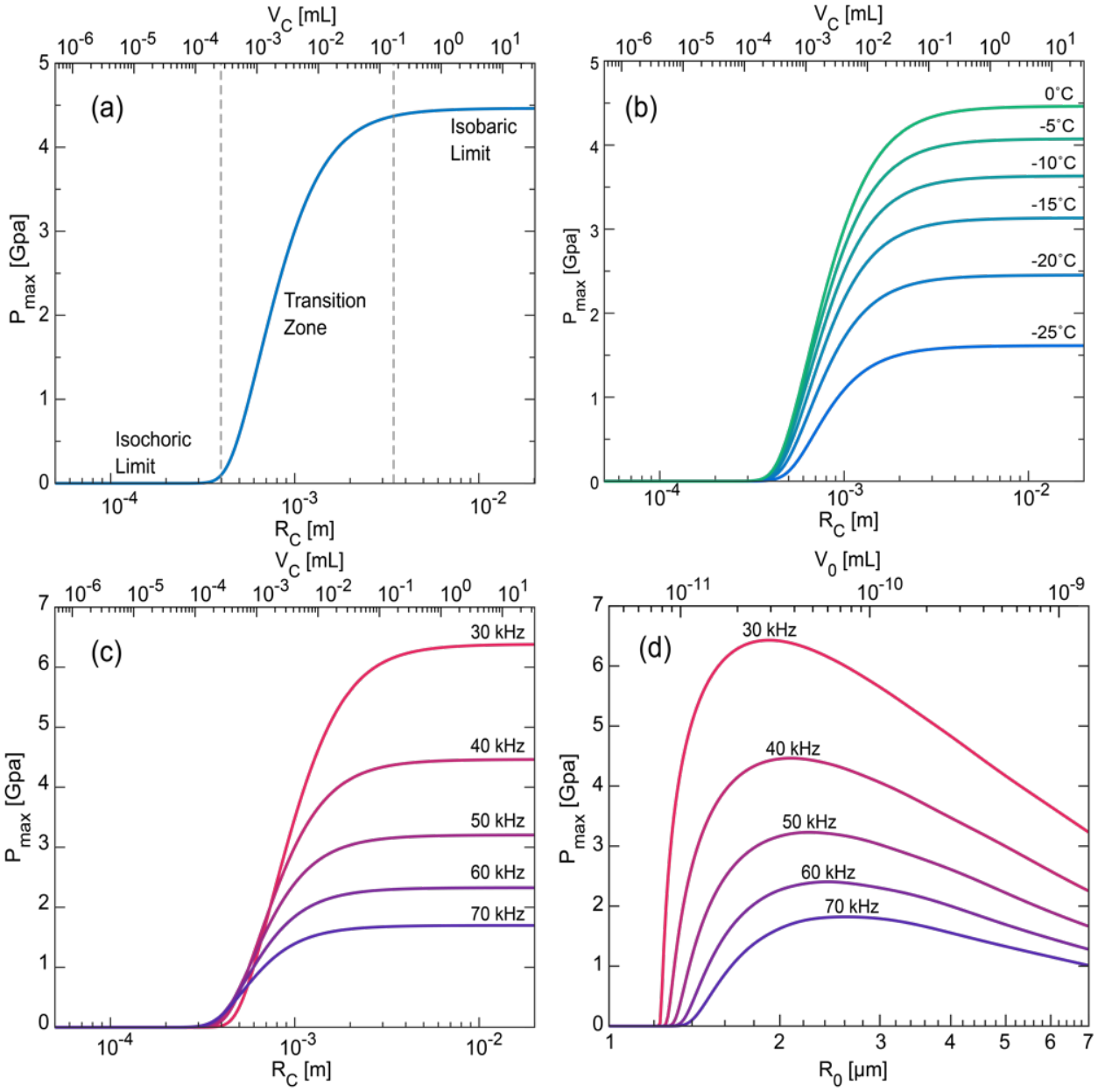

Figure 2.2: Peak collapse pressures experienced during cavitation in confined volumes. Curves are plotted for an excitation frequency of 30 kHz unless otherwise noted. (a) General dependence of maximum cavitation pressure on degree of system confinement. (b) Dependence of maximum cavitation pressure on degree of system confinement for varying degrees of bulk supercooling. (c) Dependence of maximum cavitation pressure on excitation frequency. (d) Dependence of maximum cavitation pressure on initial bubble radius at the isobaric limit of system confinement.

In Figure 2.2, the according effects of confinement on peak collapse pressure are demonstrated for varying system conditions, across which three distinct behavior regimes emerge (Fig. 2a). At the limit of infinite system volume, which is here approached at system volumes on the order of 10^{11} times greater than the initial bubble volume, the bubble dynamics are unaffected by the container. We term this volume scale the isobaric limit, as the results become equivalent to a system operating under unconfined isobaric conditions. It should be noted that this limit may increase somewhat (e.g. the effects of confinement may be felt at greater system volumes) as the initial bubble size is decreased, due to a relative enhancement of surface tension effects (See Section 2.1.7 for more detail).

As the degree of confinement increases (i.e. the container volume decreases), the bubble dynamics enter a "transition zone", in which the bubble begins to feel the effect of confinement and the peak collapse pressures begin to decline. The degree of confinement at which the transition zone is centered is dominated by the compressibility of the liquid phase, while the width of the transition zone is a weak function of the interfacial surface tension of the liquid, the ratio of specific heats of the gas, and the viscosity of the liquid. Neglecting time-dependent effects, the position of the transition zone can be probed by performing a simple force balance (derived in Section 2.1.7) at the bubble's maximum size, yielding the scaling relation:

$$K \ln\left(\frac{R_c^3 - R_{b,0}^3}{R_c^3 - R_{b,\max}^3}\right) + p_{l,0} = \left(p_{l,0} + \frac{2\sigma}{R_{b,0}}\right)\left(\frac{R_{b,0}}{R_{b,\max}}\right)^{3\gamma} - \frac{2\sigma}{R_{b,\max}} + P_A \tag{2.2}$$

in which K is the bulk modulus of the liquid, σ is the surface tension, $p_{l,0}$ is the initial pressure (atmospheric), P_A is a driving pressure, γ is the ratio of specific heats of the air, and $R_0, R_{b,max}$, and R_c are the initial bubble radius, maximum bubble radius, and confinement radius, respectively.

This scaling relation describes the approximate dependence of the maximum bubble radius on confinement, which serves as an effective first-order proxy for the peak collapse pressure and allows for convenient approximation of the order-of-magnitude confinement scales at which an arbitrary liquid with bulk modulus K and surface tension σ will start to see an arrest of cavitation dynamics. These scales are plotted for varying bulk moduli and surface tensions in Section 2.1.7, and the location and width of the water transition zone predicted by this simple relation demonstrate order-of-magnitude agreement with the full data presented in Figure 2.2.

The third and final regime depicted in Figure 2.2a, encountered at system volumes approximately 10^7 times larger than the initial bubble volume, demonstrates the existence of a critical confinement under which bubble collapse becomes entirely prohibited (as evidenced by the peak collapse pressure reducing to zero). Resistance from the rigid container prevents the bubble from reaching sufficient size to drive an unstable collapse event, and it instead merely oscillates stably in response to the applied pressure field (as in the bottommost profile in Figure 2.1b). We term this volume range the isochoric limit, and at confinement volumes in this regime, the system will experience no significant excursions in pressure.

The three regimes identified in Fig. 2a remain consistent as operational parameters are varied, though the discrete peak pressures encountered may change significantly. In particular, reduction

of the bulk system temperature significantly dampens collapse intensity (Figure 2.2b), due principally to the large increase in the viscosity of water at subzero centigrade temperatures, and reduction of the excitation frequency (Figure 2.2c) increases collapse intensity, due to an increased tensioning period in which the bubble is allowed to grow preceding collapse. The dependence of peak collapse pressure on the initial bubble size is also shown in Figure 2.2d, acknowledging that in an experimental context, a bubble field will exist with a distribution of cavitating bubble sizes. Throughout the collapse analyses presented in this work, the initial bubble radius that yields the highest collapse pressure for a given frequency is employed, ensuring description of the most extreme possible response.

2.1.3 Transient supercooling during cavity collapse

Using the results of Figure 2.2, we are now empowered to relate confinement to high-pressure transient ice nucleation by evaluating the quasi-isentropic thermodynamic path taken by the water surrounding the bubble during collapse. In Figure 2.3a, compression isentropes for water evaluated from multiple bulk system temperatures are plotted atop the H_2O phase diagram, allowing calculation of the temperature difference $\Delta T_{supercooling}$ between the compressed metastable liquid phase and the relevant equilibrium phase of ice as a function of pressure. This temperature difference is plotted in Figure 2.3b for various isentropes. As the water is compressed, it can pass through the equilibrium regions of up to five high pressure polymorphs of ice, with the most radical supercooling invariably occurring in the ice VII region.

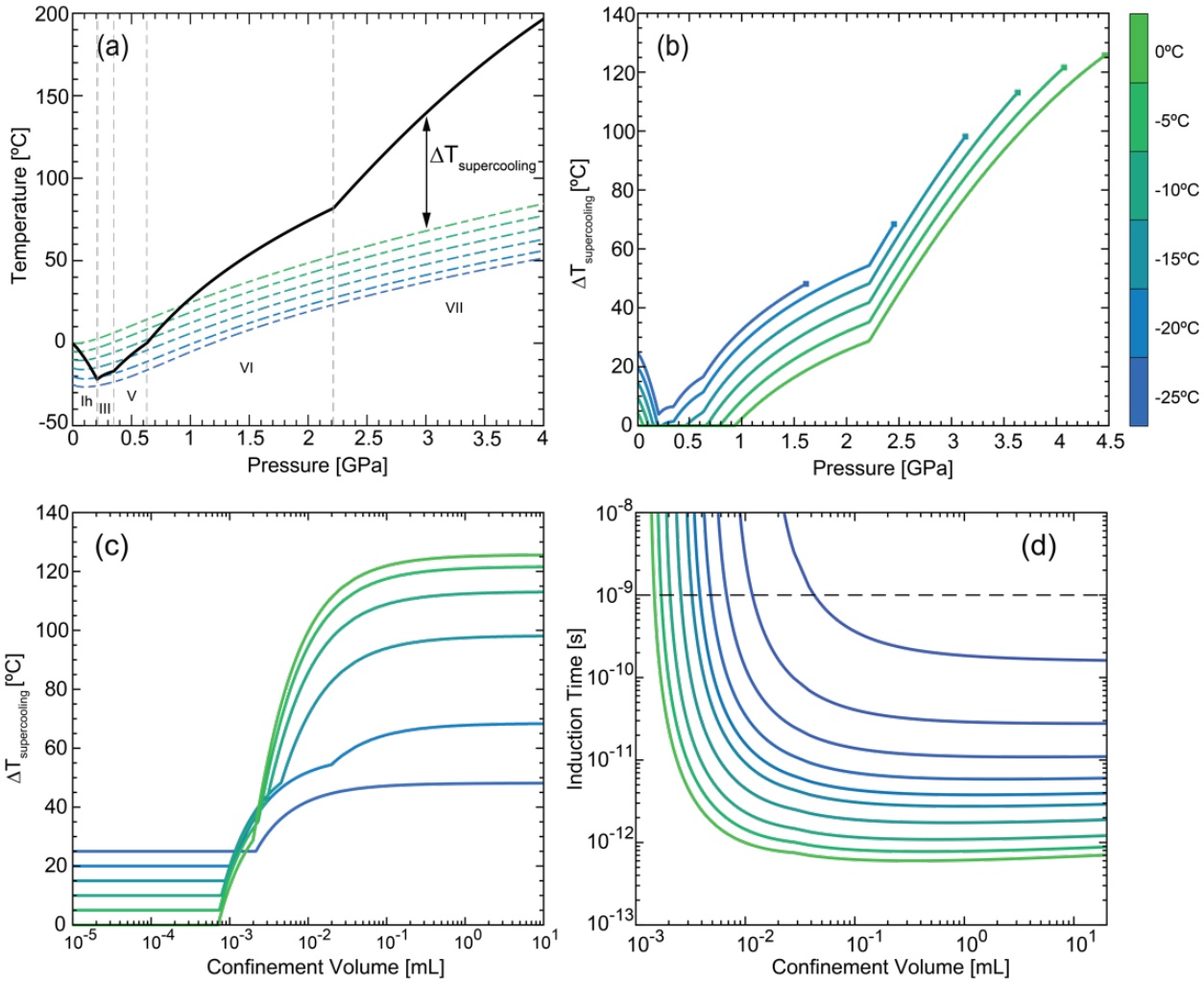

Figure 2.3: Transient high-pressure solidification processes for systems of varying bulk temperatures sonicated at 30 kHz. (a) Phase diagram of water with isentropic compression curves for bulk system temperatures of 0, -5, -10, -15, -20 and -25°C, color coded according to the color bar at right. The water-ice liquidus line (solid black) shows the equilibrium boundary between the liquid water phase (above the line) and the ice phases Ih, III, V, VI, and VII (below the line), as labelled along the bottom of the plot. Isentropic compression curves (dashed lines) show the temperature-pressure thermodynamic path followed by water as it is isentropically compressed from a varying initial temperature. As compression increases, the water will traverse through the equilibrium regions of several different ice phases. Both the liquidus line and the isentropic compression curves were calculated using the standard IAPWS multiparameter equations of state[38], [39]. (b) Magnitude of transient supercooling encountered during isentropic compression, e.g. the difference $\Delta T_{supercooling}$ between the liquidus curve and a given isentropic compression curve. Curves are truncated at the maximum pressure reached during cavity collapse for a given bulk temperature. (c) The same maximum transient supercooling as a function of confinement volume, adapted according to the pressure-confinement volume relations provided in

Figure 2.2. (d) Minimum ice VII induction time encountered during cavity collapse as a function of confinement volume, as calculated using classical nucleation theory. The dashed line represents the critical induction time threshold, defined by the average duration of a high-pressure collapse event (here 1 ns). Minimum ice VII induction times beneath this threshold will lead to formation of ice VII nuclei during cavity collapse, while induction times above the threshold will not.

By now combining the confinement-pressure results of Figure 2.2b with the pressure-supercooling results of Figure 2.3b, the maximum transient supercooling encountered at a given confinement volume can be calculated (Figure 2.3c), and the same confinement limits seen in the collapse pressure can be observed. At the isochoric limit, the maximum supercooling encountered in the system will simply be defined by the bulk system temperature, as no cavitation will occur. At the isobaric limit, significant cavity collapse pressures will drive $\Delta T_{supercooling}$ into the range of hundreds of degrees, principally in the ice VII region of the phase diagram.

Reduction of the maximum transient supercooling can be observed at remarkably large confinement volumes, on the order of 10^9 times larger than the bubble itself, and increases acutely over the volume range corresponding to the transition zone. Across confinement volumes, the maximum supercooling encountered is also a strong function of the bulk system temperature, though counterintuitively, increasing bulk supercooling decreases later cavitation-induced supercooling, due to increasing viscosity of water at low temperatures.

2.1.4 Effects on cavitation-induced nucleation

We now incorporate the transient supercooling results developed in Figure 2.3c into classical nucleation theory (CNT) and examine the induction time required for the nucleation of a high-pressure solid phase as a function of confinement. To simplify this analysis, we make the crucial assumption that the only high-pressure polymorph of ice likely to form during the quasi-isentropic compression process is ice VII, though each isentrope will briefly pass through regions in which ice V or ice VI may be more thermodynamically stable. This assumption is based on previous experimental observations of ice nucleation during quasi-isentropic dynamic shock compression, in which metastable ice VII was found to form preferentially to stable ice VI due its lower interfacial free energy[40], [41]. Furthermore, growth of ice VII has been observed at the same time scales as cavity collapse (~single nanoseconds)[35], [41], [42], and the relative degree of supercooling is highest in the ice VII region.

Using the Myint equation of state[43] to calculate the thermodynamic driving forces (e.g. the chemical potential difference) between compressed water and ice VII along each compression isentrope, CNT enables calculation of a transient induction time of the form

$$\tau = \frac{3k_B T \rho_{solid} \Delta G^*}{\pi^3 \sigma^2 \gamma} \tag{2.3}$$

which was originally formulated by Kaschiev[44] and adapted by Myint[34] to describe the time required for a cluster of ice VII particles to reach the critical size required for nucleation. In Equation (2.3), $k_B T$ is the thermal energy, ρ_{solid} is the molecular volume of ice, σ is the interfacial free energy between water and the growing ice VII phase, γ is a growth rate, and ΔG^* is the nucleation barrier (see Section 2.1.8 for full accounting of nucleation parameters).

Armed with the maximum supercooling encountered at a given confinement volume (Figure 2.3c) and the pressure-temperature paths followed during quasi-isentropic compression of the water, the fastest induction time possible at a given confinement volume can be calculated for various degrees of bulk supercooling (Figure 2.3d). The isobaric and isochoric limiting behaviors are once again observable: the induction time stabilizes to a minimum value at large system volumes, and it arcs toward infinity as the system volume decreases and the cavitation dynamics driving nucleation are extinguished.

In order to estimate whether cavitation-induced ice VII nucleation will ultimately occur, we can now compare the induction time required for the formation of a stable nucleus to the period over which the pressure excursion due to cavity collapse occurs. Previous experimental work has observed ultra-rapid formation of metastable ice VII at dynamic pressures as low as 1.8 GPa[40]; we thus examined the period over which the collapse pressure remained greater than or equal to this pressure, finding across bulk system temperature and frequency conditions a value of approximately 0.5 – 1.5 ns. This period can be applied as a critical threshold for the induction time of a high-pressure solid phase, and is plotted as a dashed line on Figure 2.3d. If the calculated induction time at a given confinement volume rests under this threshold, ice VII has a kinetic route to nucleation. If the induction time is above this threshold however (i.e. if it takes longer than ~1ns for a critical cluster of ice VII to form), the collapse pressure will dissipate before a stable nucleus can form, kinetically prohibiting cavitation-induced nucleation.

The discrete confinement volumes at which the induction time curves plotted in Figure 2.3d cross the collapse period threshold thus represent a critical phenomenon: the degree of confinement at which cavitation-induced nucleation becomes kinetically prohibited. This “critical confinement” volume can be plotted as a function of system parameters, herein the bulk temperature of the resting system and the driving frequency of the ultrasonication, to develop a kinetic phase diagram establishing the temperature - confinement boundary under which cavitation-induced nucleation will not occur for a given driving frequency (Figure 2.4).

The single-bubble analysis performed herein reveals several important consequences of system confinement: it can dampen bubble collapse dynamics, reduce transient supercooling during cavitation, and ultimately restrict cavitation-induced nucleation. Furthermore, there exist calculable critical confinement volumes at which discrete kinetic behaviors (bubble collapse, nucleation of high-pressure polymorphs) can be prohibited entirely. Perhaps most surprising however is the volume scale at which these myriad confinement effects come into play: For a single cavitation bubble on the order of 10^{-11} mL in volume, across sonication frequencies and bulk system temperatures, bubble collapse and cavitation-induced nucleation become kinetically prohibited at minimum critical confinement volumes on the order of 10^{-4} mL and 10^{-3} mL, respectively. From a physical perspective, this remarkable difference between the requisite system volumes for critical confinement and the cavitating bubble volumes is a manifestation of the large

compressibility difference between water and air (or more generally between generic liquids and gases); if the compressibility of the liquid medium surrounding the bubble increases, the observed difference in these volume scales lessens, consistent with the scaling relation provided in eq. 2 and plotted in the Figure 2.6.

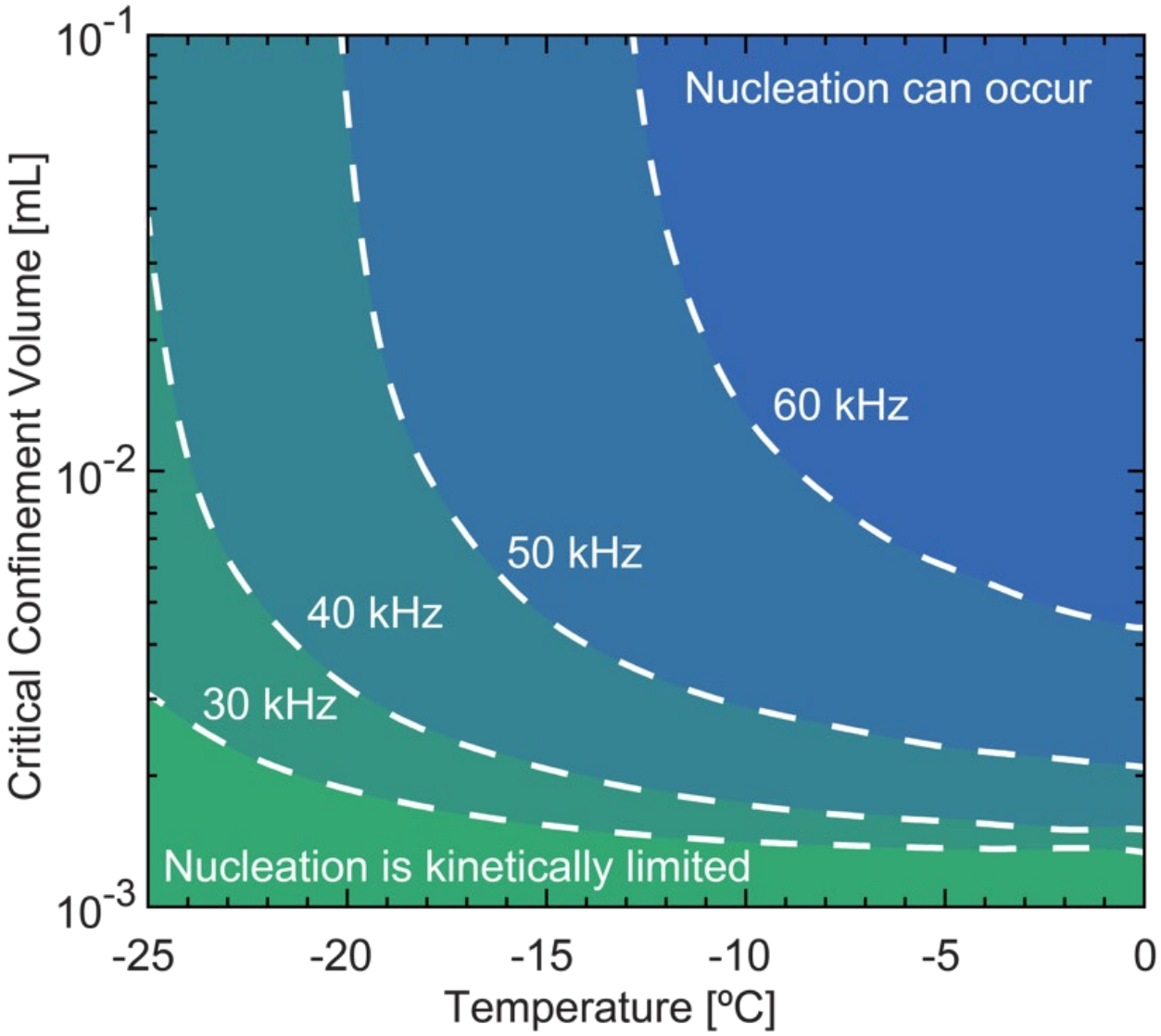

Figure 2.4: Ice VII kinetic phase diagram. The critical confinement volume for kinetic prohibition of ice VII nucleation is plotted as a function of temperature for various driving frequencies. Dashed lines indicate the boundary that separates the confinement regimes in which nucleation of ice VII can (above a given line) and cannot (beneath a given line) occur.

2.1.5 Discussion

These remarkably large single-bubble confinement volumes suggest that the observed confinement effects may also translate to bulk macroscopic systems, which produce large populations of simultaneously cavitating bubbles upon ultrasonication. For example, recent estimations of the number density of cavitating bubbles in water sonicated in the 20 – 200 kHz frequency range suggest that approximately 10^3 bubbles may cavitate per mL of liquid[45]. As a first-order approximation, if a hypothetical bulk system is ultrasonicated at 30 kHz and confined at 10 mL, the volume may be divided evenly by the number density of bubbles to arrive at an effective confinement volume per bubble of 10^{-2} mL, which is well within the transition zone for transient supercooling (Figure 2.3c) and approaching the critical confinement threshold for cavitation-induced ice VII nucleation (Figure 2.4).

It must be noted however that the critical confinement volumes calculated in this work describe only the most extreme possible cavitation scenario, in which the equilibrium size of the cavitating bubble corresponds to the peak displayed in Figure 2.2d, which will yield the greatest possible collapse pressure and the highest pursuant likelihood of ice VII nucleation. Experimentally, a cavitating bubble field in a macroscopic system will include a wide distribution of larger and smaller bubbles[45], which will inevitably produce significantly smaller pressure excursions upon collapse and reduce the likelihood of nucleation. Nucleation-suppressing confinement effects may thus potentially be observed at much larger scales than those considered here, and indeed in our recent proof-of-concept experimental investigation of nucleation in supercooled confined systems[36], suppression of nucleation was observed in macroscopically confined systems on the order of 100 mL that were supercooled to -3°C and ultrasonicated at 55 kHz. Although a full bubble field analysis is required to accurately extend the present model to experimentally relevant multi-bubble systems, the experimental findings described in[36] provide preliminary experimental confirmation of our proposed nucleation suppression mechanism, and future experimental efforts should not rule out confinement as a means of suppressing cavitation-induced effects at any scale. It should also be noted that the bubble number density, size distributions, and single-bubble peak collapse pressures may vary significantly for acoustic agitations other than ultrasonication, and future work should adapt the analyses presented herein to a variety of acoustic stimuli.

The need for robust control of ice nucleation has become increasingly clear in light of recent successes in medical supercooling[26], [27], which have yielded excellent biological results but have thus far not proven translatable outside a highly controlled laboratory environment[29]. Cavitation-induced nucleation of high-pressure polymorphs is the dominant mechanism by which supercooled systems are destabilized upon mechanical or acoustic perturbation (as occurs variously during transportation and clinical use), and thus any supercooling approach intended for practical use must work to suppress this mechanism.

Our results herein suggest that isochoric confinement can significantly hinder cavitation-induced nucleation, and, taken in combination with other recent works investigating the limiting effects of isochoric confinement on other ice nucleation and growth mechanisms[36], [46], [47], suggest that confinement may provide a compelling route toward robust nucleation suppression in supercooled systems. Future work should extend the single-bubble analyses developed herein to

full cavitating bubble fields, and in doing so establish a model for direct prediction of nucleation suppression effects in more complex macroscale cavitating systems.

2.1.6 Derivation of the cavitation model

Here we present the details of the mathematical model developed in the study to model bubble dynamics. The derivations presented follow the approach implemented by Gilmore[37], modified for consideration of a finite domain. The problem considered herein describes cavitation dynamics under confinement in an isochoric container subjected to an ultrasonic pressure field, enabling study of collapse effects as a function of container size. The mathematical formulation is defined by a single spherical bubble located at the center of a rigid, spherical vessel, as shown in Fig. 5.

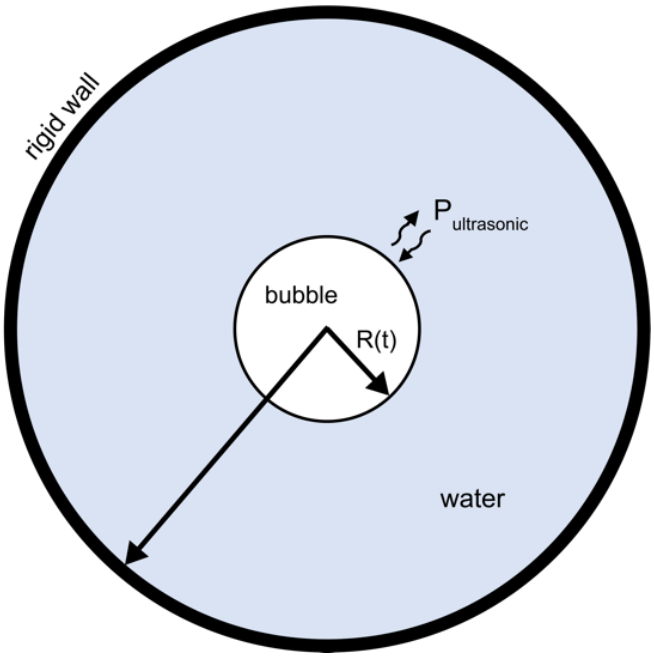

Figure 2.5: Schematic of spherical bubble within a rigid confinement

Radial, compressible flow is prescribed, and the gas inside the bubble is assumed to be spatially uniform. The effect of gravity and any initial temperature variations are neglected. Thus, the equations of motion describing the conservation of mass and momentum in the liquid are

$$\frac{1}{\rho}\frac{D\rho}{Dt}+\frac{1}{r^2}\frac{\partial(r^2u)}{\partial r}=0 \tag{2.4}$$

$$\frac{\partial u}{\partial t}+u\frac{\partial u}{\partial r}+\frac{1}{\rho}\frac{\partial p}{\partial r}=0 \tag{2.5}$$

where ρ is the density, u is the velocity and p is the pressure. The viscosity enters the problem solely as a boundary condition, as will be seen later, since viscous effects are confined to a thin boundary layer at the bubble surface and have been found to have a negligible effect on bubble dynamics[37], [48], [49].

The momentum equation is integrated from the liquid-gas interface at the bubble wall, R_b, to the container wall or confinement radius, R_c:

$$\int_{R_b}^{R_c} \left[\frac{\partial u}{\partial t} + u\frac{\partial u}{\partial r} + \frac{1}{\rho}\frac{\partial p}{\partial r}\right] dr = \int_{R_b}^{R_c} \frac{\partial u}{\partial t} dr + \left[\frac{1}{2}u^2 + h\right]_{R_b}^{R_c} \tag{2.6}$$

where the enthalpy at constant entropy, h, is given as

$$h = \int_{p_0}^{p} \frac{dp}{\rho}. \tag{2.7}$$

Using the definitions

$$\frac{1}{r^2}\frac{\partial (r^2 u)}{\partial t} = \frac{\partial u}{\partial t} + \frac{2u}{r} = \Delta_l \tag{2.8}$$

$$\frac{Du}{Dt} = \frac{\partial u}{\partial t} + u\frac{\partial u}{\partial r} \tag{2.9}$$

The remaining integral in Equation (2.6) can be reformulated by partial integration to obtain:

$$\begin{aligned} \int_{R_b}^{R_c} \frac{\partial u}{\partial t} dr &= \left[-r\frac{\partial u}{\partial t}\right]_{R_b}^{R_c} + \int_{R_b}^{R_c} r\frac{\partial \Delta_l}{\partial t} dr \\ &= \left[-r\frac{Du}{Dt} + ru\Delta_l - 2u^2\right]_{R_b}^{R_c} + \int_{R_b}^{R_c} r\frac{\partial \Delta_l}{\partial t} dr \end{aligned} \tag{2.10}$$

The remaining integral in Equation (2.10) can be evaluated by recognizing that the quantity $r\Delta_l$ is invariant in the acoustic approximation and thus satisfies the relation:

$$\frac{D(r\Delta_l)}{Dt} = \frac{\partial (r\Delta_l)}{\partial t} + c\frac{\partial (r\Delta_l)}{\partial r} = 0 \tag{2.11}$$

where c is the speed of sound in the liquid. Utilizing this, the integrated momentum equation can be assembled to yield:

$$\left[-r\frac{Du}{Dt}+r\Delta_l(u-c)-\frac{3}{2}u^2+h\right]_{R_b}^{R_c}=0 \tag{2.12}$$

From the continuity equation we find

$$\Delta_l=-\frac{1}{\rho}\frac{D\rho}{Dt}=-\frac{1}{K}\frac{Dp}{Dt} \tag{2.13}$$

In the barotropic approximation, pressure is only a function of density, $p=p(\rho)$, and is described by the relation

$$K=\rho c^2=\rho\frac{dp}{d\rho} \tag{2.14}$$

where K is the liquid bulk modulus and c is the speed of sound. Herein, K and c are evaluated at equilibrium conditions. Substituting this into Equation (2.12), we get

$$\left[-r\frac{Du}{Dt}+\frac{rc}{K}\left(1-\frac{u}{c}\right)\frac{Dp}{Dt}-\frac{3}{2}u^2+h\right]_{R_b}^{R_c}=0 \tag{2.15}$$

Gilmore [37] recognized that the Kirkwood-Bethe approximation, which assumes that the characteristic invariants propagate at a velocity of $(c+u)$, is more accurate for finite fluid velocities. By following the approach implemented by Flynn [48], we may compare the form of Gilmore's equation to Equation (2.15) and include three additional correction factors to yield

$$\left[-r\left(1-\frac{u}{c}\right)\frac{Du}{Dt}-\frac{3}{2}\left(1-\frac{u}{3c}\right)u^2+\frac{rc}{K}\left(1-\frac{u}{c}\right)\frac{Dp}{Dt}+\left(1+\frac{u}{c}\right)h\right]_{R_b}^{R_c}=0. \tag{2.16}$$

The enthalpy, h, as defined in Equation (2.7), is evaluated in terms of pressure

$$h=\int_{p_0}^{p}\frac{dp}{\rho}=\frac{K}{\rho_0}\left(1-\exp\left\{\frac{p_0-p}{K}\right\}\right). \tag{2.17}$$

To obtain an equation describing the motion of the bubble interface, Equation (2.16) and Equation (2.17) must be evaluated at the bubble wall and container wall. The boundary conditions satisfied by the liquid at the bubble wall, assuming no diffusion of gas through the interface, are

$$u(R_b, t) = \dot{R}_b \tag{2.18}$$

$$p(R_b, t) = P_g(t) - \frac{2\sigma}{R_b} - 4\mu\frac{\dot{R}_b}{R_b} + P_A \sin(\omega t) \tag{2.19}$$

where, R_b is the evolving bubble radius, σ is the surface tension of the gas-liquid interface, μ is the liquid viscosity, $P_g(t)$ is the pressure of the gas within the bubble, P_A is the amplitude and ω is the frequency of the imposed ultrasonic pressure disturbance. The over dot indicates d/dt.

Adopting a polytropic equation of state, the pressure within the bubble under adiabatic conditions is given by the relation

$$P_g(t) = \left(p_{l,0} + \frac{2\sigma}{R_{b,0}}\right)\left(\frac{R_{b,0}}{R_b}\right)^{3\gamma} \tag{2.20}$$

where γ is the ratio of specific heats, c_p/c_v. Since the container walls are assumed rigid, the liquid satisfies the condition

$$u(R_c, t) = 0. \tag{2.21}$$

It has been shown that large pressure variations due to bubble collapse during transient cavitation are only felt within a distance of few bubble radii from the bubble wall [30]. Thus, to a first-order approximation, it can be assumed that the density in the liquid varies uniformly due to the evolving bubble volume. Utilizing the relation from Equation (2.14), the pressure of the liquid at the container wall can written as

$$p(R_c, t) = K \ln\left(\frac{{R_c}^3 - {R_{b,0}}^3}{{R_c}^3 - {R_b}^3}\right) + p_{l,0} \tag{2.22}$$

where $R_{b,0}$ is the initial bubble radius and $p_{l,0}$ is the initial liquid pressure.

By evaluating Equations (2.16) and (2.17) utilizing the boundary conditions, a second-order nonlinear ordinary differential equation is obtained describing the time evolution of the bubble radius:

$$\left(1-\frac{\dot{R}_b}{c}\right)R_b\ddot{R}_b+\frac{3}{2}\left(1-\frac{\dot{R}_b}{c}\right)\dot{R}_b^2+\frac{R_c c}{K}\frac{DP_c}{Dt}-\frac{R_b c}{K}\frac{DP_b}{Dt}\left(1-\frac{\dot{R}_b}{c}\right)+h_c -\left(1+\frac{\dot{R}_b}{c}\right)h_b=0 \tag{2.23}$$

This equation can be readily numerically integrated to find the bubble radius as a function of time, $R_b(t)$. It is easily observed that in the limit of infinite confinement radius, the model reverts to the traditional Gilmore equation describing bubble dynamics in an infinite (isobaric) medium.

In the analysis described herein, the physical properties (viscosity, surface tension, density, speed of sound and bulk modulus) are evaluated at the initial bulk system temperature using values from the IAPWS R6-95(2018) formulation[38].

2.1.7 Transition Zone Scaling Analysis

As shown in Figure 2 of the main text, three regimes emerge when evaluating the dependence of the maximum pressure generated during cavity collapse on the degree of confinement. In the isochoric limit at sufficiently small confinement volumes, no significant pressure excursions are experienced. Conversely, at large confinement volumes, an isobaric limit is reached in which the bubble dynamics are unaffected by the rigid confinement and do not differ from an unconfined system. Between these two limits lies a transition zone that spans a few orders of magnitude in volume, in which the bubble dynamics begin to be affected by the rigid wall causing the peak collapse pressure to be suppressed.

Since the peak collapse pressure is integrally related to the maximum radius reached by the bubble during the growth period, the origin and behavior of the observed trends can be probed by performing a static force balance on the bubble at its point of maximum growth. During the tension phase of the ultrasonic stimulation, the ultrasonic pressure and pressure within the bubble (Equations (2.19) and (2.20)) are balanced by the pressure due to the compression of the water volume (Equation (2.22)). Taking the ultrasonic pressure to be equal to the driving pressure amplitude, the balance can be written as

$$K\ln\left(\frac{R_c^3-R_{b,0}^3}{R_c^3-R_{b,\max}^3}\right)+p_{l,0}=\left(p_{l,0}+\frac{2\sigma}{R_{b,0}}\right)\left(\frac{R_{b,0}}{R_{b,\max}}\right)^{3\gamma}-\frac{2\sigma}{R_{b,\max}}+P_A \tag{2.24}$$

Shown in Figure 2.6 is the normalized maximum bubble radius as a function of confinement radius for a range of values of liquid compressibility, K^{-1}, surface tension, σ, and initial bubble radius, $R_{b,0}$. The location of the transition zone is found to be dependent on the compressibility (K^{-1}), while the width of the transition zone is largely dependent on the surface tension (σ). Although this static scaling analysis does not include the effect of viscosity or sonic velocity, detailed analysis utilizing the full bubble dynamics model shows that viscosity has a similar effect to surface tension, though to a weaker degree, and that sonic velocity has a similar effect to

compressibility, which is expected due to their direct relationship (Equation (2.14)). The initial bubble radius ($R_{b,0}$) is also found to affect the transition zone: smaller bubbles experience the effect of confinement at larger relative container volumes. This may be attributed to the increased significance of surface tension, which scales with the surface area to volume ratio and is thus more dominant in smaller bubbles. This relationship can be observed in Figure 2.6b and Figure 2.6c. As the initial bubble size increases, this effect diminishes, and the relative critical confinement volume becomes independent of the initial bubble radius.

The scaling relation given in Equation (2.24) can be used to easily probe the discrete confinement volumes at which confinement effects will be seen for arbitrary liquid materials with known compressibilities and surface tensions.

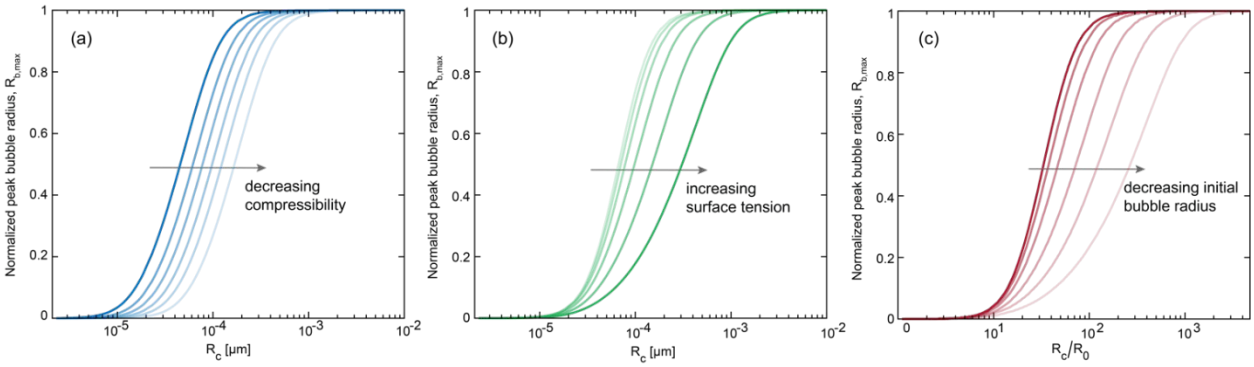

Figure 2.6: Dependence of transition zone on system parameters: (a) compressibility, K^{-1}; (b) surface tension, σ; (c) initial bubble radius, $R_{b,0}$.

2.1.8 Nucleation Parameters

This section provides a very brief explanation of the parameters used to calculate the induction time for ice VII via classical nucleation theory. The approach is identical to that applied by Myint et. al[34], who followed the initial derivations by Kashchiev[44], and more information can be found in those works.

The thermodynamic driving force for nucleation is the difference in the bulk chemical potential between the solid and liquid phases:

$$\Delta\mu = \mu_{\text{solid}} - \mu_{\text{liquid}} \tag{2.25}$$

We obtained temperature- and pressure-dependent chemical potential values for liquid water and ice VII from the equations of state developed by Myint et al [20]. This chemical potential difference $\Delta\mu$, which scales with volume and drives ice formation, is then compared to the interfacial free energy σ, which scales with surface area and resists ice formation, to identify the critical radius at which an incipient ice cluster will form a stable nucleus. This critical cluster radius is defined as:

$$R^* = \frac{2\sigma}{\rho_{\text{solid}} \Delta\mu} \tag{2.26}$$

In which ρ_{solid} is the density of the ice VII phase. The value of the interfacial free energy at a given cavitation pressure was calculated from a linear interpolation between the two reference points determined in Myint et al. [12], $\sigma = 23.0\ \text{mJ/m}^2$ at 1.58 GPa and $\sigma = 129\ \frac{\text{mJ}}{\text{m}^2}$ at 7 GPa.

The critical cluster radius is then employed in the definition of several other terms describing the size and behavior of a critical cluster, including:

The critical energy barrier to nucleation:

$$\Delta G^* = \frac{16\pi\sigma^3}{3\rho_{\text{solid}}^2 \Delta\mu^3} \tag{2.27}$$

The critical cluster size:

$$n^* = \frac{32\pi\sigma^3}{3\rho_{\text{solid}}^2 \Delta\mu} \tag{2.28}$$

The Zel'dovich factor, or the probability that a critical cluster will continue to grow, in which T is the temperature and k_{B} is the Boltzmann constant:

$$Z = \left(\frac{\Delta G^*}{3\pi k_{\text{B}} T n^{*^2}} \right)^{1/2} \tag{2.29}$$

The growth rate of the stable critical cluster, in which m is the molecular mass of the solid ice VII phase:

$$\gamma = \left(\frac{k_{\text{B}} T}{m} \right)^{1/2} \frac{\Delta\mu}{k_{\text{B}} T} \tag{2.30}$$

A frequency factor describing the attachment rate of new molecules to critical clusters, in which V_{solid} is the molecular volume of the ice VII phase:

$$D^* = \frac{4\pi R^{*^2} \gamma}{V_{\text{solid}}} \tag{2.31}$$

And the curvature at the top of the energy barrier:

$$\zeta = 2\pi k_B T Z^2 \tag{2.32}$$

Calculation of each of these parameters at a given temperature and pressure, starting from the bulk chemical potential difference, enables calculation of equation 3 in the main text, the induction time of a stable ice VII nucleus:

$$\tau = \frac{8k_B T}{\pi^2 \zeta D^*} \tag{2.33}$$

It should be noted that no arbitrary scaling factor has been applied to this induction time, as was done by Myint et al [11]. This results in our induction time calculation representing a conservative limit on the induction time of ice VII nucleation during cavity collapse (e.g. it provides the fastest possible induction time).

Equation (2.33) can be reformulated in terms of the nucleation barrier as

$$\tau = \frac{3k_B T \rho_{solid} \Delta G^*}{\pi^3 \sigma^2 \gamma}. \tag{2.34}$$

2.2 Methods to stabilize aqueous supercooling identified by use of an isochoric nucleation detection (INDe) device

2.2.1 Overview

Stable aqueous supercooling has shown significant potential as a technique for human tissue preservation, food cold storage, conservation biology, and beyond, but its stochastic nature has made its translation outside the laboratory difficult. In this work, we present an isochoric nucleation detection (INDe) platform for automated, high-throughput characterization of aqueous supercooling at >1 mL volumes, which enables statistically-powerful determination of the temperatures and time periods for which supercooling in a given aqueous system will remain stable. We employ the INDe to investigate the effects of thermodynamic, surface, and chemical parameters on aqueous supercooling, and demonstrate that various simple system modifications can significantly enhance supercooling stability, including isochoric (constant-volume) confinement, hydrophobic container walls, and the addition of even mild concentrations of solute. Finally, in order to enable informed design of stable supercooled biopreservation protocols, we apply a statistical model to estimate stable supercooling durations as a function of temperature and solution chemistry, producing proof-of-concept supercooling stability maps for four common cryoprotective solutes.

2.2.2 Motivation of this study

The stable equilibrium freezing point of liquid water, perhaps the most studied substance on Earth, is well known to be 0°C at atmospheric pressure. However, water may continue to exist in a metastable liquid state well below this temperature, and this phenomenon, termed supercooling, plays an integral role in numerous environmental[50], [51], biological[52], [53], medical[54]–[57], agricultural[58], [59], and industrial contexts[35], [60], [61]. Of particular interest, stable long-term supercooling has recently been deployed in a series of successful human organ and tissue preservation studies[54]–[57], providing a method of holding sensitive biologics at sufficiently low temperatures to arrest expiration whilst protecting them from lethal ice formation, which is essential to increasing the accessibility and efficacy of life-saving transplantation procedures[29], [62], [63]. However, despite the broad relevance of aqueous supercooling, it has thus far been minimally characterized at the bulk ($>$ 1 mL) volumes relevant to many applications, and as such, design of translatable supercooling protocols and devices has proven challenging.

The central challenge posed by the use of supercooling is the stochastic nature of ice formation[4]. At its core, nucleation of a solid phase is a kinetic process driven by random molecular fluctuations within a supercooled liquid—and thus while the point after which water *can* freeze can be rigorously defined as a single temperature (0°C), the point at which pure water *will* freeze is a complex statistical function of the supercooling temperature, the period for which it is held at this temperature, and the water's volume or surface area[64]–[66].

To complicate things further, ice may nucleate from supercooled water in one of two modes: homogeneous nucleation, in which the water becomes sufficiently cold to drive spontaneous ice

cluster formation in the liquid interior (occurring at approximately –40°C for pure water[67]–[70]), or heterogeneous nucleation in which the presence of foreign agents (particulate matter and surfaces[71]–[75], air bubbles[28], [76]–[78], etc.) reduces the kinetic barrier to ice formation and causes nucleation to occur at significantly higher temperatures. In aqueous systems of > 1 mL volume, nucleation proceeds nigh-exclusively by the heterogeneous mode, introducing a new potential dependence of any nucleation data on the materials with which the water is interfacing during a given experiment.

Given this stochastic and context-dependent nature of ice nucleation, a rigorous description of aqueous supercooling (sufficient to enable informed design of supercooling protocols) requires very high statistical power, necessitating tens-to-hundreds of trials for each condition probed. In order to achieve these sample sizes, the majority of aqueous supercooling studies have employed microliter-and-smaller water droplets, which are monitored optically or thermally in order to detect the onset of ice nucleation/ceasing of supercooling. These studies have precisely characterized several homo- and heterogeneous nucleation processes at the microscale, but have proven challenging to scale to larger volumes due to the scale-dependent confluence of volumetric and surface effects. In particular, droplet and other <1 mL-volume-based studies of heterogeneous nucleation are typically dominated by the role of the air-water interface as a potent nucleation site, as has been highlighted previously[79]. In bulk systems relevant to applied biopreservation however, evaluating simply by surface area of contact, the water-solid interface is much more likely to dominate heterogeneous effects, limiting the cross-over applicability of small-volume heterogeneous nucleation studies. Furthermore, thermodynamic size effects (e.g. surface tension and curvature effects[80]) may contribute meaningfully to droplet systems, but become negligible at bulk volumes, augmenting the difficulty in confidently scaling droplet studies.

Thus, in order to drive the characterization of aqueous supercooling at bulk volumes and ultimately design supercooling protocols relevant to bulk applications (such as biopreservation), supercooling studies must be performed directly on bulk-volume samples. However, this must be done without sacrificing the large sample sizes needed to secure sufficient statistical power to fully specify stochastic behaviors, and a significant technical challenge is thus presented.

In this work, we introduce the isochoric nucleation detector (INDe), an experimental platform which leverages the unique thermodynamics of isochoric systems to probe supercooling in bulk-volume aqueous media at high-throughput and high statistical power.

Over the past decade, isochoric (constant-volume) thermodynamic conditions, which are achieved by confining bulk water or solution in a rigid, high-strength container in the absence of air or any other highly compressible elements, have been demonstrated to affect the aqueous freezing process in various ways[46], [47], [81]. Most significantly, the phase equilibria that result under isochoric conditions are fundamentally different than those encountered under the conventional isobaric (constant pressure) conditions that exist when the system is open to the atmosphere. Instead of freezing entirely at sub-zero centigrade equilibrium, as is expected under isobaric conditions, an aqueous isochoric system will freeze only partially, achieving a two-phase equilibrium configuration in which the expansion of some portion of ice drives self-pressurization of the system, depressing the freezing point of the remaining portion of the system and maintaining it in a stable liquid state. This ultimate two-phase thermodynamic destination of the system not

only affects the final phase equilibria experienced, but also the kinetic nucleation and growth pathway taken to get there, and prior theoretical and experimental work has suggested that isochoric conditions may enhance the stability and reduce the variability of aqueous supercooling[36], [46], [82], thereby enabling not only potentially robust biopreservation and other practical applications, but reliable supercooling characterization at bulk volumes.

Herein we detail the electro-mechanical design of the INDe device and its thermodynamic operating principles and then employ it to conduct three studies investigating multiple factors that affect supercooling in aqueous systems, including thermodynamic boundary condition, surface coating and solution chemistry. Among several key findings, we demonstrate that isochoric conditions can indeed significantly enhance the depth and stability of aqueous supercooling relative to conventional isobaric conditions; that applying a hydrophobic coating to all surfaces in contact with the bulk liquid sample can further enhance aqueous supercooling regardless of thermodynamic condition, and that various common solutes will depress the maximum degree of supercooling possible by at least as much as their according freezing point depression. Finally, we deploy a Poisson-statistics model of nucleation to calculate the induction time of nucleation (i.e., the period that the supercooled liquid will remain stable) as a function of temperature for each solution using only our maximal supercooling data as an input, providing an essential tool for the informed design of supercooled biopreservation protocols. In total, this work demonstrates both the multifaceted utility of the INDe platform for nucleation analyses and several novel means of enhancing supercooling in aqueous systems.

2.2.3 Design of an Isochoric Nucleation Detector (INDe)

In order to study bulk-volume aqueous supercooling at high-throughput, we have designed a device that leverages the unique thermodynamic behaviors of aqueous systems confined under isochoric (constant-volume) to detect nucleation at low-latency without the need for scale-variant thermal or optical detection: the isochoric nucleation detector (INDe).

At the heart of the INDe, depicted in Figure 2.7, is a two-part isochoric (constant-volume) chamber constructed from Aluminum-7075, chosen for its preferable combination of high strength and high thermal conductivity. The chamber has an internal volume of 5mL and an inner diameter of 0.5”. A threaded plug with a tapered end forms a tight metal-on-metal seal with the corresponding mating surface on the chamber body, providing a sealed interior capable of withstanding pressures in excess of 200 MPa. This design feature further creates a continuous and homogenous interior surface that minimizes the potential for active nucleation sites and thus maximizes supercooling to the greatest extent possible. Flat exterior faces of the chamber allow it to be clamped between a pair of temperature control assemblies, each comprised of a two-stage thermoelectric module and standard fan-cooled CPU heat sink. To aid in temperature control and uniformity, the chamber is further surrounded by an insulation shell of 3D printed PLA plastic filled with expanding polyurethane insulating foam. Figure 2.13 shows several assembled INDe devices.

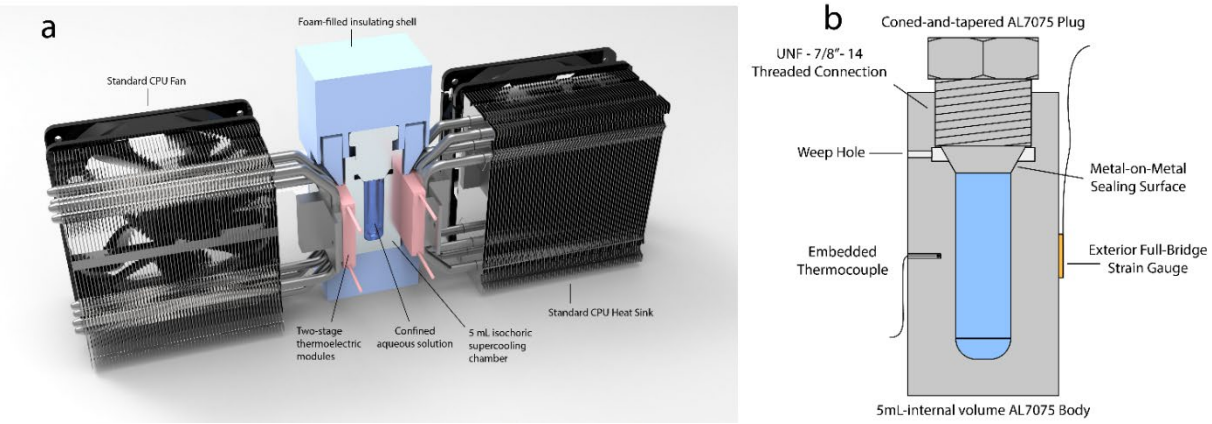

Figure 2.7: Schematic of the Isochoric Nucleation Detector (INDe). (a) 3D rendering depicting cutaway of INDe chamber, insulation shell and temperature control assemblies consisting of thermoelectric modules and fan-cooled CPU heat sinks. (b) 2D cutaway schematic of 5mL INDe isochoric chamber depicting sealing mechanism, embedded thermocouple and strain gauge.

2.2.4 Pressure-based nucleation detection

In traditional nucleation experiments, the nucleation events are often detected optically, by sensing the change in sample translucence[74], [83], or thermally, by detecting the release of latent heat[84], [85]. In metallic isochoric chambers, optical detection is not possible. Detection of the latent heat release is possible; however, in systems of milliliter scale or larger, the propagation of thermal energy from the nucleation site to the temperature sensor requires appreciable time and may thus lead to measurement uncertainty. In aqueous systems under isochoric conditions however, a third signature of ice nucleation exists: pressure. Due to the difference in density between ice and water, when ice begins to crystallize from supercooled aqueous media in a confined environment, its expansion generates significant hydrostatic pressure (up to approximately 210 MPa at –22°C)[47]. Thus, in an isochoric chamber, the detection of a pressure rise serves as an alternative method for nucleation detection. Furthermore, this pressure signal propagates through the sample at the speed of sound (approximately 1500 m/s in pure water), providing extremely low detection latency and affording easy scalability to increasingly large systems.

In order to detect the pressure signature of ice nucleation, a traditional pressure transducer may be employed; however, this can introduce undesirable material interfaces, undesirable complexity and expense, as well as potential compressibility issues, which may corrupt the desired isochoric conditions. Instead, the INDe, which is specifically designed to maximize supercooling stability, utilizes a high-sensitivity full-bridge strain gauge affixed to one of the exterior faces of the chamber (Figure 2.7b). Elevated pressure within the sealed isochoric environment causes the chamber to mildly elastically deform, which produces a clear spike in strain gauge signal. The

equivalence between direct detection of pressure and detection of strain was verified by simultaneously monitoring pressure and strain during a nucleation event. As shown in Figure 2.8c, the two signals are nearly coincident, with sub-one second latency. This simple strain detection method has proven to be highly sensitive, and because it is independent of chamber geometry, may be readily employed in isochoric systems of varying size.

On the face of the chamber opposite the strain gauge, a hole in which a type-K thermocouple is embedded, allows for measurement of the internal temperature (±0.2°C). A 3D thermal analysis, detailed in the SI, was performed to evaluate the temperature evolution of the aluminum chamber at the maximal cooling rates of interest to this work (2±0.5°C/min). The temperature of the chamber where the thermocouple is mounted was found to remain within 0.05°C of the interior chamber wall temperature, which itself is uniform across its surface area to within ±0.05°C. This uniformity is the most critical to interpretation of all nucleation results, because in bulk systems nucleation proceeds nigh-exclusively in the heterogeneous mode, starting at the chamber wall. The center temperature of the sample by comparison will lag somewhat behind the periphery in contact with the chamber walls (see SI for details), but is presumed not to contribute to observed nucleation phenomena due to the absence of homogeneous nucleation modes at temperatures higher than approximately –40°C.

2.2.5 Transient supercooling experiments in the INDe

Experiments to characterize supercooling are generally conducted in one of two modes: isothermal or transient. In the isothermal mode, the sample is quenched to and held at a single sub-freezing temperature, and the time required for ice to nucleate is recorded (this "induction time" is a fundamental characteristic of supercooling, and will be discussed in further detail in the coming sections)[58], [83], [86]–[88]. In the transient mode, the sample temperature is cooled continuously at a constant rate and the temperature at which nucleation occurs is recorded[74], [89]–[91]. This value, herein referred to as the nucleation temperature, represents the limit of stability at which the induction time approaches zero, or the maximal degree of supercooling possible.

From a theoretical standpoint, the isothermal method may be preferable, as it enables direct determination of the nucleation rate of the system, $J\left[\frac{\#\ of\ nuclei}{unit\ size * unit\ time}\right]$, which represents the most fundamental parameter employed in classical nucleation theory (CNT). However, this nucleation rate can vary many orders of magnitude with small changes in temperature[64], and the induction time may thus vary from the order of seconds to the order of years with only a few degrees change in temperature, posing a significant difficulty for laboratory experimentation (especially if trials are to be repeated tens or hundreds of times in order to establish sufficient statistical power). Thus, the transient method is much more practical for high-throughput experimentation, and while the INDe can be operated in both configurations, we conduct all experiments herein in the transient mode.

Transient supercooling experiments in the INDe begin by filling and sealing the isochoric chamber. Special attention is paid to excluding any air from the chamber during assembly, as the presence of any bulk gas phase can corrupt the desired isochoric conditions by introducing

increased compressibility[92], and because the gas-liquid interface may act as a potent nucleation site[28]. To form a reliable seal capable of withstanding elevated pressures, which may exceed 200 MPa if ice growth is allowed to proceed indefinitely, the plug is tightened to a torque of 45 ft-lbs. After loading, the sealed chamber is inserted into the insulation shell and secured between the temperature control assemblies.

Utilizing a custom-developed Python control dashboard, the temperature is decreased at a rate of 2±0.5°C/min via PID control of the thermoelectric modules. Cooling is continued until the onset of nucleation, which is indicated by a spike in the strain and autonomously sensed by the control software. The thermoelectric elements are then switched into heating mode and the temperature of the chamber is quickly brought back above 0°C and held for a specified time (here 5 minutes), after which the same plunge in temperature is repeated. This heating step arrests ice growth and enables the supercooling to be "reset" after each nucleation event, enabling continuous unmonitored cycling for tens or hundreds of independent nucleation events over the course of several hours.

Depicted in Figure 2.8a and Figure 2.8b are example raw temperature and strain data for several cooling and warming cycles. In Figure 2.8c we provide verification that the observed strain signal is, as expected, coincident with the increase in internal hydrostatic pressure, as measured by a digital pressure transducer. The base of the strain spike corresponds to the nucleation of ice from the supercooled liquid and establishes the time at which the nucleation temperature is determined. Figure 2.8d depicts the evolution of nucleation temperatures for a single experiment across 100 cycles (no statistically relevant trend is observed, as should be expected of a memoryless stochastic process), and Figure 2.8e shows a violin plot depiction of this same nucleation data capturing the stochastic distribution, median value, and range. The width of the violin plot is proportional to the number of nucleation events (i.e., nucleation probability) at the corresponding temperature. Figure 2.8f depicts the survivor curve or cumulative distribution function of this data, which describes the fraction of total cycles for which the sample did not freeze at a given temperature. For example, for the data shown, approximately 50% of trials remained unfrozen at –14.5°C. Each of these representations offers different insight into the statistical realities of nucleation in the target substance, with the survivor curve providing the ultimate limits of the observed nucleation probabilities. Further details on all performed statistical analyses are provided in the Methods section.

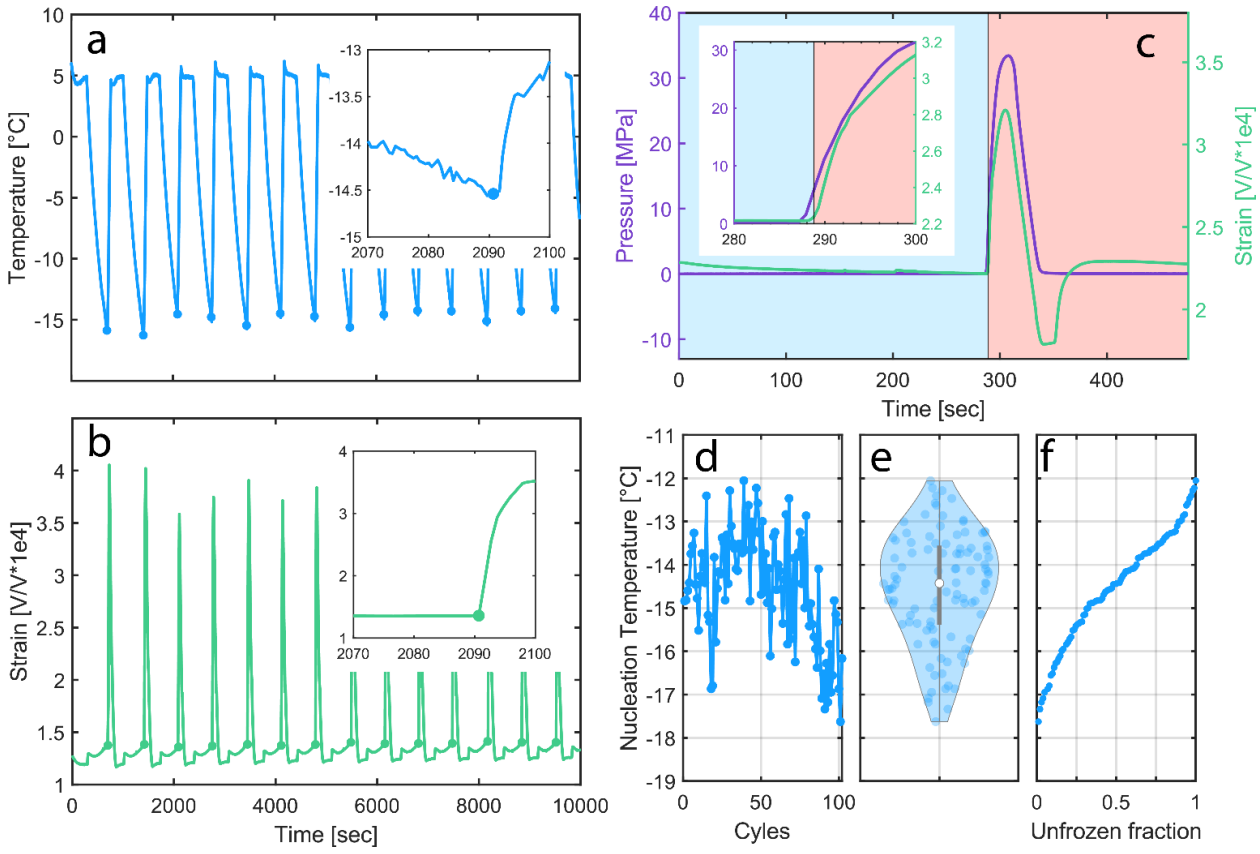

Figure 2.8: Example data obtained by the INDe. (a) Raw temperature curves for a series of cooling/warming cycles. Markers at bottom of saw-tooth indicate nucleation temperature. Inset depicts zoom-in on one nucleation event. (b) Corresponding raw strain curve. Spike in signal caused by nucleation of ice within isochoric chamber. Markers at base of spike indicate nucleation event. Inset depicts zoom-in on one nucleation event. (c) Validation of equivalence between pressure and strain monitoring for nucleation detection. Blue region indicates cooling period. Red region indicates warming period after detection of nucleation. (d) Representative extracted nucleation temperatures from one INDe experiment. (e) Violin plot representation of nucleation temperature distribution. (f) Survivor curve representation of nucleation temperature distribution.

2.2.6 Using the INDe to probe various factors affecting aqueous supercooling

Supercooling is a complex phenomenon affected by myriad factors, including thermodynamic boundary conditions, surface conditions, and system chemistry. The INDe provides a versatile platform for probing all of these aspects both independently and in concert, and in order to demonstrate the breadth of studies possible, we present three studies on differing factors affecting

aqueous supercooling, which culminate in the presentation of useful tools for the design of effective supercooled biopreservation protocols.

Effects of thermodynamic conditions and surface conditions on supercooling of pure water

Recent studies have suggested that isochoric conditions may enhance the supercoolability of aqueous solutions relative to conventional isobaric (constant pressure) conditions at atmospheric pressure. Powell-Palm et al.[36] demonstrated that supercooled isochoric systems exhibit enhanced stability against macroscopic agitations including vibration, ultrasonication, drop impact and thermal cycling, albeit at only a single mild supercooling temperature (–3°C). Further studies have also suggested that isochoric confinement may increase supercoolability by increasing the energetic barrier to nucleation and suppressing other kinetic nucleation mechanisms such as cavitation[46], [82].

In order to further probe the potential effects of isochoric confinement on supercooling, the INDe is employed here to characterize the supercooling limit of deionized water in three potential thermodynamic configurations: under isobaric conditions (in which the liquid is freely exposed to the atmosphere), under isobaric + oil-sealed conditions (in which the liquid is exposed to the pressure reservoir provided by the atmosphere, but is denied contact with air by an immiscible layer of oil), and under isochoric conditions (in which the liquid is denied access to the atmosphere entirely and is rigidly confined at constant volume). Isobaric experiments were performed in the same INDe chambers, yet with the plug removed, and in the oil-sealing trials, a layer of mineral oil was placed atop the water volume, as depicted in Figure 2.9a. Although ice nucleation in an isobaric system is not required to be accompanied by an increase in hydrostatic pressure, the strain gauges nonetheless produce a small yet distinct spike upon nucleation, likely due to rapid ice expansion in the narrow cavity. This signal proves sufficient for nucleation detection and is additionally supplemented by monitoring of the temperature rise due to the release of latent heat (which occurs within a second of the strain rise).

In addition to these varying thermodynamic conditions, we also probe the effect of two different surface conditions on pure water supercooling. As nucleation occurs heterogeneously in most real aqueous systems[4], [75], [93], countless studies have probed the effects of surface conditions on ice nucleation processes. In classical nucleation theory, the contact angle of the liquid phase on the containing surface captures the propensity of that surface to aid in heterogeneous nucleation, with lower contact angles (or hydrophilic surfaces) increasing the likelihood of nucleation and higher contact angles (or hydrophobic surfaces) decreasing the likelihood of nucleation[65]. Surprisingly however, while myriad studies have examined the supercooling of droplets on hydrophobic surfaces, to our knowledge no previous studies have probed the effect of fully containing > 1 mL volumes of water within hydrophobic walls. Thus, for each of the thermodynamic configurations mentioned above, we also probe the effect of coating the entire interior surface of the chambers with a thin layer of petrolatum, thus exposing it to exclusively hydrophobic surfaces.

For each condition, a minimum of 50 trials per chamber in three different chambers are performed, providing a minimum n = 150 data points. The results of these pure water experiments with both bare aluminum surfaces and hydrophobic petrolatum-coated surfaces are shown in Figure 2.9, and several conclusions can be made.

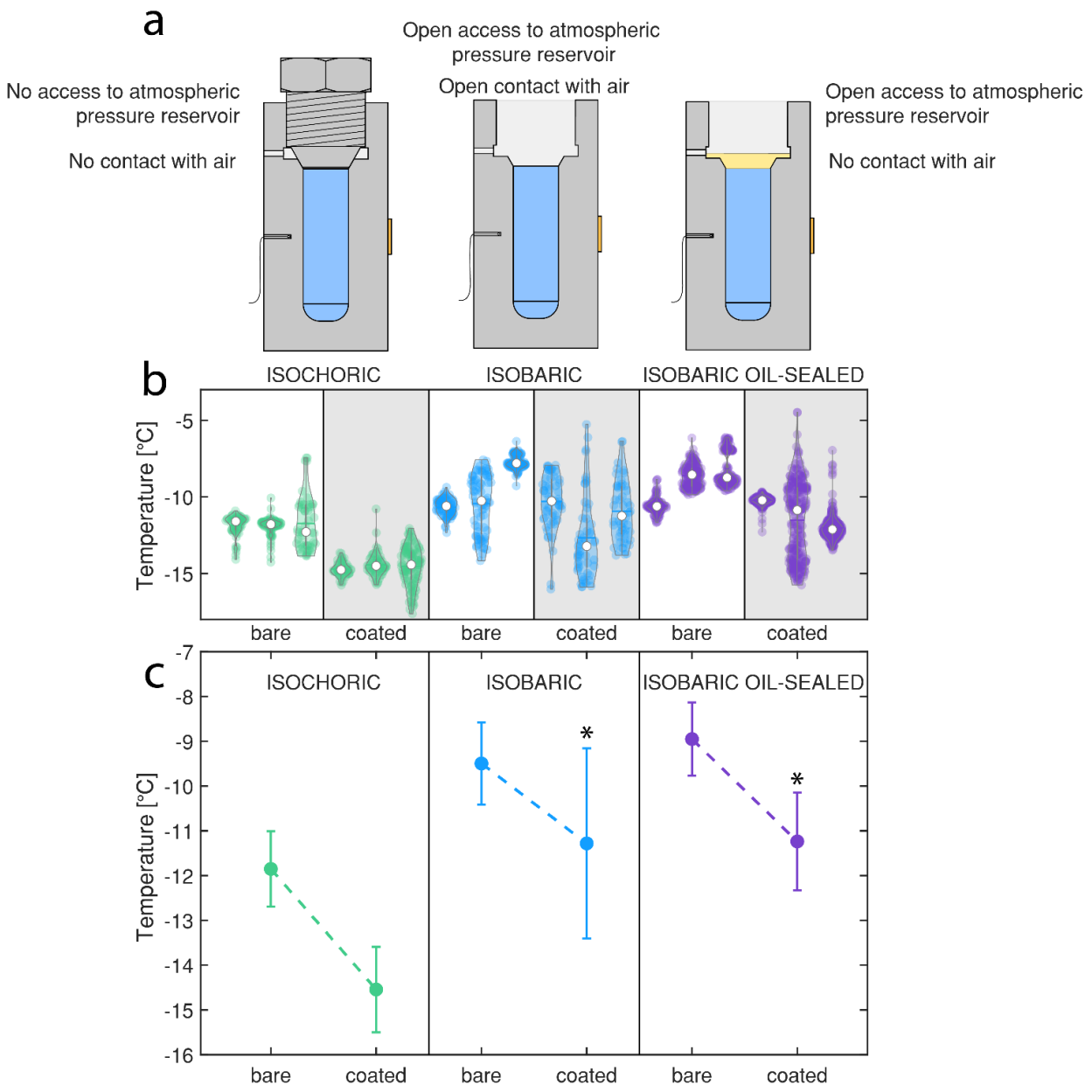

Figure 2.9: Investigation of thermodynamic conditions (isochoric, conventional isobaric, and isobaric oil-sealed) with two different wall conditions (bare metal and petrolatum-

coated). (a) Schematic illustration of experimental configurations. (b) Violin plot distributions of nucleation temperatures. Each violin plot represents an experiment performed on a different sample in a different device. (c) Mean nucleation temperature for each experimental condition. For each condition, experiments were conducted in three (3) separate chambers for a minimum of 50 cycles each. Each value reported in (b) is the average of the mean nucleation temperatures from each chamber, weighted by the number of cycles. Error bars indicate the average of the standard deviations for each chamber, weighted by the number of cycles. Asterisks (*) indicate conditions that produced statistically similar results.

Firstly, for both surface conditions, bare and coated, the isochoric systems exhibit significantly lower mean nucleation temperatures than both the isobaric and isobaric oil-sealed systems. This finding supports previous theoretical suggestions that isochoric confinement increases the nucleation barrier and decreases the probability of nucleation at a given temperature[46], and is furthermore consistent with previous experimental findings that found isochoric supercooling to be more stable than its isobaric alternatives at a given sub-zero centigrade temperature[36]. Interestingly, oil-sealing produces no statistically significant effect on the observed nucleation temperature as compared to the unsealed isobaric system, seemingly contrary to previous findings[28], [54]. Based on the fact nucleation occurs heterogeneously (i.e., on surfaces) in aqueous systems of this size, we may attribute this result to the small relative surface area of the water-air interface in our system, which accounts for only approximately 6% of the total enclosed surface area. Following this logic, in systems of smaller height-to-diameter aspect ratios (such as those employed in previous studies[28], [54]), oil-sealing may be predicted to have a more marked effect.

A further explanation for these observations may lie in the three-phase contact line (i.e., the air-water-surface and air-oil-surface interface). This interface, which is present in both isobaric and isobaric oil-sealed systems, is not present in the isochoric system due inherently to the total confinement within the aluminum chamber. Recent studies have probed nucleation kinetics at three phase contact lines and have found increased nucleation propensity at these interfaces[94]–[96].

Secondly, for all three thermodynamic configurations, the addition of a hydrophobic surface coating to the bare metallic walls is found to significantly depress the mean nucleation temperature. It should be noted that the amount by which the nucleation temperature decreased is very similar between the two isobaric conditions and greater under isochoric conditions, consistent with the aforementioned surface area arguments. These results suggest that systems designed for enhanced supercooling should incorporate hydrophobic coatings not only at the air-water interface, but on every surface in contact with the liquid. However, while the supercooling enhancement effect of one token hydrophobic surface coating (petrolatum) is demonstrated here, whether these effects are specific to petrolatum or to hydrophobic coatings as a whole cannot be concluded, and future work should probe the effects of various hydrophobic coatings.

Finally, among the three thermodynamic configurations, the conventional isobaric trials produce the largest standard deviations, while the standard deviations for the isobaric oil-sealed

and isochoric trials are of comparable and lesser magnitude. This suggests that an exposed air interface, which is open to convection, the introduction of microscopic particulates, small local variance in pressure, etc., may introduce the potential for inconsistent nucleation sites, a result that is consistent with previous supercooling experiments[28], [36], and that isochoric or oil-sealed conditions should be employed for fundamental nucleation characterization where possible.

Effects of common cryoprotective solutes on aqueous supercooling

While the supercooling behaviors of pure water are of fundamental interest to materials science, a myriad of biological, geochemical, and atmospheric supercooling processes of interest involve the incorporation of various solutes. The equilibrium freezing point depression accompanied by the addition of various solutes to water is well documented; however, the effect of these same solutes on complex kinetic processes such as heterogeneous nucleation is less well understood. Amongst the many studies that have probed the metastability of aqueous solutions[75], [93], [97]–[99], it is often hypothesized that the presence of solutes disrupts the hydrogen bonding network of water molecules and their ability to produce crystalline-like order, and that this disruption results in a decreasing homogeneous nucleation temperature relative to pure water[69].

To demonstrate the utility of the INDe for characterizing the effect of solutes on supercooling in bulk aqueous solutions, we perform transient supercooling experiments on binary solutions of four common cryoprotective compounds: dimethyl sulfoxide (DMSO), ethylene glycol, glycerol and propylene glycol. In order to probe the maximal possible supercooling, per the results in the previous section, these experiments are conducted under isochoric conditions in chambers coated with petrolatum. Figure 2.10 shows the nucleation temperature data for trials conducted at concentrations of 1 mol%, 2.5 mol% and 5 mol% of each solute. Figure 2.10a-d show the distributions of the experimental nucleation data in violin plot form, Figure 2.10e-h show survivor curves for this data, and Figure 2.10i-l show the weighted mean nucleation temperatures as a function of concentration. As in the preceding pure water experiments, a minimum of 50 trials/chamber in three different chambers are performed for each condition, providing a minimum n = 150 data points, which Figure 2.10 displays in aggregate for each solute and concentration. The chamber-by-chamber raw data for each condition (totaling 36 trials across four solutions and three concentrations) are provided in Figure 2.14.

Several significant conclusions can be drawn from the data in Figure 2.10. Firstly, the expected trend of decreasing nucleation temperature with increasing solution concentration is observed over all tested solutions and concentrations, indicating that no unanticipated surface-solute interactions or entropic effects develop with increasing solute presence. The absolute degrees of supercooling achieved by each solution are largely similar (within an approximately 2°C span for each mol%), with 5 mol% propylene glycol providing the deepest observed supercooling at –21.6°C.

Furthermore, the nucleation temperatures observed across solutions at the relatively mild concentrations probed here suggest strong untapped potential for supercooling in the context of biopreservation, in which the duration of preservation possible is a strong function of the degree of coldness achieved. Supercooled biopreservation studies have thus far been conducted at temperatures in the –3°C to –8°C range[55]–[57], [100]; however, our data suggest that much colder temperatures could potentially be achieved. For example, at 5 mol% (15.4 – 21.2 mass% or

2.4 – 2.5M depending upon the solute), all four solutions exhibit maximal supercooling at temperatures less than –20°C, and at 1 mol% (3.4 – 4.9 mass% depending upon the solute or approximately 0.5M) they exhibit maximal supercooling at temperatures less than –15.9 °C. Of course, safe and high-stability supercooling cannot be performed at the limit of supercooling and additional analyses are required to estimate the temperatures at which high stability is guaranteed (discussed in the following section), but the magnitudes of the nucleation temperatures shown in Figure 2.10 suggest that significantly colder supercooled biopreservation is possible without the incorporation of high-toxicity concentrations cryoprotectant chemicals.

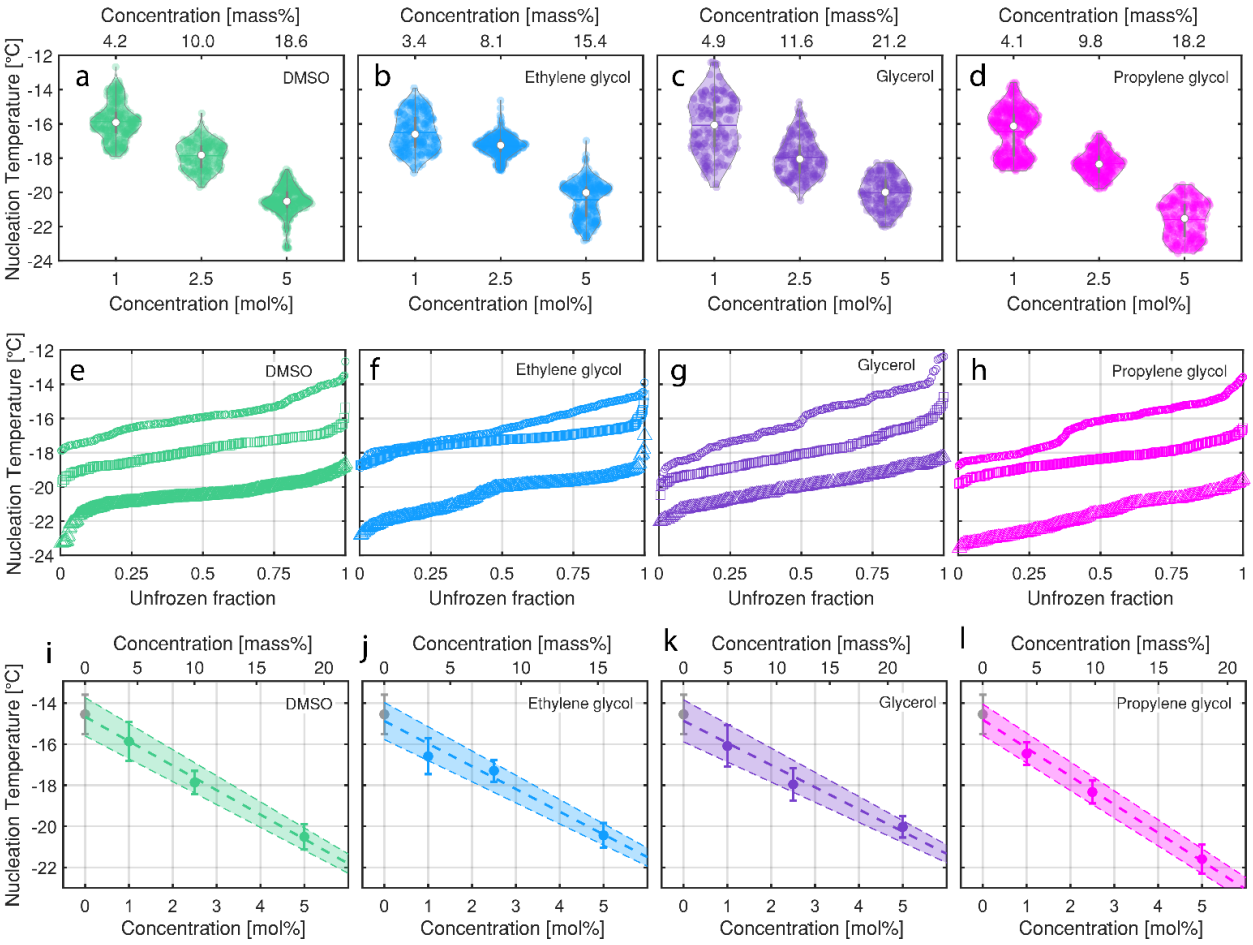

Figure 2.10: Nucleation temperature data for binary solutions of water and four solutes: DMSO (green), ethylene glycol (blue), glycerol (purple), propylene glycol (pink). (a)-(d) Violin plot distributions of nucleation temperatures. (e)-(h) Survivor curves for distributions shown in (a)-(d). (i)-(l) Weighted mean nucleation temperatures as a function of concentration. Error bars and shaded region indicate one standard deviation.

In addition to solution-by-solution analysis of absolute supercooling, useful insight can be attained through comparison of the relative supercooling (i.e., the distance in temperature past the equilibrium melting point to which the solution is supercooled) between solutions. One oft-used parameterization framework, termed the lambda method[75], [93], [101], [102], characterizes the effect of solutes on aqueous supercooling using the relation:

$$\Delta T_{nuc} = \lambda \Delta T_{melt} \tag{2.35}$$

wherein ΔT_{melt} is the equilibrium melting point depression of the aqueous solution, $\Delta T_{nuc} = T_{nuc,solution} - T_{nuc,water}$, is the depression of the nucleation temperature of the solution relative to the nucleation temperature of pure water, and λ is an empirical constant that depends on the nature of the solute as well as experimental conditions such as the presence of specific ice nucleators and sample volume[101]. Following this approach, for a set of identical experimental conditions, the relative supercooling ability of different solutions may be compared on the basis of their λ value. It has been found that for homogeneous nucleation in microscale systems (sub-mL volumes, typically probed using droplets), λ is approximately equal to 2[75]. Exceptions to this exist for large molecules, such as polymers and long-chain carbohydrates, which exhibit significantly non-ideal behavior in solution and have been shown to produce λ values up to and greater than 4[75], [98]. The λ value for homogeneous nucleation at the microscale represents the upper bound for a given solution however, and for heterogeneous nucleation, λ will decrease with increasing nucleation propensity.

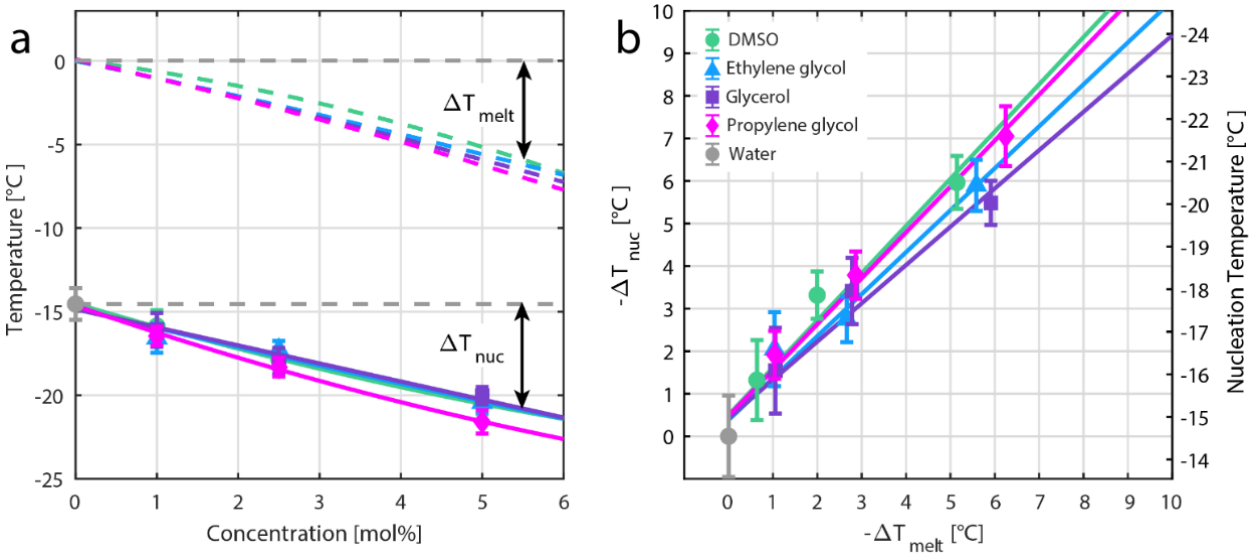

Figure 2.11: Equilibrium melting temperature and nucleation temperature curves for four solutes: DMSO (green), ethylene glycol (blue), glycerol (purple), and propylene glycol (pink). (a) Equilibrium melting temperatures and nucleation temperatures as a function of concentration. ΔT_{melt} is the equilibrium melting point depression. ΔT_{nuc} is the difference between the nucleation

temperature for the solutions and the nucleation temperature of pure water. (b) Change in nucleation temperature versus melting point depression.

Applying the lambda method, we proceed to compare the relative supercooling between solutions. Figure 2.11a provides both the equilibrium melting temperature and nucleation temperature curves as a function of concentration for the four studied solutions, and comparison via the lambda method is achieved in Figure 5b by plotting the degree of additional supercooling compared to pure water, ΔT_{nuc}, against the equilibrium melting point depression, ΔT_{melt}. Two conclusions may be drawn from this comparison.

Firstly, the ratio $\lambda = \Delta T_{nuc}/\Delta T_{melt}$ falls between 0.95 and 1.2 across all solutions tested herein. The majority of prior nucleation research evaluating solution supercooling by the lambda method has examined microscale systems, and often in the homogeneous nucleation regime. To our knowledge, this data provides the first high-statistical power lambda values for these solutions at > 1 mL volumes and under consistent surface conditions, and we thus suggest that an approximate value of $\lambda = 1$ may provide a sound benchmark for the scaling of bulk supercooled solutions with their melting point depression.

Secondly, Figure 2.11b demonstrates that while ethylene glycol, propylene glycol, and DMSO all exhibit very similar behavior, glycerol provides appreciably less supercooling per unit melting point depression. It is difficult to speculate as to the origin of this difference, however previous work in the homogeneous regime has similarly reported that glycerol provides less supercooling as compared to ethylene glycol[98].

Calculating nucleation induction times using INDe data

This work has thus far presented results on the supercooling of aqueous media with the interest of measuring the absolute and relative degrees of supercooling afforded to water by the addition of various solutes or the application of different thermodynamic conditions. We now turn to the oft-overlooked next step in supercooling analysis: adaptation of this material data to a useful application.

In order to facilitate supercooled biopreservation, stability of supercooling must be ensured for extended periods, typically on the order of days or weeks—which of course precludes the use of the maximal supercooling temperatures reported in the preceding section, at which ice nucleation is induced over a period of seconds. Thus, to design an effective biopreservation protocol, one must know not simply the maximum degree of supercooling possible, but the maximum degree of supercooling *at which* the induction time of nucleation (the period that the solution will remain stably supercooled preceding the emergence of the first nucleus) exceeds the desired preservation duration. While direct experimental probing of the requisite relationship between temperature and induction time can prove incredibly time-intensive, this relationship can be reliably estimated using only the survivor curve data that we have already generated herein.

Nucleation of a solid phase from a liquid phase is often analyzed through the lens of classical nucleation theory, a semi-physics-based phenomenological framework developed in the mid-20th century. However, nucleation may also be modelled as a Poisson process, an approach that has enabled significant recent progress in untangling the phase transformation kinetics of metals, ceramic materials, and phase-change energy storage materials[84], [103]–[105].

In particular, Lilley et al.[84] have recently developed a model by which to calculate the induction time as a function of temperature for a given system using only high-throughput bench-scale nucleation data, such as that presented in Figure 2.10, and we here adapt this approach to estimate the induction time-temperature relationships for our solutions of interest. Within this model, the Poisson rate parameter is taken to equal to the nucleation rate, $J\left[\frac{nuclei}{s}\right]$, which may be fitted to a function of the form

$$J(T) = \gamma \Delta T^n \tag{2.36}$$

$$\chi(T) = \exp\left(-\frac{1}{\beta}\int_{T_m}^{T} J(T)dT\right) = \exp\left(-\frac{\gamma(T_m - T)^{n+1}}{\beta(n+1)}\right) \tag{2.37}$$

wherein β is the cooling rate in $\frac{^\circ C}{s}$. In our INDe system, the cooling rate is prescribed, and thus Equation (2.36) can be fitted to the experimentally measured survivor curves (an example fit is shown in Figure 2.15) in order to determine γ and n and obtain the nucleation rate as a function of temperature. Finally, the average induction time τ can then be calculated as $\tau = J^{-1}$.

2.2.7 Mapping stability for supercooled biopreservation

Following the aforementioned procedure, the induction time-temperature relationship is computed for the pure water trials with petrolatum coating (Figure 2.12a) and for the four solutes presented thus far (Figure 2.12b-e). The induction times are computed for each individual trial and the shaded regions provide the range of induction times for the three individual trials of each condition. The solid lines give the average of the three individual induction times. It should be noted however that the induction times are computed from experimentally-obtained survivor functions, whose empirical functional form is non-linear. Thus, this average does not capture the full predictive power of the empirical data that the shaded range does, and may vary from the true average, the computation of which would require a method of averaging a set of multi-parameter empirical cumulative distribution functions. Future work should investigate more sophisticated mathematical approaches by which to extend averaging of raw nucleation data to computed induction times or other secondary parameters.

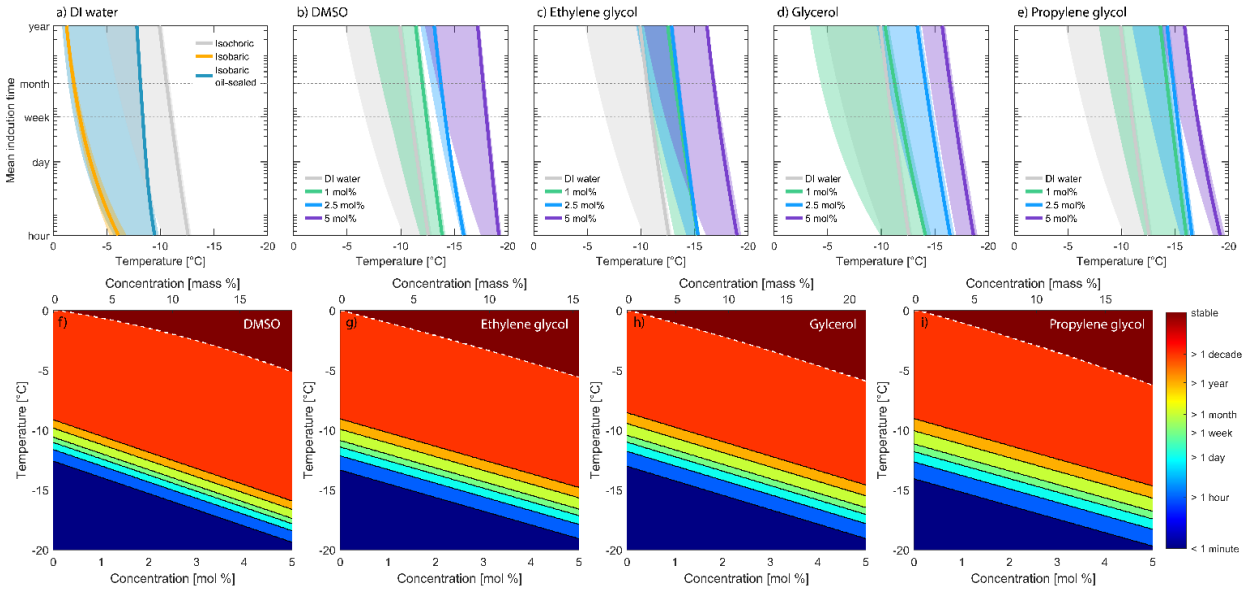

Figure 2.12: Isochoric nucleation induction times. (a) Nucleation induction times as a function of temperature for pure water under three thermodynamic boundary conditions (isochoric, isobaric, isobaric oil-sealed) and with petrolatum-coated walls. (b)-(e) Nucleation induction times for solutions of DMSO (green), ethylene glycol (blue), glycerol (purple) and propylene glycol (pink) at concentrations of 1 mol%, 2.5 mol% and 5 mol%. Shaded region represents range of induction times from the three individual trials for each condition. Solid lines represent the average of the computed induction times. (f)-(i) Induction time stability maps as a function of temperature and solution concentration. White dashed lines indicate equilibrium melting point, above which the solutions are indefinitely stable.

Figure 2.12a offers further insight into the effect of thermodynamic conditions. Isochoric conditions, which produce the lowest nucleation temperature of the three conditions probed in Figure 2.9, also produce the most stable supercooling, as can be seen by comparing the predicted induction times for the three conditions at any given temperature. Interestingly, the oil-sealing, which produced no significant effect on mean nucleation temperature when compared with conventional isobaric, shows distinctly longer inductions times on average. This result may serve to support previous oil sealing experiments conducted by Huang et al.[28], [54] which were conducted over extended durations and found improved long-term stability with surface sealing.

Figure 2.12b-e demonstrate the effects of solutes on induction time and highlight the extreme sensitivity of induction time to temperature, with shifts of only a few degrees yielding orders-of-magnitude changes in the induction time. For example, a 2.5 mol% solution of ethylene glycol, which is expected to remain supercooled for an hour at –15°C, has a predicted induction time longer than one year at –12.5°C. Similarly, at a given temperature, a slight increase in solution concentration also increases the predicted induction times by orders of magnitude.

This sensitivity highlights the difficulty of designing supercooled biopreservation protocols without rigorous advance characterization of the desired preservation solution and suggests that Figure 2.12a-e may be referenced directly by the interested cryobiologist for the informed design of supercooled biopreservation protocols. For example, this analysis predicts that preservation on the order of months in a solution of 5 mol% (15.4 mass%, ~2.5M) ethylene glycol may be conducted at temperatures as cold as –16°C, or in a solution of 1 mol% (4.2 mass%, ~0.5M) solution of DMSO at temperatures as low as –12°C.

In Figure 2.12e-h, we extend further the utility of this average induction time data by incorporating a continuous concentration axis, which we achieve by fitting a three-dimensional surface to the curves shown in Figure 2.12a-e and constructing concentration-temperature-induction time heatmaps. We term these "supercooling stability maps", and the discrete contours shown capture the estimated temperature-variance of a given induction time (1 day, 1 week, 1 month, etc.) with solution concentration, providing a new supercooled biopreservation design tool. The white dashed lines represent the equilibrium melting temperature, above which a solution is indefinitely stable. As more granular understanding of the principle biological factors affecting biopreservation (solution toxicity, temperature dependence of metabolism, etc.) emerges, it is anticipated further that this data may be used to optimize preservation temperature and preservation period / induction time against solution toxicity, which is in many cases a clear function of concentration.

Some limitations to the interpretation of this data should be noted: All supercooling tests herein probed a 5 mL volume of aqueous media, and the induction times presented in Figure 2.12 describe this particular system. If the assumption is made that nucleation is initiated on the interior chamber surface, the computed nucleation rates and induction times may be linearly scaled by the surface area for any isochoric system with petrolatum-coated surfaces. However, future studies must experimentally validate this scaling and investigate the possibility of a volumetric contribution.

Furthermore, as noted previously, determination of the true average induction times across samples/systems, the nucleation behaviors of which all produce Poisson distributions but not the *same* Poisson distribution, proves mathematically non-trivial, and must be investigated further. What's more, the end application of supercooled biopreservation provokes many questions about the interpretation of the temperature-induction time relationship in protocol design— *should* an average induction time be used to design a biopreservation protocol? Can factors of safety be incorporated in supercooling protocol design by operating some distance from these averages, or outside the range of observed values? How can we further quantify the relative stability or instability of supercooling for a given time period as we increase or decrease temperature? These and other questions arising from the development of the proof-of-concept stability maps shown herein point to the need for significant future statistical analyses by which certainty and safety in stable supercooling can be more specifically guaranteed.

2.2.8 Conclusions

In this work, a new device for high-throughput characterization of aqueous supercooling in bulk-volumes is presented, termed the isochoric nucleation detector (INDe). This device uses a

new non-invasive pressure-based nucleation detection mechanism enabled by the unique thermodynamics of aqueous isochoric systems and provides a platform for probing many of the myriad factors that affect bulk-volume aqueous supercooling with high statistical power. Over the course of three studies, totaling thousands of nucleation detections, we identify three key factors that affect the stability and depth of supercooling in bulk aqueous systems. Firstly, isochoric thermodynamic conditions enable significantly deeper supercooling than conventional isobaric or isobaric oil-sealed conditions; secondly, applying a hydrophobic coating (here petrolatum) to all solid surfaces in contact with the liquid enhances supercooling regardless of thermodynamic condition; and thirdly, common cryoprotective solutes enhance the maximal supercooling temperature possible at a rate roughly equal to their freezing point depression. In order to increase the direct utility of these findings to the biopreservation community and others seeking to harness stable aqueous supercooling, we also input our maximal supercooling data into a Poisson statistics model that enables prediction of the relationship between supercooling temperature and nucleation induction time, or how long a supercooled system will remain stable at a given temperature. Finally, we use this information to introduce and construct proof-of-concept supercooling stability maps, a new reference tool to enable informed design of stable supercooled biopreservation protocols. This work in sum presents a new experimental and theoretical pipeline by which to first characterize and ultimately utilize aqueous supercooling at $>$ 1 mL volumes.

2.2.9 Supplemental Information

Materials and Methods

Experimental materials. Deionized water (type II, SKU S25293) and ethylene glycol (SKU E178) were purchased from Thermo Fisher Scientific (USA). Mineral oil for the oil-sealing experiments (SKU M8410), propylene glycol (1,2-propanediol, SKU 398039), DMSO (dimethyl sulfoxide, SKU D5879) and glycerol (SKU G7893) were purchased from Sigma-Aldrich (USA). Petrolatum used to coat the interior chamber surface was purchased from Vaseline, Unilever (UK).

Isochoric nucleation detector electronics. The isochoric nucleation detection (INDe) system is comprised of temperature control assemblies and temperature and strain monitoring systems, which are controlled via a Python-based control software running on a Raspberry Pi 4B single board computer (Raspberry Pi Foundation, UK). The temperature control assemblies are each comprised of a two-stage thermoelectric module (CUI Devices CP60H-2 Series) and fan-cooled CPU heat sink (Cooler Master). The thermoelectric modules are controlled by a PID temperature controller (Opt Lasers, TEC-8A-24V-PID-HC-RS232). Full bridge aluminum strain gauges (3147_0), PhidgetBridge strain gauge DAQ (1046_0B), Thermocouple Phidget DAQ (TMP1101_0), and USB VINT Hub (HUB0000_0) were purchased from Phidgets Inc. (CA).

Isochoric chamber loading procedure. Solutions are first prepared using an analytical balance (A&D ER-182A). The solution (or deionized water) is then dispensed slowly into the chamber using a syringe so to not introduce any air bubbles or air pockets. The plug is then threaded into the chamber until the sealing surfaces contact each other, after which a digital torque wrench (Yellow Jacket 60648) is used to apply a torque of 45 ft-lbs. This torque is applied to ensure a tight metal-on-metal seal is formed. No pressure is applied to the liquid during this process, as excess

liquid is forced out through the weep hole. This was confirmed in preliminary trials using a pressure transducer, as shown in Figure 2.8c.

Chamber surface coating. For the coated deionized water experiments and all aqueous solution experiments, the interior chamber surface is coated with a thin layer of petrolatum. To apply this coating, the chamber is first heated using a standard heat gun, and a small amount of petrolatum (<1mL) is then placed into the chamber. After melting the petrolatum, the chamber is then inverted and simultaneously rotated in order to coat the entire surface while allowing excess liquid to drain out. The chamber is then left to cool in a refrigerator at ~2°C to allow the petrolatum coating to solidify. A thin layer of petrolatum is also applied to the bottom surface of the plug.

Statistical analysis. For all supercooling results presented, a minimum of 50 consecutive nucleation cycles were performed for each trial and repeated in three separate chambers, totaling a minimum of n=150 data points per experimental condition. These data are then aggregated for each condition and reported as a weighted average across trials, accompanied by a weighted average of the standard deviations of each trial. Statistical difference was confirmed using one-way ANOVA and Bonferroni's multiple comparisons test. Significant difference was indicated by a value of $p < 0.05$, and groups that were determined not to be significantly different (i.e., share a common mean) were marked with asterisks. Due to the large number of data points obtained for each condition, the standard error of the mean was miniscule in all cases and was thus not reported.

Isochoric nucleation detection (INDe) array

The isochoric nucleation detection (INDe) device is a scalable platform suited for performing high-throughput supercooling experiments on aqueous systems. The INDe system introduced in this study utilizes solid-state thermoelectric modules for both cooling and heating. Together with air-cooled heat sinks, this design enables implementation in any laboratory setting without the need for refrigerated fluid circulating systems. Pictured in Figure 2.13 is an array of six (6) individual INDe devices operating off a single Raspberry Pi computer (bottom right). The temperature of each INDe is controlled by a separate PID temperature controller (bottom left), which receives commands from the centralized control dashboard.

Figure 2.13: Array of isochoric nucleation detection devices.

CPA solution raw data violin plots

Shown in Figure 2.14 are the violin plot distributions of the nucleation temperatures for the 36 individual solution experiments. Experiments were conducted in three independent chambers for each of the four solutes (DMSO, ethylene glycol, glycerol and propylene glycol) at three concentrations (1 mol%, 2.5 mol% and 5 mol%).

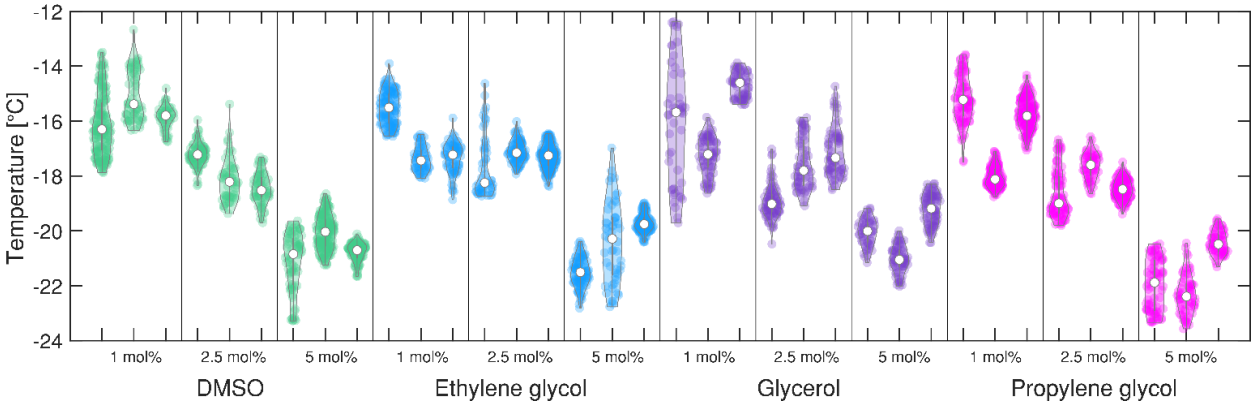

Figure 2.14: Nucleation temperature violin plot distributions for CPA experiments.

Statistical model for calculation of isothermal induction time

As described by Lilley et al.[84], transient supercooling experiments of the type performed in this study, wherein the temperature of a sample is lowered at constant rate until nucleation occurs, may be modelled as a non-homogeneous Poisson process. For surface-initiated nucleation, the survivor function, $\chi(T)$, is related to the nucleation rate, $J(T)$, by Equation (2.36) of the main text as

$$\chi(T) = \exp\left(-\frac{1}{\beta}\frac{\gamma(T_m - T)^{1+n}}{1+n}\right) \tag{2.38}$$

wherein β is the cooling rate, T_m is the equilibrium melting point, and γ and n are empirical fitting parameters. This equation may be fitted to the survivor curves generated by the INDe in order to obtain values for γ and n. Figure 2.15 shows the experimental (markers) and fitted (solid lines) survivor curves for each of the trials. Table 2.1 provides the values for the fitting parameters, γ and n.

Table 2.1: Empirical nucleation rate parameters obtained by fitting experimental survivor function data to Poisson distribution.

	n	γ
Isochoric DI water Bare	30.25	1.67E-34
	54.52	1.69E-60
	7.8	6.68E-11
Isochoric DI water Petrolatum	38.64	3.37E-47
	27.95	1.32E-34
	11.87	2.68E-16
Isobaric DI water Bare	21.86	1.35E-24
	5.56	2.10E-08
	20.79	2.10E-20
Isobaric DI water Petrolatum	5.88	1.69E-08
	5.67	5.29E-09
	5.67	1.69E-08
Isobaric oil-sealed DI water Bare	26.4	4.12E-29
	12.88	2.64E-14
	8.34	6.68E-10
Isobaric oil-sealed DI water Petrolatum	59.33	1.03E-61
	4.7	8.33E-08
	24.11	3.29E-28

	n	γ
DMSO 1 mol%	15.13	2.10E-20
	17.74	6.68E-23
	44.20	2.64E-54
DMSO 2.5 mol%	49.17	4.21E-60
	27.69	1.06E-35
	33.46	8.42E-43
DMSO 5 mol%	16.52	2.68E-22
	26.24	5.29E-33
	60.40	8.42E-74
Ethylene glycol 1 mol%	26.62	4.21E-33
	42.76	6.68E-54
	37.25	2.64E-47
Ethylene glycol 2.5 mol%	17.42	8.33E-23
	43.99	5.29E-53
	37.20	2.13E-45
Ethylene glycol 5 mol%	34.85	5.29E-44
	11.28	8.42E-16
	52.65	2.10E-62

	n	γ
Glycerol 1 mol%	6.68	1.34E-10
	26.56	2.13E-34
	32.71	3.37E-39
Glycerol 2.5 mol%	35.92	1.69E-45
	17.53	8.33E-23
	19.29	1.34E-24
Glycerol 5 mol%	32.12	4.21E-39
	34.85	3.33E-43
	26.72	3.37E-32
Propylene glycol 1 mol%	18.76	6.68E-24
	51.63	1.67E-65
	28.65	1.34E-35
Propylene glycol 2.5 mol%	20.63	5.29E-27
	37.57	5.29E-46
	49.23	1.05E-60
Propylene glycol 5 mol%	17.80	1.06E-23
	25.92	1.67E-33
	39.23	3.33E-47

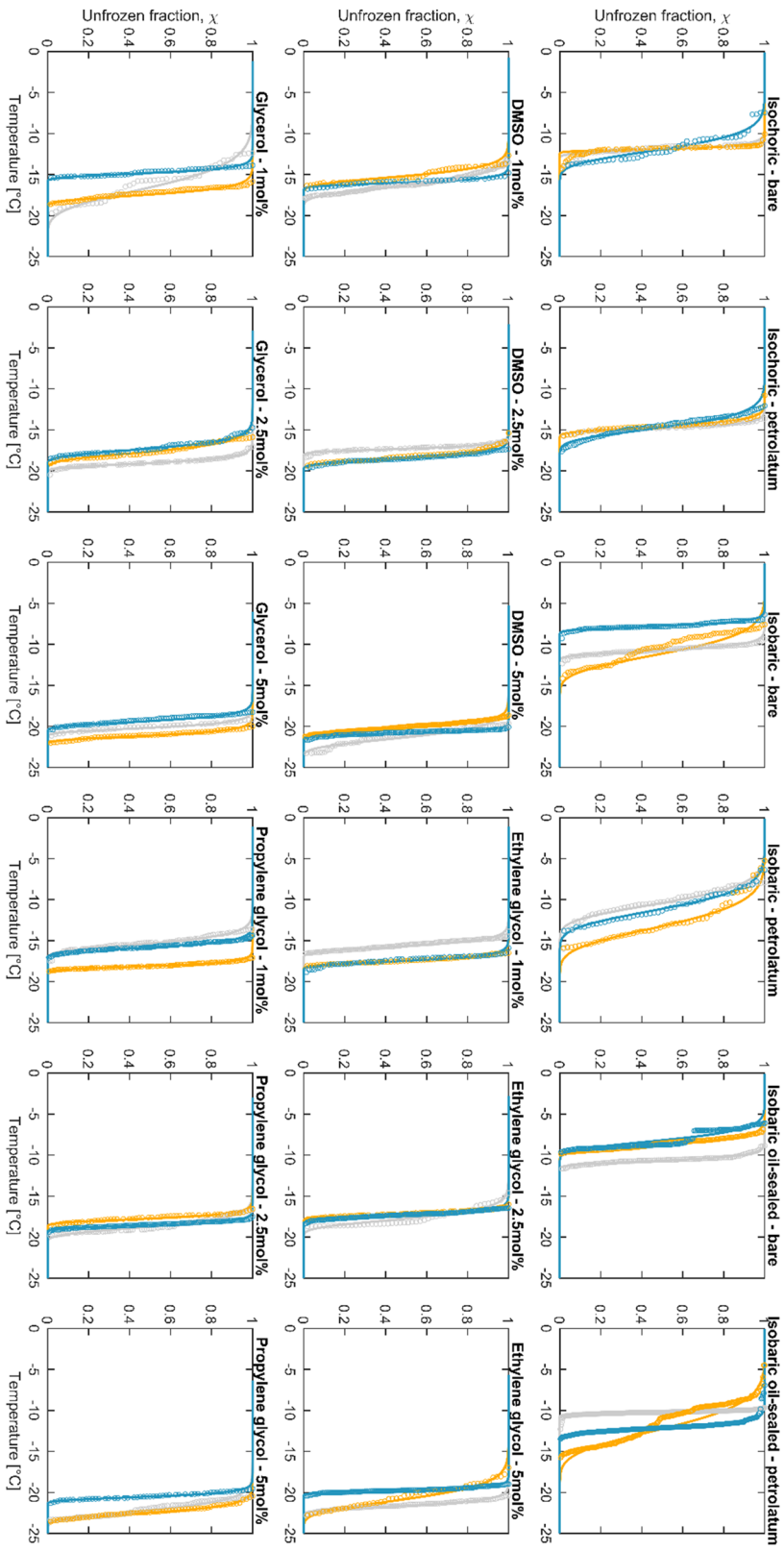

Figure 2.15: Experimental (markers) and fitted (solid lines) survivor curves.

INDe Chamber Thermal Analysis

A 3D transient thermal analysis of the INDe chamber was performed in COMSOL Multiphysics (results depicted in Figure 2.16). A cooling rate of 2°C/min was applied to the two opposing sections of the chamber surface in contact with the thermoelectric modules. Over the course of cooling from 0°C to –25°C, the interior wall of the chamber is found be uniform to within ±0.05°C. The temperature at the center of the water volume is also found to lag the wall temperature by at most 2.5°C.

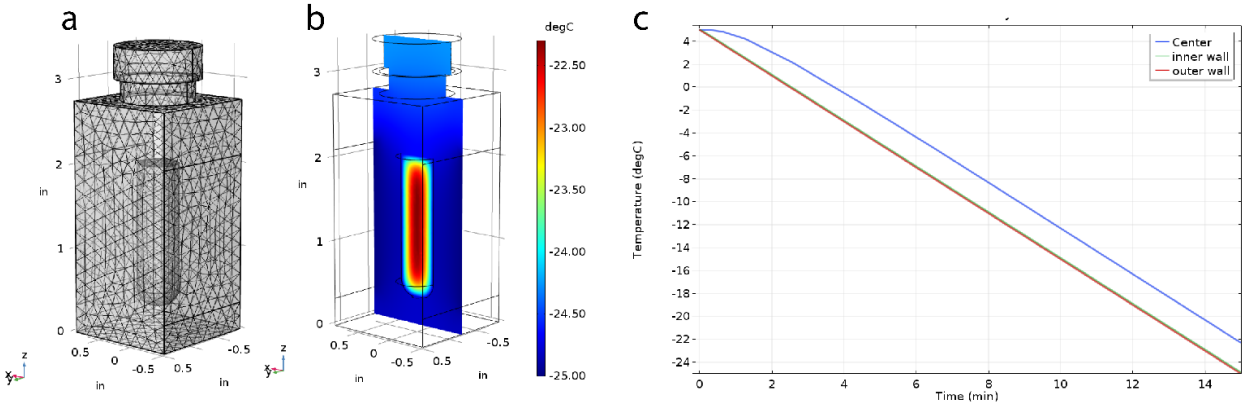

Figure 2.16: Thermal analysis in COMSOL Multiphysics. a) 3D geometry and mesh of chamber. b) Temperature profile of center plane at t=15 min. c) Temperature evolution of liquid center, inner wall and outer wall.

2.3 Enhanced control over ice nucleation stochasticity using carbohydrate polymer cryoprotectants

2.3.1 Overview

Metastable supercooling has emerged as a trans- formative technique for ice-free biopreservation, but issues of stability inherent to the stochastic nature of ice formation have thus far limited its translation out of the laboratory. In this work, we explore the influence of the bio-based carbohydrate polymer FucoPol on aqueous supercooling using an isochoric nucleation detection technique. We show that FucoPol, a high-molecular-weight, fucose-rich polysaccharide, which has previously been shown to reduce average ice crystal sizes after nucleation, also induces a concentration-dependent stabilization of metastable supercooled water, as evidenced by both a significant reduction in nucleation stochasticity (i.e., the spread in temperatures over which the system will nucleate upon cooling) and a corresponding increase in the predicted induction time of nucleation.FucoPol is found to confine the stochasticity of ice nucleation to a narrow, well-defined band of temperatures roughly one-third as wide as that of pure water under identical conditions. Importantly, this substantial reduction in stochasticity is accompanied by only a minimal (<1 °C) change in the average nucleation temperature, suggesting that this effect is distinct from colligative freezing point depression. Reducing and characterizing the stochasticity of aqueous supercooling is essential to the engineering design of practical biopreservation protocols, and the results reported herein suggest that high-viscosity polymer systems may provide a powerful and largely unexplored lever by which to manipulate metastable-equilibrium phase change kinetics at subzero temperatures.

2.3.2 Motivation of this study

Aqueous supercooling has shown recent promise for a range of applications, particularly in the atmospheric [51], food [106] and biomedical fields [28], [107], wherein an aqueous system is held in an ice-free state below the freezing temperature of water. Because supercooling is thermodynamically metastable however, stabilizing the supercooled state through chemical, mechanical, or other means is of great importance for the usability of supercooled systems in all manner of applications, and perhaps most namely biopreservation [17], [18], [108].

Current methods for securing the viability of biological matter during sub-zero temperature preservation rely principally on the use of chemical cryoprotectants (CPAs) capable of reducing ice crystal size, growth potential or occurrence altogether. However, Rubinsky *et al.* have shown the efficacy of isochoric (constant-volume) chambers at forcing pressurized, biphasic water-ice systems to undergo continuous and controlled phase transition along the *liquidus* line, in which the frozen fraction can be manipulated via the final temperature/pressure or chemical modulation and ice-free preservation of biologics in the liquid volume achieved, something unattainable using conventional isobaric freezing [47].

This methodology eliminates the usage of toxic concentrations of CPAs to achieve an ice-free environment in the biological volume by leveraging the pressure that emerges with the expansion of ice under confinement, but it is limited in temperature by the deleterious effects of pressure

[109]. Acknowledging the limitations of high pressure, recent studies have explored the effects of isochoric conditions on aqueous supercooling, in which the aqueous system confined in the isochoric chamber is held in a pre-nucleation, ice- and pressure-free liquid state. These studies have identified several possible mechanisms by which the stability of supercooling should be enhanced in isochoric systems [19], [110], and shown experimentally that indeed isochoric confinement has the effect of decreasing the likelihood of ice nucleation [111], [112].

Even considering these effects however, applications of isochoric supercooling are still subject to uncertainties borne of the stochastic nature of ice nucleation. This stochasticity means that the probability of nucleation can be predicted over a range of temperatures, but the random probability distribution means nucleation cannot be pinpointed to a single temperature. The practical consequence is that, under isochoric conditions, the extent and location of ice formation can be finetuned, but its physical traits of emergence cannot: even by precisely manipulating thermodynamic phenomenology, this statistical randomness may still result in *rogue* nucleation, at a temperature that the system may cascade into unintended freezing and pressurization, thus permanently damaging valuable biological matter.

Therefore, there is a need to find methods and molecules capable of reducing nucleation stochasticity. Previous work by Suzuki *et al.* [113] has shown that viscosity, molecular weight and rotational correlation time have an influence on the supercooling temperature of water. Thus, supercooling is correlated with intrinsic properties that define molecular structure. Although small molecules have been extensively studied, relatively few polymeric systems have been probed for their potential [114], and none under isochoric conditions.

FucoPol is a high-molecular-weight ($1.7-5.8\times10^6$ Da) fucose-containing polysaccharide secreted by the Gram-negative bacterium *Enterobacter* A47 (DSM 23139) [115], [116], whose cryoprotective [117], [118] properties were recently demonstrated. FucoPol has a fucose, galactose, glucose, and glucuronic acid hexamer motif (2.0:1.9:0.9:0.5 M ratio), a main chain composed of a →4)-α-L-Fuc*p*-(1→4)-α-L-Fuc*p*-(1→3)-β-D-Glc*p*(1→ trimer repeating unit, and a trimer branch α-D-4,6-pyruvyl-Gal*p*-(1→4)-β-D-GlcA*p*-(1→3)-α-D-Gal*p*(1→ in the C-3 of the first fucose [117]. FucoPol also contains 13−14 wt.% pyruvyl, 3−5 wt.% acetyl, and 2−3 wt.% succinyl in its acyl composition [119]. The presence of glucuronic acid as well as the acyl substituents pyruvyl e succinyl all confer a polyanionic character to the polymer [120]. Its aqueous solutions have a shear-thinning behavior.

Previous work has shown the wide potential of FucoPol applications. First, it acts as a crystallization inhibitor, successfully cryopreserving several animal cell lines by promoting earlier ice nucleation at sub-zero temperatures but reducing ice crystal dimensions to innocuous sizes [117]. Second, it has a rheological shear-thinning behavior reflective of a linearly-disposed helical conformation, showing strong analogy to antifreeze proteins [121], viscoelastic properties comparable to those of guar gum and fucogel [120] and emulsifying properties [116] that are desirable in the food industry. Lastly, it distinguishes itself from common-use CPAs by its bio-based non-cytotoxic nature, very low osmolality and osmotic regulation effects due to its extracellular location and suspected cell membrane stabilization effects [122]. All these properties reflect the acute interest in studying the influence of carbohydrate polymer systems in the supercooling behavior of water, and under isochoric thermodynamics in general.

In this work, we explore the influence of a bio-based carbohydrate polymer on aqueous supercooling under isochoric conditions. We show that a fucose-rich polysaccharide, with proven crystal size reduction [117] and *in vitro* cryoprotective properties [118], can confine the randomness of ice nucleation to a narrow, well-defined, near-deterministic range of nucleation temperatures. This stochasticity is one of the most defining physical constraints in manipulating success/failure rates in supercooled biopreservation. To the best of our knowledge, this is the first attempt at fundamentally characterizing high-molecular weight polymer systems under isochoric conditions and at sub-zero temperatures.

2.3.3 Raw data and reduction of stochasticity with the addition of FucoPol

Isochoric nucleation detection was performed according to the methods and protocol of Consiglio *et al.* [112] under a process of transient supercooling, in order to assess the influence of varying FucoPol concentrations on the nucleation temperature (T_n) and behavior of pure water (experimental details in Methods section). Figure 2.17 shows the T_n distributions for increasing FucoPol presence (with Fig. 1a showing all raw data recorded and Fig. 1b showing data aggregated by FucoPol concentration) and Table 2.2 summarizes all temperature data recorded.

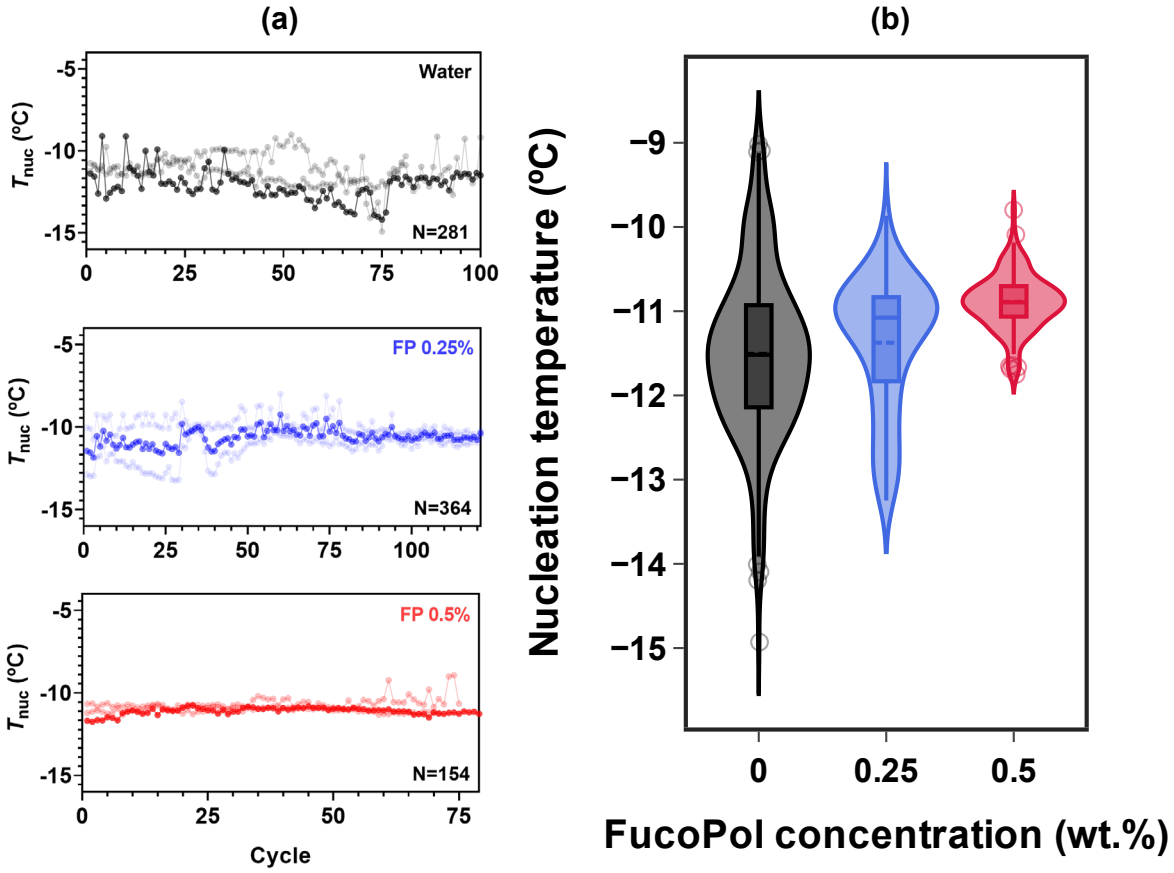

Figure 2.17: Nucleation cycle stochasticity and aggregated temperature distribution. (a) Individual nucleation cycle runs for water (black), 0.25% (blue) and 0.5% FucoPol (red). n = 3 independent trials are shown for each condition, each with >50 cycles. An increased experimental deviation of temperature points from the mean is evident in pure water. The spread of temperature data for water is minimized with increasing polymer concentration. **(b)** Corresponding violin plot distributions show a slight increase in nucleation temperature with increased FucoPol concentration. Violin plots show aggregated data from n = 3 independent trials of at least 50 cycles each for each condition. Total sample size is N=281, 364 and 154 for water, 0.25% and 0.5% FucoPol, respectively.

Table 2.2: Summary of nucleation temperature data for the INDe experiment.

Sample	Mean T_n	Median T_n	ΔT_{min}^{max}	σ	N
Water	–11.51	–11.52	5.91	1.01	281
0.25% FucoPol	–11.37	–11.08	3.38	0.79	364
0.5% FucoPol	–10.89	–10.89	1.95	0.33	154

While pure water nuclei form at an average –11.51±1.01ºC in the 5.3 ml isochoric chamber employed (identical to that described previously [112]), supplementation of FucoPol causes a distinguishable if modest increase in the T_n of water that is correlated to concentration. In the presence of 0.25% FucoPol, water nucleates at –11.37±0.79ºC and subsequently increases to –10.89±0.33ºC at 0.5% FucoPol.

As compared to pure water (Figure 2.17, black), FucoPol systems are observed to follow an increasingly-deterministic pattern of nucleation (Figure 2.17, blue and red), which is to say that the stochastic range, *i.e.* the spread of nucleation temperatures, is considerably reduced in the presence of FucoPol. Whilst the pure water distribution has a standard deviation of 1.01, the spread is decreased 1.3- and 3-fold for 0.25% and 0.5% FucoPol, respectively. Considering that the system temperature monitoring has a lower detection limit of ±0.2ºC, ice nucleation in a 0.5% FucoPol takes on a near-deterministic quality ($\sigma^2 = \pm 0.33$) at -10.89 °C.

This statistical confinement of T_n can also be interpreted as an enhanced control over ice nucleation stochasticity, and the range of temperature data in Table 2.2 more evidently shows this change. For pure water, the difference ΔT between the maximum and minimum recorded T_n is 5.91ºC, whilst for 0.25% it is 3.38ºC and only 1.95ºC for 0.5% FucoPol. In practical terms, a 0.5% FucoPol solution can contain the highly random process of ice nucleation to just under a 2ºC interval, compared to the 6ºC uncertainty of pure water. This stochastic range can be further interpreted as a measure of experimental safety. The smaller the range, the greater the control over ice nucleation will be, enabling predictive planning over which working temperature to employ in an experimental setting to avoid *rogue* nucleation events that could jeopardize the viability of preserved biological material.

2.3.4 Correlating viscosity with observed nucleation characteristics

The average nucleation temperatures recorded for each concentration were also correlated to polymer viscosity measurements. According to Suzuki *et al.* [114], the effect of molecular structure on nucleation behavior is affected by intrinsic polymer properties, such as viscosity. Figure 2.18 shows the correlation between the trending nucleation temperature as a function of concentration and a Gompertz exponential growth model for viscosity. The high correlation between a concentration-dependent increase in T_n and the log-zero shear viscosity of FucoPol validates the previous results and suggests an influence of polymeric molecular structure on ice boundary physics.

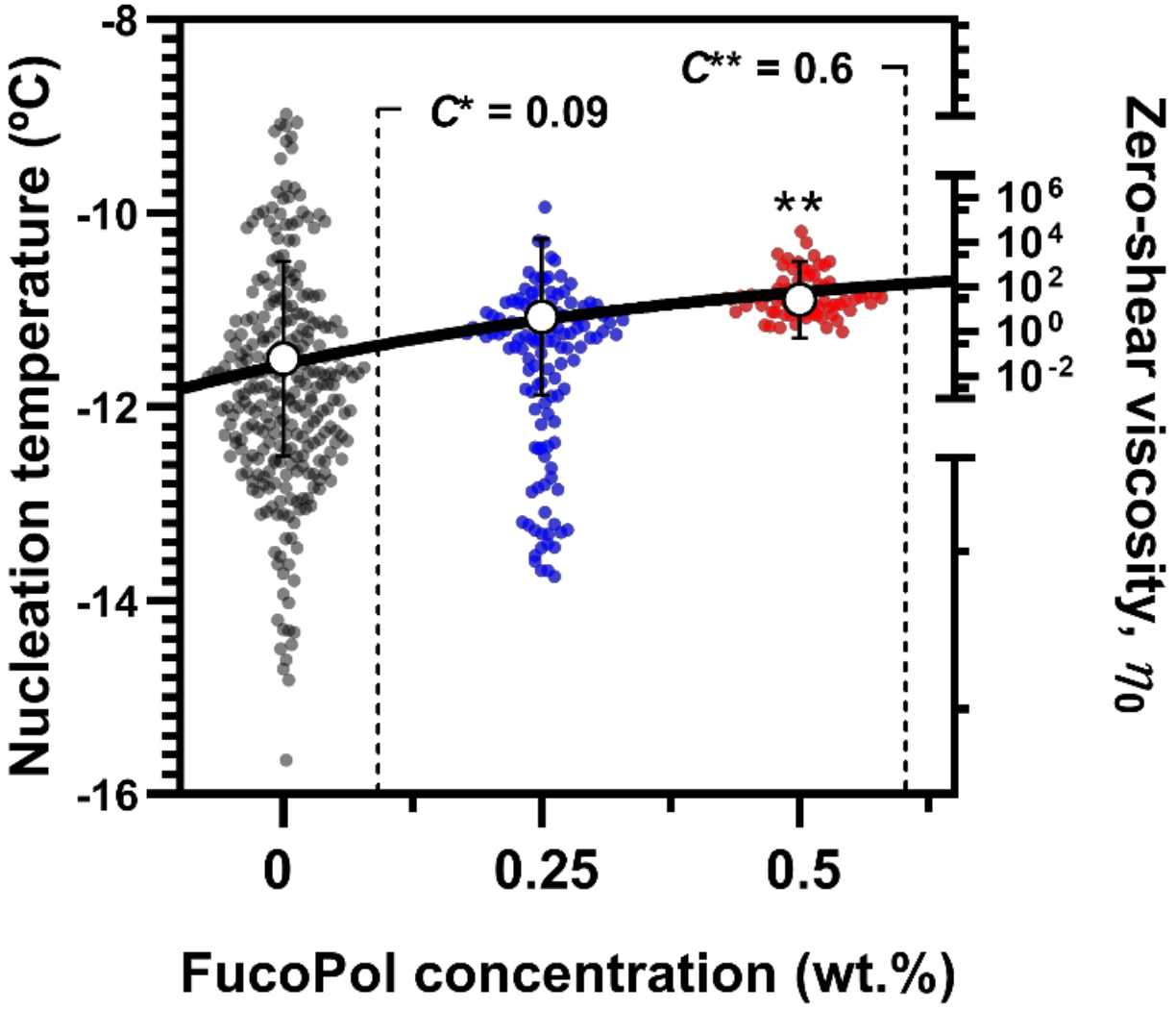

Figure 2.18: Correlation between polymer zero-shear viscosity, resulting average nucleation temperature, and stochastic range. An increase in concentration results in a statistically significant (p = 0.001) non-linear increase in water nucleation temperature, which is correlated to the log-viscosity. Zero-shear viscosity data adapted from Torres *et al.* [119] are fit to a Gompertz exponential growth model (black curve). Swarmplots of collected data points are shown along with error bars showing the standard deviation and the average nucleation temperature (white circle). Data points shown are aggregated from three experiments for each condition.

Swarmplots of nucleation temperatures were also superimposed on the viscosity curve. Note that the relative stochasticity reduction associated with the addition of polymer is always significantly larger than the relative change in average nucleation temperature, and that the slight change in nucleation temperature is *positive*. This suggests that the dominating factor affecting stochasticity is independent of thermodynamic freezing point depression, and is likely thus purely

kinetic in nature. Future studies should address the precise mechanisms mechanisms at play, which may reveal ways in which future polymers could be engineered to specifically elicit this stochasticity reduction effect.

2.3.5 Effect of reduced stochasticity on induction times and biopreservation protocol design

Ice nucleation is a stochastic process that can be statistically modelled by a Poisson distribution [13, 24], which relates the frequency of nucleation events to the temperature and duration of supercooling (see Equation (2.40) in Methods). The experimentally measured survivor curves in Figure 2.19a (unfrozen fraction vs. temperature) correspond to the cumulative distribution function of a nonhomogeneous Poisson process (Equation (2.41), Methods). By assuming a form for an empirical nucleation rate, the survivor function may be fit to an empricial cumulative distribution function describing the constant cooling rate nucleation process (Equation (2.41), Methods). The computed nucleation rate parameters for water and FucoPol systems are summarized in Table 2.3.

With knowledge of the nucleation rate, the mean induction time can be computed (Equation (2.42), Methods). This can physically be understood as the induction time necessary for the first ice nuclei to form and kickstart freezing of the whole system, or the time period for which the system will remain stable in the supercooled liquid state. Figure 2.19b shows the induction time for the three tested conditions. The shaded region represents the spread of times for the three repeated trials.

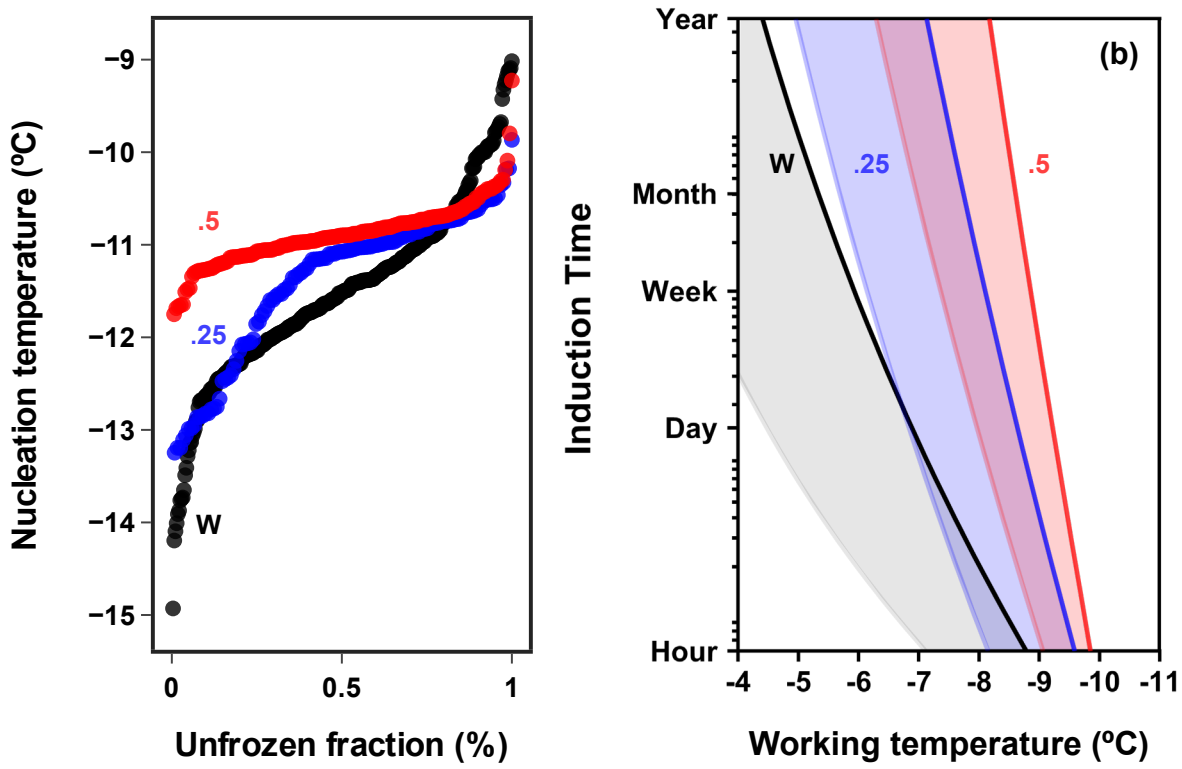

Figure 2.19: Survivor plot of the unfrozen fraction of water (a) and corresponding Poisson-modelled induction time bands on a practical timescale (b). In (a), reduction of stochasticity is evident from a reduced spread of temperature data, characterized by a visible horizontal flattening of the curve. Data points from triplicate independent runs for water (N=281), 0.25% FucoPol (N=364) and 0.5% FucoPol (N=154) are shown aggregated. In (b), actionable insight from a realistic timescale perspective can be derived from each nucleation induction time band, calculated from applying Equation (2.42) to separate runs, leaving the working system temperature and solution to choice, depending on the desired applicability.

Table 2.3: Optimal Poisson-fit parameters for a supercooled system in the presence of FucoPol.

Sample	$\Gamma\left(\frac{1}{K^n \cdot s}\right)$	n	R^2	τ (-5°C)	τ (-8°C)
Water	1.36×10^{-16}	13.0	0.942	~6 months	~1 hour
	1.04×10^{-13}	8.0			
	7.20×10^{-10}	6.6			
0.25% FucoPol	3.80×10^{-34}	30.4	0.881	>1 year	~2 weeks
	2.47×10^{-29}	26.8			
	8.60×10^{-21}	18.1			
0.5% FucoPol	4.33×10^{-52}	48.1	0.918	>1 year	>1 year
	8.22×10^{-38}	34.3			
	6.83×10^{-28}	24.7			

This analysis reveals that pure water is expected remain stable for about 4 years at –4ºC until nucleation initiates, but for only 3 hours at –8ºC. In the presence of FucoPol, water at –8ºC can remain supercooled 12 to 365-times longer, lasting a day with 0.25% or a whole month with 0.5% without any nucleation. At –4ºC, water in the presence of FucoPol is expected to remain indefinitely stable within realistic timescales.

The reduced stochasticity of ice nucleation when FucoPol is present can be interpreted further. In Figure 2.19a, the inflections of the survivor curves flatten out to narrower temperature ranges with increasing polymer concentration, which implies that statistical determinism increases and randomness decreases. The overall aspect of the curve is preserved, indicating that the solution still behaves according to the same Poisson distribution as expected.

Figure 2.19b shows that the calculated induction time (IT) bands for FucoPol concentrations reveal a concentration-dependent increase in the stabilization of the supercooled state of water. With the gradual addition of polymer, the bands steepen, conferring lengthier induction times at a given temperature. Consiglio et al. [112] has shown that DMSO, ethylene glycol, glycerol and propylene glycol also increase supercooled state stability, but do so principally by shifting the curves rather than steepening the curves. At the limit of infinite steepness (i.e., a vertical induction time curve), the system would become fully deterministic. Thus FucoPol can be interpreted to increase the determinism of the system (and reduce the stochasticity) while only mildly affecting the mean nucleation temperature.

Induction time plots like Figurb offer actionable insight to the cryobiologist by acting as a tool to assess the potential stability of a biopreservation scenario under defined conditions of temperature, solute concentration and duration of preservation. For instance, if a working temperature of –7ºC is chosen, Figure 2.19b would indicate that an aqueous isochoric solution would last a day without ice. However, by addition of 0.5% FucoPol, the preservation could be extended to roughly half a year, by conservative estimates.

2.3.6 Discussion

Recent isochoric supercooling studies by Consiglio *et al.* [112] have shown that aqueous solutions of glycerol, ethylene glycol, DMSO and propylene glycol have resulted in average nucleation temperatures of –20, –20, –21 and –22, respectively, at 5 mol% (equivalent to 15.4–21.2 wt.%). Most small molecule cryoprotectants and antifreeze proteins display depression of both the equilibrium freezing point and the nucleation temperature [124]. However, FucoPol has consistently shown a distinct effect, in which the nucleation temperature of water *increases* (albeit mildly) with addition of polymer. FucoPol was selected as the model molecule for this study due to (i) its previously demonstrated cryoprotective properties [117], (ii) a very low osmolality-to-function ratio that reduces mass transport and is capable of competing with antifreeze proteins [125], (iii) a high viscosity associated with high molecular weight [119], and (iv) an intrinsic biocompatibility that eliminates cytotoxicity issues [118]. Previous work under isobaric conditions [117] has shown that FucoPol induces the occurrence of crystallization at a higher temperature, consistent with the results herein, and that there is a concomitant 54% reduction of mean crystal size and a distinguishable effect on crystal morphology. Under isochoric conditions, concentrations of 0.25 and 0.5 wt.% FucoPol resulted in a slight increase of the mean nucleation temperature to –11.37±0.79ºC and –10.89±0.33ºC. FucoPol is thus confirmed to affect both the process of initial nucleation and subsequent crystal growth.

The most defining aspect of FucoPol's influence in isochoric water nucleation however, is the statistical confinement of nucleation temperatures. Here, we have achieved a supercooled state of water that is 1.7 to 3-times more stable in the presence of FucoPol, and with drastically increased nucleation induction times that range from a day to a month at –8ºC, compared to only 3 hours for pure water (an 8 to 243-fold increase in temporal stability). This finding has several practical consequences, providing both a *safety net* to biopreservation strategies that rely on the isothermal hold of biological matter in a supercooled state and enabling higher statistical confidence during protocol design.

Both this work and that of Consiglio *et al.* confirm that polymeric and small molecule cryoprotectants, respectively, contribute to supercooled state stabilization (*SSS*), as observed by the shift of their corresponding induction bands towards lower temperatures. However, the dominant effects by which *SSS* occurs differs. Glycerol, DMSO, ethylene glycol and propylene glycol have a dominant thermodynamic influence on the system. They significantly influence the nucleation temperature, but its stochastic spread and induction band slope remains comparatively unaltered [112].

In this work, we focused on the low polymer entanglement regime, where FucoPol appears to have a Gompertzian influence on the ice nucleation temperature of water. This is a direct consequence of dynamic molecular structure, but interpretations might differ in high-entanglement regimes. However, any slight influence on nucleation temperature is overshadowed by a drastic reduction of temperature spread and stochasticity. These observations suggest that kinetic effects largely outweigh any accompanying thermodynamic effects. From the perspective of water molecules, diffusion is hindered with increasing polymer concentration, reducing the degrees of freedom of the system to induce nucleation in spatially distinct regions. It is also possible that this boundary confinement of water molecules follows a predisposed pattern, defined by the

hydrodynamic interactions of FucoPol, that originates similar final states of spatial matter disposition, thus resulting in limited, predictable ways for nucleation to occur. These reductions of molecular interactivity, bond directionality and local entropy may all contribute to the enhanced viscosity-dependent stochasticity control that is observed.

Proteins derived from mechanisms of selective pressure under sub-zero temperature habitats, such as antifreeze proteins (AFPs) and ice nucleating proteins (INPs), have independently shown traits of ice growth inhibition and promotion of nucleation, respectively. The accumulated knowledge on FucoPol now reveals that this polymer has the modulatory capability to express both – the former hereby demonstrated, and the latter observed before [117]. Moreover, the ability of FucoPol to provide different flow dynamics due to entanglement creates the possibility to obtain different behavioral regimes in ice physics, something that natural proteins are unable to achieve.

In summary, this substantially different behavior – reduced stochasticity – is hereby highlighted, to the best of our knowledge, for the first time in carbohydrate polymers, with strong practical application in the design of supercooled biopreservation protocols. FucoPol may be employed to enhance supercooling stability at non-toxic osmolalities, leading to more efficient preservation methodologies.

2.3.7 Materials and Methods

FucoPol production

FucoPol was produced by cultivation of Enterobacter A47 (DSM 23139) in a 2 L bioreactor (BioStat B-plus, Sartorius, Göttingen, Germany) under a fed-batch mode, using 40 g/L glycerol (Sigma-Aldrich, Germany) as the carbon source, according to the procedure previously described [126]. FucoPol was extracted from the cultivation broth by dia/ultrafiltration, as previously described [127] and characterized in terms of sugar monomers and acyl group compositions, and molecular mass distribution, as previously described [126]. The sample had number (M_n) and weight average molecular (M_w) weights of 1.9×10^6 Da and 3.3×10^6 ($\pm0.3\times10^6$ Da*)*, respectively, with a polydispersity of 1.70.

Sample preparation

Aqueous solutions of FucoPol were prepared at concentrations of 0.25 and 0.5 wt.% using deionized water (type II, SKU S25293) as solvent. Dissolution was performed at room-temperature with a magnetic stir bar under slow agitation, for at least 30 minutes. Dissolution was considered complete when the solution had a homogeneous beige appearance. The solution was then degassed in a vacuum chamber (Robinair VacuMaster, USA). Degassing was considered complete when no surfacing air bubbles were visible.

Setup and electronics

The INDe system, as designed by Consiglio *et al.* [112] is composed of three main components. First, a Python-based control software that runs on a Raspberry Pi 4B single board computer (Raspberry Pi Foundation, UK). Then, two temperature control assemblies, each

comprised of a two-stage thermoelectric module (CUI Devices CP60H-2 Series) and a fan-cooled CPU heat sink (Cooler Master). Lastly, a thermoelectric module controlled by a PID temperature controller (Opt Lasers, TEC-8A-24V-PID-HC-RS232), which is composed of a full bridge aluminum strain gauge (3147_0), a PhidgetBridge strain gauge DAQ (1046_0B), a thermocouple Phidget DAQ (TMP1101_0) and a USB VINT Hub (HUB0000_0), all purchased from Phidgets Inc. (CA).

Isochoric chamber preparation

The internal wall of the isochoric chamber was firstly coated with a thin layer of petrolatum (Vaseline, Unilever, UK) to avoid ice nucleation in the aluminum surface. A small amount of petrolatum (*ca.* 1mL) was inserted inside the chamber with a stainless-steel lab spatula and heated up for about 5 min using a standard heat gun. After visible melting of the petrolatum, the chamber was inverted and slowly rotated to allow for uniform coating of the walls and remove excess liquid. The chamber was then left to cool at -4ºC until the chamber was at room-temperature to allow the petrolatum coating to solidify. Then, the test sample was slowly dispensed to the lateral wall of the chamber using a syringe, carefully as to avoid insertion of undesired air bubbles or pockets. The chamber plug was wrapped with Teflon, its bottom surface also thin-coated with petrolatum and threaded into the chamber until the sealing surfaces contacted each other, after which a digital torque wrench (Yellow Jacket 60648) was used to apply a sealing torque of 40 ft-lbs.

Assay and data collection

After loading the sealed isochoric chamber between the two Peltier modules and insulated using a 3D-printed Styrofoam cap, the experiment started by holding the system at 5ºC for 5 minutes. Then, a full cycle is obtained, and is comprised of the following: cooling at 2ºC/min until nucleation is detected by an increase in strain gauge pressure, then fast warming to 5ºC and hold for 5 min to guarantee full melting of the system. Then, consecutive cycles were obtained and the corresponding nucleation temperatures recorded as a time-series.

Polymer rheology fitting

Zero-shear viscosity data on FucoPol (Figure 2.18) was adapted from Torres *et al.* [119], to which a Gompertz growth model was fit, of the form:

$$f(t) = ae^{-e^{b-ct}} \tag{2.39}$$

where a is the asymptote as $t \to \infty$, b is the displacement along the x-axis and c is the growth rate. The Gompertz growth model is a time-series applicable to measuring viscosity, η, as a function of shear stress, $\dot{\gamma}$, that is applied over time [128], [129]. However, zero-shear viscosity, η_0, is a measure of intrinsic viscosity decoupled from a time constraint, thus can be directly associated with a concentration value. Substituting mathematical parameters with rheologically meaningful variables, the fitting equation is as follows:

$$\eta_0 = abe^{-cx} \tag{2.40}$$

where x is FucoPol concentration in weight percentage, a=6201, b=5.49×10^{-6} and c=1.921 (R^2=.9985, df=14, RMSE=24.82).

Nucleation rate

Ice nucleation is a stochastic process where the number of critical size nuclei formed per unit time, the nucleation rate, $J(T)$, may be estimated by the following power-law:

$$J(T) = \gamma \Delta T^n \tag{2.41}$$

The constant cooling rate experiments presented in this study can be modelled as a non-homogeneous Poisson process [123], whereby the fraction of unfrozen samples at a given temperature, $\chi(T)$, can be related to $J(T)$ as follows:

$$\chi(T) = \exp\left(-\frac{\gamma}{\beta}\frac{(T - T_\mathrm{m})^{1+n}}{1+n}\right) \tag{2.42}$$

where T is the temperature, T_m is the equilibrium melting point, β is the cooling rate, and γ and n are empirical fitting parameters. This relation (unfrozen fraction vs. temperature) corresponds to the survivor functions shown in Figure 2.19a. Here, T_m = 0ºC due to a proven non-colligative effect on FucoPol on water thermodynamics [117], and β = 2ºC/min. See Table 2.3 for the computed values of γ and n.

Induction time

The estimated values for γ and n are better descriptors of the supercooling behavior compared to a single value for the average nucleation temperature [130]. Thus, one can accurately grasp how a thermodynamic system will behave at a defined temperature and solute concentration by plotting induction time graphs (Figure 2.19b). The mean induction time, τ, describes how long a system will remain in stable supercooled state before the first super-critical ice nucleus emerges. It is inversely proportional to the nucleation rate, $J(T)$, as follows:

$$\tau = J(T)^{-1} \tag{2.43}$$

Statistical analysis

All data was collected as three independent samples (different isochoric chambers) of, at least, N=50 observations (cycles). Results are shown as *mean* ± σ^2 for normal data and *median* ± σ^2 for *n*-modal distributed data. Statistical significance was assessed with an ordinary one-way ANOVA, with Sidak's multiple comparisons test. Significance was reported using the NEJM *p*-value threshold nomenclature as follows, from ascending order of significance: 0.12 (ns), 0.033 (*), 0.002 (**), <0.001 (***), where 'ns' means not significant for a 95% confidence interval (CI), where α=0.05.

Chapter 3

Probabilistic aspects of supercooled biopreservation

This chapter presents two studies aimed at describing the statistical aspects of ice nucleation and drawing relevant connections to the application of biopreservation. Section 3.1 formally relates metabolism reduction to supercooling stability utilizing simple Arrhenius models for metabolic rate and Poisson statistics of ice nucleation. Section 3.2 introduces a hybrid model of heterogeneous ice nucleation that captures the inherent stochasticity with Poisson statistics and the sample-to-sample variability resulting from uncharacterized trace impurities using extreme value statistics.

3.1 Relating metabolism suppression and nucleation probability during supercooled biopreservation

3.1.1 Overview

Aqueous supercooling provides a method by which to preserve biological matter at subfreezing temperatures without the deleterious effects of ice formation. The extended longevity of the preserved biologic is a direct result of a reduction in the rate of metabolism with decreasing temperature. However, because the nucleation of ice from a supercooled solution is a stochastic process, supercooled preservation carries the risk of random ice nucleation. Theoretical supercooled biopreservation research to date has largely treated these biological and thermophysical phenomena separately. Here, we apply a statistical model of stochastic ice nucleation to demonstrate how the possible reduction in metabolic rate is inherently related to supercooling stability (i.e., the likelihood of ice nucleation). We develop a quantitative approach by which to weigh supercooling stability vs. potential metabolic reduction, and further show how the stability-metabolism relationship varies with system size for two assumed modes of nucleation. Ultimately, this study presents a generalizable framework for the informed design of supercooled biopreservation protocols that considers both phase transformation kinetics and biochemical or biophysical kinetics.

3.1.2 Motivation of this study

The challenge of preserving biological matter and organisms outside their native homeostatic environments is a wide-reaching problem with relevance to food preservation[131], organ transplantation[1], reproductive science[132], tissue engineering[133] , and beyond. The myriad biochemical processes that comprise life rely on relatively controlled thermodynamic conditions (temperature, mass exchange, hydration, etc.) to proceed, and deviation from these conditions can drive spoilage in harvested foods, expiration of *ex vivo* donor organs, and potentially biological death for living organisms.

For centuries, humans have recognized that cold temperatures can stave off these negative effects (by reducing the overall rate of metabolism/biochemical reaction), leading to the widespread adoption of refrigeration. With the groundbreaking studies of Polge, Smith, and Parkes[134], among others, this technique was extended into the realm of human biology in order to preserve organs and other constructs outside of the human body.

However, while refrigeration provides extended longevity, long-term preservation nigh-universally requires temperatures well below the freezing point of water, the principal material constituent of most biological matter of interest. The crystallization of ice at subfreezing temperatures can in turn cause irreversible mechanical, osmotic, and dehydrative damage, and thus much of the past half-century of cryobiology research has sought strategies by which to mitigate the damage caused by ice, implicitly accepting its presence[135].

Recently however, the unique penchant of water to remain in a metastable liquid state below its equilibrium freezing temperature has received increasing attention as a potential method for ice-free biopreservation. This new modality, termed supercooling, has been leveraged to excellent effect in the preservation of rat livers[57], human livers[18], human cardiac microtissues[136], and various foods[137] at subfreezing temperatures yet in the absence of ice. However, the calculus required to design stable and predictable supercooling protocols, which operate at a continuous *metastable* equilibrium, is significantly different than that required to design conventional freezing protocols.

The rates of metabolism and other biological processes are temperature dependent[138], [139] and these reactions typically slow at progressively lower temperatures. It may thus seem clear that indefinitely lower temperatures should be sought for increasingly robust preservation. While this logic is reasonable from a conventional cryopreservation standpoint, wherein ice growth is considered inevitable, it is incompatible with metastable supercooled preservation, because it ignores the physics of ice nucleation, which predict that the probability for ice nucleation (which is always non-zero for a supercooled liquid) increases with both the depth below the freezing point and with the time spent in a supercooled state.

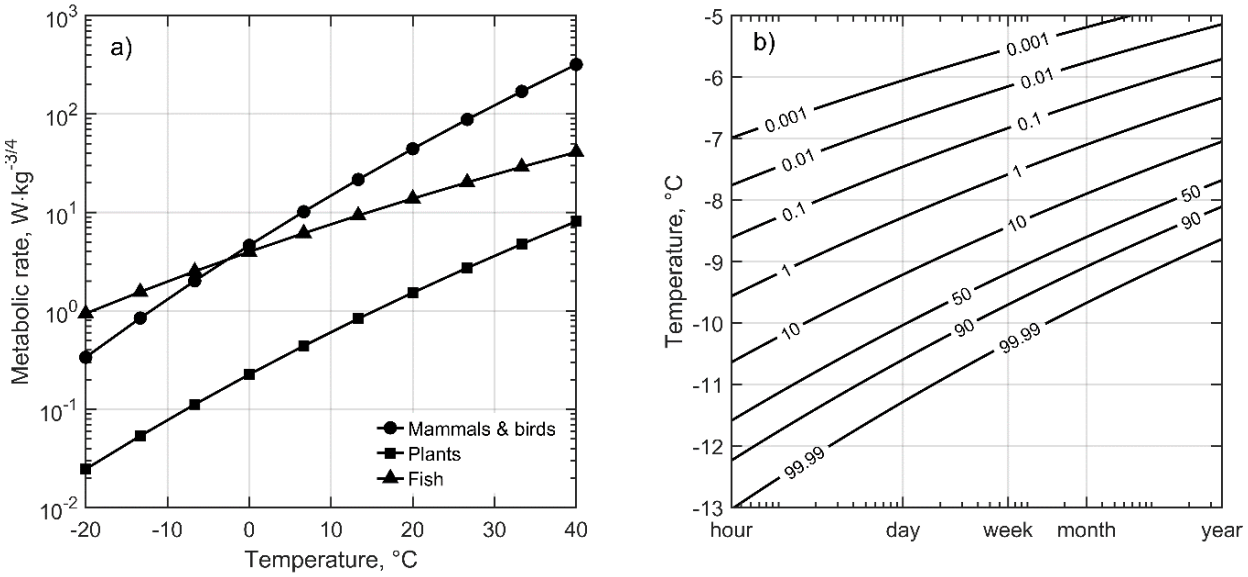

Figure 3.1: a) Temperature dependence of metabolic rate for mammals/birds, plants, and fish. Parameters from Gillooly, et al.[138]. b) Nucleation probability (%) as a function of temperature and supercooled duration for deionized water in a petrolatum-coated isochoric system[140].

A comprehensive analysis of supercooled biopreservation must thus necessarily consider both aspects of biochemical/biophysical kinetics and of ice nucleation kinetics. With this in mind, we have developed a new method of analysis that enables optimal design of cryopreservation protocols through a marriage of biology and physics.

In this study, we present a coupled analysis of metabolism and ice nucleation kinetics to describe the potential suppression of metabolic rate as a function of the probability for ice nucleation. We find that a compromise must be made between the competing design parameters (metabolic suppression, preservation duration, nucleation probability), and that this informed decision can only be made by following a multi-physics approach. Furthermore, it should be noted that while significant previous research has sought to characterize[141], [142] and optimize[143] cryopreservation protocols via various modes of thermal transport analysis, the physics relevant to the stability of supercooling are not dominated by thermal transport, but by first-nucleus nucleation kinetics, offering a less-treaded path by which to approach the problem.

Though we only explicitly consider simple models for the temperature dependence of metabolism and nucleation kinetics, the framework is entirely generalizable and can be supplemented with the development of more detailed models of biochemical/biophysical and ice nucleation kinetics.

3.1.3 Metabolic rate temperature dependence

The temperature dependence of metabolism has been characterized by Gillooly et al.[138] for several classes of organisms using an Arrhenius function of the form

$$B(T) = B_0 \exp\left(-\frac{E_i}{k_{\mathrm{B}}T}\right) \tag{3.1}$$

where B_0 is a normalization constant with units $\mathrm{W \cdot kg^{-3/4}}$ (analogous to the classical Arrhenius frequency factor), E_i is a representative activation energy for the rate-limiting enzyme-catalyzed biochemical reactions of metabolism, k_{B} is the Boltzmann constant, and T is the temperature in K.

This general model for mass-normalized resting metabolic rate was derived on the basis of allometry and biochemical reaction kinetics and fits metabolic data in a temperature range of 0°C to 40°C. In order to extend this model to supercooled temperatures (<0°C), we risk a loss of quantitative accuracy, however the general trends should not be compromised.

Figure 3.1a depicts the metabolic temperature dependence determined by Gillooly, et al.[138] for mammals/birds, plants, and fish. The respective metabolic rate parameters are provided in Table 3.1 in the Methods section

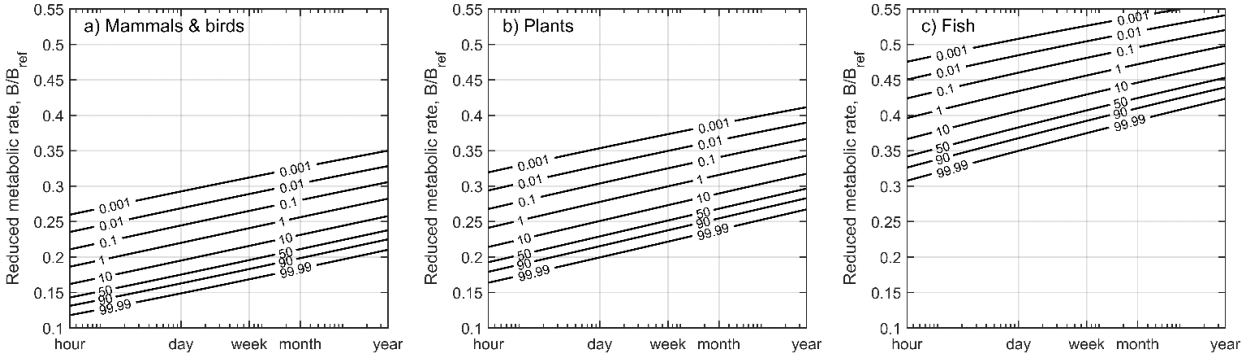

Figure 3.2: Suppression of metabolic rate as a function of nucleation probability and supercooled duration for a) mammals/birds, b) plants, and c) fish. Reduced metabolic rate calculated with reference to the rate at $T_{\mathrm{ref}} = 4°C$.

3.1.4 Nucleation statistics

The stochastic process of solid phase crystallization from a supercooled liquid may be modeled by Poisson statistics[144]–[148]. For a liquid held at a constant subcooled temperature, the probability for nucleation, p, is given by the homogeneous Poisson distribution.

$$p(T,t) = 1 - e^{-J(T)\cdot t} \tag{3.2}$$

wherein J is the system nucleation rate, T is the temperature, and t is the time spent in a supercooled state. If nucleation is initiated in the bulk of a fluid, the total system nucleation rate is dependent on the fluid volume, V, and if nucleation is initiated on the surface encapsulating the fluid, then it is dependent on the total system surface area, A. If the temperature varies spatially or temporally, the nucleation process is considered a nonhomogeneous Poisson process, and the probability can be generalized as

$$p\big(T(t,V,A)\big) = 1 - \exp\left[-\int_t \int_V \int_A J\big(T(t,V,A)\big)\, dt\, dV\, dA\right] \tag{3.3}$$

Equations for the nucleation rate are often sought through application of classical nucleation theory[149], [150], however, empirical relations may also be obtained by fitting parameterized equations to experimental data. A common form for an empirical nucleation rate equation is

$$J(\Delta T) = \gamma \Delta T^n \tag{3.4}$$

wherein $\Delta T = T_m - T$ is the depth below the equilibrium melting point, T_m, and γ and n are empirical fitting parameters[84], [151]. With this system nucleation rate, the nucleation probability at constant temperature becomes

$$p(T,t) = 1 - \exp(-\gamma (T_m - T)^n t) \tag{3.5}$$

A recent study characterized the nucleation of deionized water in an isochoric system (V=5.3mL, A=18.7cm^2) with petrolatum-coated walls[140], and average empirical nucleation parameters γ and n were evaluated as 2.20×10^{-22} and 22.06, respectively. The numerical results presented in the remainder of this study will use this data, as it is one of the few nucleation datasets available characterizing a bulk-volume non-droplet system (>1mL). However, it should be emphasized that the methodology and equations presented herein are generalized and do not depend on specific values of γ or n, or on the specific form of the nucleation rate. Thus, the present analysis can be applied to any set of nucleation data.

Figure 3.1b depicts the nucleation probability (%) as a function of temperature and supercooled duration for the characterized system. This probability-temperature-time mapping gives the basest outline of the temperatures and preservation durations that are achievable with high stability (i.e., low ice nucleation probability). For example, nucleation is predicted to occur at a rate less than 0.1% for all temperatures above -6°C and durations up to three months.

Qualitatively, we can see that for a given preservation period, the nucleation probability increases slowly up until 10% after which the trend intensifies and reaches a nearly deterministic regime (>99.99%) in a span of only 2°C. Therefore, while temperature can be varied relatively

safely below and around the region of 10% nucleation probability, any incidental fluctuations thereafter carry significantly enhanced risk for nucleation.

3.1.5 Relating metabolic suppression and nucleation probability

By solving for temperature in Equation (3.5) and substituting into Equation (3.1), we can obtain the following relation for the metabolic rate as a function of supercooled duration and nucleation probability.

$$B(t,p) = B_0 \exp\left(-\frac{E_i/k_\mathrm{B}}{T_\mathrm{m} - \left(\frac{-ln(1-p)}{\gamma t}\right)^{1/n}} \right) \tag{3.6}$$

The results of this analysis are shown in Figure 3.2a-c relative to the metabolic rate at 4°C, which is the current clinical standard for organ preservation[1] and is further commonly encountered in food refrigeration. As it may be expected, because the relative reduction in metabolic rate trends strongly with the temperature dependence (or equivalently the ice nucleation probability, as shown in the figure), organisms with larger characteristic activation energies, E_i, experience larger reductions in metabolism.

Additionally, a similar trend with nucleation probability at constant duration is observed with metabolism as with temperature. A large change in metabolism does not significantly affect the nucleation probability in the region below 10%, however, the trend quickly steepens, and for nucleation probabilities greater than 10%, further change in metabolic suppression is accompanied by large changes in probability and swift entering of a quasi-deterministic regime.

3.1.6 Scaling with system size

The experimental data obtained by Consiglio, et al.[140] and used in this study characterized the nucleation rate of a specific 5.3 mL isochoric system, and further investigation is required to identify the mode(s) of nucleation and determine how the nucleation rate scales with volume and container surface area. Despite this gap in our current knowledge however, we can still conject how the nucleation phenomena (probability-time-temperature relation) would scale by assuming that only surface-mediated *or* volumetric nucleation will dominate.

Assuming this independent scaling (i.e., that only one nucleation mode is applicable), the nucleation rate would become

$$J(V,\Delta T) = \frac{V}{V_0}\gamma \Delta T^n \quad \text{or} \quad J(A,\Delta T) = \frac{A}{A_0}\gamma \Delta T^n \tag{3.7}$$

wherein V_0 is the volume (5.3mL) and A_0 the surface area (18.7cm^2) of the chamber from Consiglio et al.[140], and V and A are the volume and surface area of a hypothetically scaled system.

The relation between temperature, supercooled duration, and system size for two nucleation probabilities (0.001% and 10%) is shown in Figure 3.3a. The indicated volumes correspond to the volumetric scaling assumption, and conversely, the indicated surface areas correspond to the surface area scaling assumption.

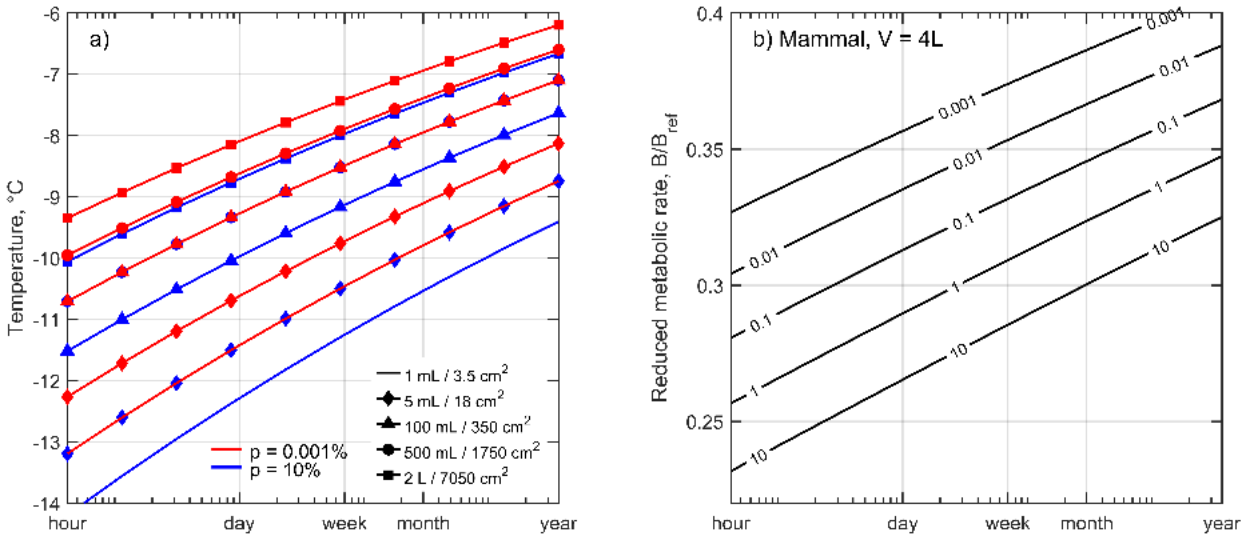

Figure 3.3: a) Scaled temperature vs. time dependence for nucleation probabilities of 0.001% (red) and 10% (blue). Indicated volumes correspond to volume scaling assumption. Indicated areas correspond to surface area scaling assumption. b) Dependence of mammalian metabolic rate on supercooled duration and nucleation probability for a hypothetical 4L system applicable to human organ preservation (volumetric scaling assumed).

3.1.7 Towards the design of supercooled biopreservation protocols

We may now seek to consider specific applications using these new design tools, and one of the most promising applications is full organ supercooling for transplantation purposes. By applying the simple scaling analysis above, we can estimate the metabolic suppression possible in a petrolatum-coated isochoric system of arbitrary size. Shown in Figure 3.3b is the dependence of mammalian metabolism on nucleation probability and supercooled duration for a 4L system (volume scaling assumed). This volume is expected to be able to contain any mammalian organ, excluding perhaps the lungs. We can see that a two-thirds reduction in the metabolic rate ($B/B_{ref} \approx$ 1/3) may be achieved compared to preservation at 4°C for a preservation period of one week and nucleation probability of only 0.01%.

In the case of full organ preservation, given the extreme value of transplantable donor organs (the average heart transplant costed more than $1M in 2017[1]), minimization of nucleation

probability must be prioritized since any formation of ice and freezing of tissue risks lethal and irreversible damage.

On the other hand, for cell suspensions divided into a multitude of individual vials, a smaller margin of error may be viable since 100% survival is often not necessary and enhanced metabolic suppression may be of greater value. The 5mL isochoric system from Consiglio, et al.[140] may be a well-suited volume for cell preservation. In this case, we can reference Figure 3.2c directly and observe that nearly a three-quarter reduction in the metabolic rate compared to 4°C may be obtained for preservation of one week and nucleation probability of 0.1%.

The preservation of food may likewise not demand total assurance of the avoidance of ice nucleation if a certain loss is acceptable. Future scenario-specific analyses may seek an optimal protocol that balances nucleation frequency with extension of shelf life. For example, if it is currently impossible to preserve sashimi-grade tuna for longer than 72 hours, a protocol that enables longer preservation times but with a 50% chance of ice nucleation may still be viable and valuable, generating 50% high-quality survival of a yield that otherwise may be entirely lost.

For each of these scenarios, marriage of the modeling methodology herein to experimental validations in applied biopreservation should be sought in future work, and could be leveraged to develop standards for acceptable thresholds of nucleation probability suited to each application.

3.1.8 Conclusions

Although this study has only related the temperature dependence of nucleation kinetics with metabolism as whole, the methodology can be extended to any temperature-dependent biochemical or biophysical process of interest. For example, the relation provided in Equation (3.6) can be used to characterize any first-order chemical reaction with known pre-exponential factor and activation energy. In addition to metabolic rate, the temperature dependence of membrane processes, enzymatic activity, ATP depletion, and other processes related to hypothermia and ischemia-induced damage would be of interest for low-temperature biopreservation. These processes might possess temperature dependencies ill-described by the Arrhenius function of Equation (3.1), and in this case an alternative temperature-dependent rate equation such as the Eyring equation from transition state theory[139] may be substituted in its place.

Furthermore, as discussed in previous sections, the nucleation data used in this study is of limited scope. In order to rigorously quantify nucleation probabilities applicable to real applications, further investigations should seek to characterize the volumetric and surface scaling, and nucleation data reflecting the precise preservation medium to be employed should be used (as opposed to pure water data).

Future work should also seek to experimentally distill the metabolism reduction described herein into more actionable temperature-dependent metrics, such as gross organ, tissue, or cell viability, degree of food expiration, etc., and thereby validate directly the results of this modeling approach.

In conclusion, we have shown that, armed with knowledge of the temperature dependence of the metabolic rate and rate of ice nucleation, the safety (against ice nucleation) and effectiveness (reduction of metabolism) of a proposed supercooled biopreservation protocol can be quantitatively characterized. We find that a compromise must be made amongst the various competing design parameters since metabolism decreases monotonically with temperature and conversely the probability for ice nucleation from a supercooled liquid increases monotonically with temperature and supercooled duration.

3.1.9 Methods

The metabolic rate parameters B_0 and E_i, summarized in Table 3.1, are computed from data in Figure 1 of Gillooly, et al.[138].

Table 3.1: Metabolic rate parameters from Gillooly, et al.[138].

Organism	**ln B_0 (W·kg$^{-3/4}$)**	**E_i (eV)**
Mammals & birds	34.67	0.78
Plants	26.55	0.66
Fish	19.65	0.43

Nucleation rate parameters were computed by parametric inference of data from constant cooling rate nucleation experiments[140]. The survivor curve representation of this data (unfrozen fraction vs. temperature) corresponds to the cumulative distribution of a nonhomogeneous Poisson process, the rate parameter of which is the nucleation rate. By assuming a form for the nucleation rate (such as in Equation (3.4)), a distribution may be fitted to the data to obtain the empirical parameters.

This empirical fitting method may be applied to arbitrary nucleation experiments reporting unfrozen fraction vs. temperature survivor curves, and the application of the analysis presented herein to the design of specific supercooling protocols should use nucleation data that represents the precise system of interest, in order to capture surface-mediated nucleation effects specific to that system.

3.2 Extreme value statistics of heterogeneous ice nucleation

3.2.1 Overview

The propensity of water to remain in a metastable liquid state at temperatures below its equilibrium melting point holds significant potential for cryopreserving biological material such as tissues and organs. The benefits conferred are a direct result of progressively reducing metabolic expenditure due to colder temperatures while simultaneously avoiding the irreversible damage caused by the crystallization of ice. Unfortunately, the freezing of water in bulk systems of clinical relevance is dominated by random heterogeneous nucleation initiated by uncharacterized trace impurities, and the marked unpredictability of this behavior has prevented implementation of supercooling outside of controlled laboratory settings and in volumes larger than a few milliliters. Here, we develop a statistical model that jointly captures both the inherent stochastic nature of nucleation using conventional Poisson statistics as well as the random variability of heterogeneous nucleation catalysis through bivariate extreme value statistics. Individually, these two classes of models cannot account for both the time-dependent nature of nucleation and the sample-to-sample variability associated with heterogeneous catalysis, and traditional extreme value models have only considered variation of the characteristic nucleation temperature. We conduct a series of constant cooling rate and isothermal nucleation experiments with physiological saline solutions and leverage the statistical model to evaluate the natural variability of kinetic and thermodynamic nucleation parameters. By quantifying freezing probability as a function of temperature, supercooled duration, and system volume, while accounting for nucleation site variability, this study also provides a basis for the rational design of stable supercooled biopreservation protocols.

3.2.2 Motivation of this study

Understanding how solid phases nucleate from the melt is a complex problem of wide-spread relevance. The nucleation of ice, in particular, governs the formation of clouds in our atmosphere[50], plays a key role in the survival of organisms living in extreme climates[152], [153], and determines the quality of our refrigerated and frozen foods[154], [155].

Ice nucleation also sets the current limit for the preservation of life saving organs for transplantation[62]. The clinical standard for *ex vivo* storage of organs involves placing an organ on ice (at roughly 0-4°C) and only enables brief periods of preservation (4-6 hours for the heart and 12-18 hours for the liver[156]) before the organ expires and is unfit for transplantation. Due to the Arrhenius-like nature of metabolic reactions, reducing the preservation temperature further could extend these durations, and as result, remove significant logistical hurdles, improve immunological matching and expand access to life-saving organs[157]. Critically however, the freezing point of water (0°C) represents a fundamental barrier, as freezing of biological systems is often fatal. Reducing the temperature of preservation below 0°C without ice formation thus holds significant implications for global health.

Despite manifesting at the human and even global scale, the fundamental process of nucleation involves the coordinated dynamics of a handful of molecules occurring at or even below the nanoscale[50], [158]. This immense separation of scales results in making predictions about how

nucleation occurs extremely difficult. Additionally, nucleation occurs almost always heterogeneously, which means that not only the physics of the liquid itself must be understood but also the interactions with all surfaces it finds itself in contact with. The result is that, depending on the catalyzing efficiency of the nucleating surfaces present in a given volume of water, ice may nucleate anywhere from just below the equilibrium melting point of 0°C down to the homogeneous nucleation limit around –40°C (pure water at atmospheric pressure)[158]. Likewise, when held at a constant subcooled temperature, water may freeze within seconds or remain in a metastable liquid state for years at a time.

In theory, if one were to characterize every surface present in a system, then the nucleation behavior could be predicted for that system and subsequent systems of the same heterogeneous composition. This has been the approach of many researchers, for example, in the atmospheric sciences, who have thoroughly quantified the nucleation behavior of many common aerosol particulate materials in order to understand larger phenomena such as cloud formation[71]. These studies often seek to describe the time dependent nature and inter-sample variability observed in freezing experiments, capturing active site variability through distributions of contact angle, surface area, or combinations thereof[159]–[162].

This scenario is uncommon however, since the typical engineer seeking to predict the freezing behavior of arbitrary systems cannot realistically characterize each and every system, and especially not *in situ*[163]. What's more, nucleation is known to be sensitive to variation in impurities to such an extent that the nucleation behavior of samples taken from a single source may even vary significantly from one another[164]. This phenomenon is known as non-self-averaging behavior and results from catalyst sites possessing a wide distribution of nucleation rates[164]–[166]. Since the nucleation rate is proportional to the exponential of the nucleation barrier, large variations in characteristic nucleation efficiency between active sites can result in one or a few active sites making up the entirety of the total system nucleation rate. This is thought to be responsible for the common experimental observation of nucleation occurring repeatably at individual sites on a surface[167], [168].

The recognition that the single most potent active site may be responsible for nucleation is equivalent to the so-called weakest-link hypothesis common in the study of fracture mechanics[169] (i.e., a chain is only as strong as its weakest link, and similarly, a material placed under stress will fracture due to its weakest defect). The weakest link analogy is an example of the statistical theory of extreme values[170], which describes situations with a large number of random variables, N, for which we are interested in the probability distribution of the largest (or smallest) of the N random variables. Extreme value statistics is also used to model, for example, extreme weather and financial events[170].

In the study of nucleation, the smallest nucleation barrier, highest nucleation temperature, or shortest nucleation induction time are relevant extreme variables. Extreme value theory can thus be recognized as the foundation of the classic singular model for heterogeneous nucleation which describes nucleation by a single characteristic nucleation temperature[171], [172]. The singular model has been found to describe the distribution of nucleation temperature among a collection of transiently cooled droplets and to predict how nucleation temperature changes with the size of droplets[173], [174].

Although this formulation of the classic singular model does not describe a time dependence of nucleation, extreme value theory has also been applied to experiments that measure the time until nucleation occurs for droplets held at a constant temperature. For systems exhibiting non-self-averaging behavior, the measured nucleation rate of a collection of droplets strays from the exponential decay predicted by Poisson statistics, instead becoming a stretched exponential[175].

Ultimately, the randomness of nucleation represents a far-reaching scientific challenge and specifically poses significant barriers to the deployability of supercooling for the preservation of biological systems in clinical settings. While the inherent stochastic nature of nucleation results in a finite probability for nucleation at all times when in a supercooled metastable state, at low undercoolings, and when adequately characterized, the probability is vanishingly small[22]. On the other hand, the heterogeneous catalysis of nucleation by random active sites adds an additional layer of unpredictability to supercooling stability. In even the purest volumes of water, the presence of minute insoluble impurities as well as certain soluble macromolecules can result in widely varying freezing behavior even in samples from the same source.

In this study, we perform an extensive series of both constant cooling rate and isothermal ice nucleation experiments, and develop a statistical model of nucleation rooted in both the observed inter-sample variability and the intra-sample stochasticity. The time and temperature dependent stochasticity is captured by conventional Poisson statistics, and the active site variability is captured by a new bivariate extreme value model describing variability of both the kinetic and thermodynamic heterogeneous nucleation parameters.

This article is structured as follows. In Section 3.2.3, an overview of the constant cooling rate and isothermal nucleation experiments is provided. In Section 3.2.4, the probability distributions that describe nucleation stochasticity are derived from Poisson statistics, and in Section 3.2.5 extreme value statistics are introduced and formally connected to Poisson statistics in order to describe heterogeneous nucleation variability.

In Section 3.2.6, the results from the constant cooling rate experiments are presented, which are then, in Section 3.2.7, evaluated within the new extreme value statistics framework. The model is then validated by assessing its ability to predict how the nucleation behavior scales with system size in Section 3.2.8, and by measuring isothermal nucleation probabilities Section 3.2.9.

By developing a unified framework for characterizing both sources of randomness associated with nucleation processes, this study uncovers fundamental properties of heterogeneous nucleation and provides a basis for the rational design of safe and robust supercooled biopreservation protocols.

3.2.3 Nucleation experiments

The principal goal of supercooled biopreservation is to stably hold biological material in a supercooled liquid state in order to suppress metabolic activity and achieve a certain degree of suspended animation. Nucleation is a random process and directly characterizing supercooling stability would require conducting experiments under the experimentally relevant timescales (days, possibly weeks) and repeating experiments many times in order to build statistical confidence. Because this is generally impractical, we may alternatively seek to indirectly predict

supercooling stability by characterizing the system nucleation rate. The nucleation rate describes the rate of formation of critical ice clusters in a supercooled liquid and is related to nucleation probability under the framework of Poisson statistics (see Section 3.2.4).

Experiments for characterizing nucleation rates generally fall under two categories: 1) isothermal and 2) constant cooling rate. In isothermal experiments, a sample is quickly quenched to and held at a constant supercooled temperature, and the time at which nucleation occurs is recorded. In constant cooling rate experiments, the temperature of a sample is continually decreased at a constant rate, and the temperature at which nucleation occurs is recorded. Through the application of Poisson statistics, equivalent information (namely the nucleation rate) can be obtained from these two techniques. In this study, constant cooling rate experiments were chosen for collecting the bulk of nucleation data since they allow data to be collected more quickly. Since isothermal supercooling experiments replicate the scenario employed during supercooled biopreservation, an additional campaign of isothermal experiments was performed at various temperatures and compared to the statistical predictions of the model formed from the constant cooling rate data.

The experimental setup employed in this study has been previously described by Consiglio et al.[176] and consists of a rigid Al-7075 chamber with petrolatum coated surfaces (Vaseline, Unilever, UK). The chamber is filled completely with liquid, excluding all bulk gas. The combination of hydrophobic surfaces and rigid confinement has been found to enhance the stability of supercooled solutions[46], [176]–[178] and is employed here since the practical objective of this work is designing robust supercooled biopreservation protocols[22], [136]. We also hypothesize that these conditions suppress nucleation from the container surface and from external perturbations and thus isolate the effect of nucleation catalysts present in the solution. The petrolatum coating, which is freshly applied before each experiment, has the additional benefit of providing maximal consistency across repeated experiments and devices. All experiments were conducted with phosphate-buffered saline (PBS (1X) ID: 10010023, Thermo Fisher Scientific, USA), the melting point of which is approximately –0.5°C. This solution has a physiological osmolarity of 280 - 315 mOsm/kg, which mimics many of the commonly utilized cold storage organ preservation solutions.

Within each constant cooling rate experiment, the temperature is lowered at a constant rate. Nucleation is monitored via an externally mounted strain gauge that enables detection of the pressure rise attributed to ice growth within the confined volume. Upon detection of nucleation, the system is rewarmed to +5C to melt the ice and re-equilibrate the system. After a rewarming hold period of five minutes, the cooling cycle is repeated. This process is repeated multiple times in order to construct an empirical distribution of nucleation temperatures. Each CCR experiment consisted of an average of ~80 freeze/thaw cycles.

The primary constant cooling rate experiments were conducted in a 5ml chamber (V=5.3ml, SA=19cm^2) with a cooling rate of 2°C/min. A second set of constant cooling rate experiments were conducted in a 20ml chamber (V=21.2ml, SA=41.9cm^2) with a cooling rate of 1°C/min. In order to study the variability of heterogeneous catalysts present across the samples, these experiments were repeated a total of 23 times in the 5ml systems (i.e., 23 different 5 mL samples underwent ~80 freeze/thaw cycles each) and 10 times in the 20ml systems (i.e., 10 different 20 mL samples

underwent ~80 freeze/thaw cycles each). Isothermal experiments were conducted in the 5ml systems at temperatures of –12°C (n=10), –13°C (n=6), and –14°C (n=18). A cutoff of two hours was imposed in order to maintain experimental throughput.

Since this study aims to develop methods for informing design of supercooled biopreservation protocols, it is important to consider how these experiments, which only investigate the supercooling of physiological solutions, relate to supercooling of an organ. A convenient property of biological materials is that they ae generally poor ice nucleating substrates and only freeze at low temperatures or under the influence of external ice[179], [180]. There are of course notable exceptions of certain bacteria[5], proteins[6] and other macromolecules[181], however these are generally not present in mammalian systems. This poor nucleating property enables us to study the nucleation behavior of solutions and containers with the understanding that this behavior will extend to equivalent systems that also contain biological material.

3.2.4 Poisson statistics of nucleation processes

Nucleation, considered here as the steady state formation of stable solid clusters, is a stochastic process with individual nucleation events being independent of each other and of previous events. From a probabilistic standpoint, it can be shown that nucleation in an ensemble of supercooled molecules is governed by Poisson statistics[148]. This yields the result that, for a volume of uniform temperature and composition, the probability of observing k nucleation events in the time interval $[0, t]$ is given by the Poisson distribution:

$$P_k(t) = \frac{(\lambda t)^k}{k!} e^{-\lambda t} \tag{3.8}$$

where λ is a rate parameter $[s^{-1}]$and t is time $[s]$. Since the rate parameter is constant here, Equation (3.8) describes a homogeneous Poisson process (note that this is distinct from the homogeneous descriptor of nucleation occurring in the bulk of a fluid and not at an interface). From this, we can find that the probability of zero nucleation events ($k = 0$) occurring in a system with constant nucleation rate J $[s^{-1}]$ follows an exponential decay:

$$P(t) = \exp(-Jt) \tag{3.9}$$

This probability distribution is shown in Figure 3.4a as a function of time for three different nucleation rates. If the nucleation rate is not constant but instead varies with time, we have a nonhomogeneous Poisson process, and the probability of zero nucleation events becomes

$$P(t) = \exp\left(-\int_0^t J(\tau) d\tau \right) \tag{3.10}$$

In certain scenarios, the temperature is lowered at a constant cooling rate, $\dot{T} = |dT/dt|$, and we can define the probability as a function of temperature instead of time by integrating the nucleation rate in temperature, beginning at the equilibrium melting temperature, T_m.

$$P(T) = \exp\left(-\frac{1}{\dot{T}}\int_{T_\mathrm{m}}^{T} J(T')dT'\right) \tag{3.11}$$

In statistical terms, this probability distribution is known as the survival function, S, which is defined as $S_X(x) = \Pr(X \geq x)$ and represents the probability that a random variable, X, will take on a value greater than or equal to x. In the context of nucleation, the survival function represents the probability that nucleation does not occur before a given time (Equation (3.9) for constant temperature) or degree of supercooling (Equation (3.11) for constant cooling rate). The survival function is related to the cumulative distribution function (CDF), $F_X(x)$, by $F_X(x) = 1 - S_X(x)$.

The probability density function (PDF) is another useful statistical function and is defined as $f_X(x) = \frac{d}{dx}F_X(x)$. Since the probability for a continuous random variable to take on any one particular value is zero, in the context of nucleation, the PDF represents the relative likelihood that nucleation will occur around a given temperature (for constant cooling rate) or around a certain time (at constant temperature). For a constant cooling rate process, the PDF is given by

$$f(T) = \frac{1}{\dot{T}}J(T)\exp\left(-\frac{1}{\dot{T}}\int_{T_\mathrm{m}}^{T} J(T')dT'\right) \tag{3.12}$$

In order to solve for the freezing probability distribution, a relation for the nucleation rate $J(T)$ is needed. Classical nucleation theory (CNT) provides a framework for describing the nucleation process[182] and can be used to describe the heterogeneous nucleation rate [$\mathrm{m^{-2}\,s^{-1}}$] as[183], [184]

$$J(T) = n_s\frac{k_\mathrm{B}T}{h}\exp\left(-\frac{\Delta F_\mathrm{diff}}{k_\mathrm{B}T}\right)\exp\left(-\frac{\Delta G^*_\mathrm{hom} f_\mathrm{het}}{k_\mathrm{B}T}\right) \tag{3.13}$$

where n_s is the number of water molecules per unit area in contact with the ice nucleus, k_B is Boltzmann's constant, h is Planck's constant, ΔF_diff is the energy of activation for a water molecule to cross the water/ice interface, ΔG^*_hom is the homogeneous free energy of formation for a critical ice embryo, and f_het is a geometric compatibility factor describing the reduction of the free energy barrier due to the presence of an ice nucleating surface.

Many of the terms in Equation (3.13) are independent of or only weakly dependent on temperature, and the nucleation free energy barrier, ΔG_hom, often dominates the variation of the nucleation rate with temperature[185]. By grouping together the kinetic terms and approximating

the temperature dependence of the free energy barrier as $\Delta G^*_{\mathrm{hom}} \sim (T\Delta T)^{-2}$, we can arrive at an oft employed two-parameter relation[87], [186]:

$$J(T) = A \exp\left(\frac{-B}{T^3 \Delta T^2}\right) \tag{3.14}$$

where $\Delta T = T_{\mathrm{m}} - T$ is the degree of supercooling, and A and B are constants. The parameter A is often referred to as the pre-exponential term or kinetic factor [s^{-1}], and the parameter B as the nucleation barrier or thermodynamic factor [K^5]. With this relation, we arrive at cumulative distribution and probability density functions, respectively, for a constant cooling rate process:

$$F(T|A,B) = \exp\left[-\frac{A}{\dot{T}} \int_{T_{\mathrm{m}}}^{T} \exp\left(\frac{-B}{T'^3 \Delta T'^2}\right) dT'\right] \tag{3.15}$$

$$f(T|A,B) = \frac{A}{\dot{T}} \exp\left(\frac{-B}{T^3 \Delta T^2}\right) \exp\left[-\frac{A}{\dot{T}} \int_{T_{\mathrm{m}}}^{T} \exp\left(\frac{-B}{T'^3 \Delta T'^2}\right) dT'\right] \tag{3.16}$$

The cumulative distribution and probability density functions for a characteristic system with $T_{\mathrm{m}} = 0°\mathrm{C}$ and nucleation parameters $A = 1.5 \times 10^{19} \mathrm{s}^{-1}$ and $B = 1.5 \times 10^{11} \mathrm{K}^5$ are shown in Figure 3.4b. The average nucleation temperature and standard deviation for this process are –13.7°C and 0.2°C, respectively.

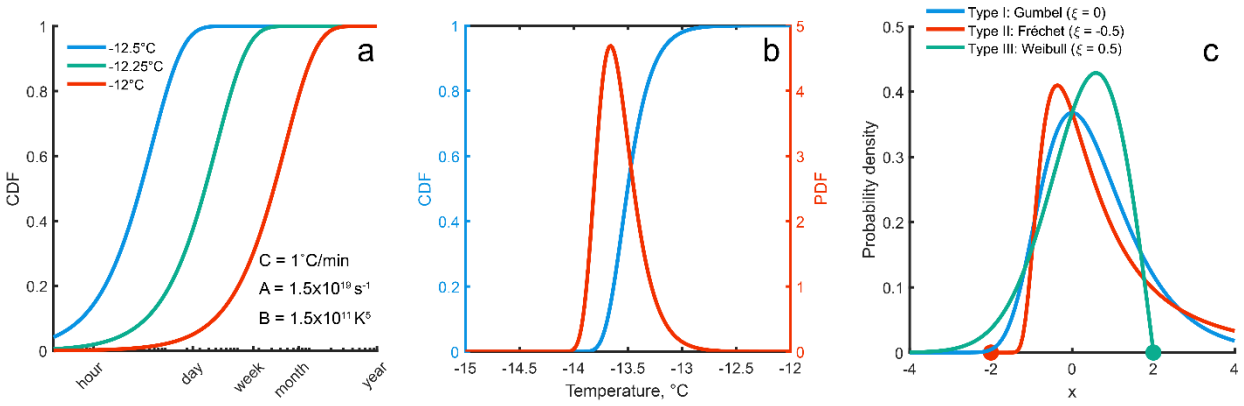

Figure 3.4: Probability distribution functions. a) Isothermal cumulative distribution functions for a system with equilibrium melting temperature $T_{\mathrm{m}} = 0°C$ and nucleation parameters $A = 1 \times 10^{19}\ s^{-1}$ and $B = 1.5 \times 10^{11}\ K^5$ at temperatures –12.5°C (blue), –12.25°C (green), and –12°C (red), computed from Equations (3.9) and (3.14). b) Cumulative distribution (blue) and probability density (red) functions for same system as in panel a) cooled at a constant rate of 1°C/min, computed from Equations (3.15) and (3.16), respectively. c) Example Type I: Gumbel

(blue), Type II: Fréchet (red), and Type III: Weibull (green) generalized extreme value probability density functions (Equation (3.20)) for $\boldsymbol{\mu} = \mathbf{0}$ and $\boldsymbol{\sigma} = \mathbf{1}$.

The moments of a probability distribution provide useful quantitative measures about the shape of the distribution. The first moment describes the expected value (i.e., mean), the second moment is related to the variance, and the third moment is related to the skewness. The n-th central moment is described generally by

$$\mu_n = \int_{-\infty}^{\infty} x^n dF(x) = \int_{-\infty}^{\infty} x^n f(x) dx \tag{3.17}$$

The goal of nucleation experiments, to quantify the nucleation rate, is achieved by fitting the cumulative distribution function from Equation (3.15) to an empirical distribution of nucleation temperatures from a constant cooling rate experiment. This nucleation rate can then be used with Equation (3.10) to predict the probability that this system would freeze for an arbitrary thermal history as a function of time.

Although this procedure can be used to accurately characterize individual samples, its extension to the prediction of freezing probabilities for arbitrary systems (of nominally equivalent composition) is complicated by the fact that nucleation in real bulk systems is a heterogeneously catalyzed process. Samples of water, even when extensively purified[187], inevitably contain varying amounts and populations of heterogeneous nucleating agents, and this often results in different nucleation rates between seemingly identical samples[164], [165].

In order to characterize the freezing probability for heterogeneous nucleation, one would ideally know properties of every nucleating agent present. The total system nucleation rate could then be expressed as the sum of the individual rates:

$$J(T) = \sum_{i}^{N} A_i \exp\left(\frac{-B_i}{T^3 \Delta T^2}\right) \tag{3.18}$$

where N is the total number of active sites and A_i and B_i are the nucleation parameters of the i-th nucleating particle. Nucleating particles often contain surface features such as crevices that have an outsized contribution to the particle's total nucleation rate. In this case, the particle's total surface area is not a relevant parameter. Otherwise, the term A_i would contain the total surface area of the nucleating particle. Equation (3.18) can be used in place of the single nucleation rate from Equation (3.14) in the above statistical relations.

This approach has been widely adopted by the atmospheric science community to characterize the nucleating behavior of specific aerosol materials[184]. In these experiments, precise quantities of rigorously characterized material are added to the system. The nucleation rate of this system

can then be measured, and any observed difference can be attributed to the added material if the nucleating agents result in nucleation at higher temperatures than the base solution[188]–[190].

Unfortunately, this methodology cannot be applied if the purity of a solution or exact properties of all active heterogeneous catalysts are not known (such as the case with a bottle of standard laboratory-grade phosphate-buffered saline). Additionally, if the nucleation rate is strongly dependent on surface features as well as surface chemistry, the observed nucleation rate between samples of the same absolute composition may not be consistent[168], [191]. Very few tools are at our disposal for predicting nucleation in these instances. In the following section, we leverage the observation that nucleation often occurs at the single most potent active site[165], [172], [192], enabling the application of methods from extreme value statistics for describing the effect of random impurities and circumventing the need of fully characterizing every impurity.

3.2.5 Extreme value statistics of heterogeneous nucleation

Any model of heterogeneous nucleation must describe, in some manner, the inherent variability of nucleation active sites that contributes to the total system nucleation rate as described in Equation (3.18) [193]. When specified quantities of characterized impurities are added to a solution, the nucleation parameters are known (i.e., can be characterized). Conversely, in the case of a system containing uncharacterized impurities, the total number of active sites, N, as well as the nucleation parameters, A and B, become random variables[165].

A common experimental observation is that ice nucleates repeatably at individual sites, such as a scratch on a container's surface[167], [187]. As discussed earlier, this behavior is characteristic of quenched disorder and often leads to non-self-averaging behavior. The result is a nucleation behavior varying randomly between seemingly identical samples.

The statistical theory of extreme values has been proposed to describe this nucleation phenomenon and is at the core of first statistical theory of heterogeneous nucleation[171], [172], [174]. The theory is described generally as follows: a series of independent and identically distributed random variables, $X_1, \dots, X_n$, is described by the cumulative distribution function, $F_X(x)$, and maximum, $M_n = \max(X_1, \dots, X_n)$. Although the distribution of the maximum value of this set is exactly given by $\Pr(M_n \leq z) = [F(z)]^n$, the distribution $F_X(x)$ is often not known such as in the case of heterogeneous nucleation with a distribution of active sites. In the asymptotic limit of $n \to \infty$ however, the distribution of the maximum is described, regardless of the underlying distribution $F_X(x)$, by a finite family of distributions known as the generalized extreme value (GEV) distribution[170], [194]:

$$G(x) = \exp\left\{-\left[1 + \xi\left(\frac{x-\mu}{\sigma}\right)\right]^{-\frac{1}{\xi}}\right\} \tag{3.19}$$

$$g(x) = \frac{1}{\sigma}\left[1 + \xi\left(\frac{x-\mu}{\sigma}\right)\right]^{-\left(1+\frac{1}{\xi}\right)} \exp\left\{-\left[1 + \xi\left(\frac{x-\mu}{\sigma}\right)\right]^{-\frac{1}{\xi}}\right\} \tag{3.20}$$

Here, $G(x)$ is the cumulative distribution function, $g(x)$ is the probability density function, and μ, σ, and ξ are the location, scale, and shape parameters, respectively. The specific distribution is determined by the shape parameter, which governs the tail behavior. While the Gumbel distribution is unbounded in both limits, the Weibull distribution has an upper bound and the Fréchet distribution a lower bound. The sub-classes of the GEV distribution are summarized in Table 3.2 and depicted in Figure 3.4c for location and scale parameters $\mu = 0$ and $\sigma = 1$, respectively. Even though we cannot realistically know the complete distribution of impurities present in a solution, in the asymptotic limit, the distribution of most potent sites is predicted to follow one of these three distributions.

In order for extreme value theory to be applied to heterogeneous nucleation experiments, a few additional assumptions must first be introduced: 1) the variability in the number of active sites between systems is much smaller than the total number of active sites, and 2) the underlying distribution of active sites is the same between systems. These assumptions are reasonable for individual samples taken from the same source.

Table 3.2: Generalized extreme value distribution sub-types.

Type	Name	Shape factor	Cumulative distribution function	
I	Gumbel	$\xi = 0$	$G(x) = \exp\left[-\exp\left(-\frac{x-\mu}{\sigma}\right)\right]$	(3.21)
II	Fréchet	$\xi > 0$	$G(x) = \begin{cases} \exp\left[-\left[1 + \xi\left(\frac{x-\mu}{\sigma}\right)\right]^{-1/\xi}\right] & x > 0 \\ 0 & x \leq 0 \end{cases}$	(3.22)
III	Weibull	$\xi < 0$	$G(x) = \begin{cases} \exp\left[-\left[1 + \xi\left(\frac{x-\mu}{\sigma}\right)\right]^{-1/\xi}\right] & x < 0 \\ 1 & x \geq 0 \end{cases}$	(3.23)

Determining the relevant extreme variables

The specific physical quantity that is chosen as the extreme variable confers additional constraint on the problem. For example, the classic singular model of nucleation prescribes a characteristic activation temperature to each active site, and thus the nucleation temperature is the extreme variable. In reality, nucleation is stochastic and does not occur at a single temperature but rather over a distribution of temperatures, even for a single active site. For extreme value statistics to be a good descriptor of the nucleation temperature, the variability of nucleation temperature for individual active sites should be small in comparison to the variability of characteristic nucleation temperature between systems. This is the case for the system studied here, as seen in Figure 3.5 and Figure 3.6, where the standard deviation of nucleation temperatures for a single sample is on average about 0.33°C while the standard deviation of nucleation temperatures between samples is approximately 1.5°C.

The classic singular model is typically applied to data from constant cooling rate experiments in which nucleation temperature is the measured quantity. Alternatively, in the case of isothermal experiments, the relevant extreme variable is the nucleation induction time, and the active site with the minimum characteristic induction time is responsible for nucleation[195]. For extreme value statistics to have reasonable predictive power here, the spread of induction times for individual active sites caused by inherent stochasticity should likewise be small compared to the spread of induction times between samples.

These two applications of extreme value statistics are the most readily applied since the extreme variable is a measured quantity. Alternatively, we can consider the molecular mechanisms of nucleation and instead of attributing nucleation to the active site with the highest nucleation temperature or shortest nucleation induction time, we can describe the potency of the active site by the nucleation rate itself. In this way, nucleation is attributed to the active site with the largest nucleation rate.

In the two-parameter nucleation rate relation described in Equation (3.14), the nucleation barrier, B, is exponentiated, and as such, the nucleation rate is much more sensitive to B than it is to the pre-exponential factor, A. A theoretical extreme value analysis of nucleation performed by Sear[164], [165] held the pre-exponential factor constant and treated the nucleation barrier as the extreme variable. This approach is convenient since it reduces the problem to a single variable, however it is not consistent with the common experimental observation that the spread of nucleation temperatures is rather constant regardless of the temperature at which nucleation occurrs[196]. Both the expected value and standard deviation of the nucleation temperature for a constant cooling rate experiment, as computed from the first and second moments of the probability distributions, are dependent on pre-exponential and nucleation barrier parameters. Therefore, both nucleation parameters must vary for the standard deviation to remain the same as the nucleation temperature changes.

Because singular extreme value models cannot suitably capture the time and temperature dependence of nucleation, nor the variability of the nucleation rate, we propose a bivariate scheme that treats both the nucleation temperature and the nucleation barrier parameter, B, as extreme quantities. These parameters are intimately related, with higher nucleation barriers yielding lower

nucleation temperatures. As described in Section 3.2.4, these variables are formally related through Poisson statistics by the average nucleation temperature, which is defined as the first central moment of the constant cooling rate probability distribution function:

$$\langle T_{\mathrm{f}} \rangle = \int_{-\infty}^{\infty} \frac{A}{\dot{T}} \exp\left(\frac{-B}{T^3 \Delta T^2}\right) \exp\left[-\frac{1}{\dot{T}} \int_{T_{\mathrm{m}}}^{T} A \exp\left(\frac{-B}{T'^3 \Delta T'^2}\right) dT'\right] T \, dT \tag{3.24}$$

However, from this equation we can see that the nucleation temperature is not only dependent on the nucleation barrier, B, but also on nucleation kinetic factor, A. Each of the three nucleation parameters (namely the average nucleation temperature, $\langle T_{\mathrm{f}} \rangle$; the nucleation kinetic factor, A; and the nucleation barrier, B) are random variables, and this equation will be utilized in the bivariate model to constrain their formal relationship.

An additional limitation of the classic singular model is that it does not capture the cooling rate dependence of the nucleation process, only prescribing a single characteristic nucleation temperature. In reality, the nucleation temperature is dependent on the cooling rate with faster cooling rates yielding lower nucleation temperatures. This limitation is overcome in the proposed hybrid model since the expression relating the extreme variables, $\langle T_{\mathrm{f}} \rangle$ and B, to the nucleation rate pre-exponential factor, A, in Equation (3.24) also contains the cooling rate.

The proposed hybrid scheme is a case of bivariate analysis. The nucleation temperature and nucleation barrier, described by their separate univariate extreme value distributions, are not independent variables however, and we must consider their statistical dependence, which is determined by their empirical correlation. We can then construct a joint probability distribution that encodes the marginal distributions and correlation. Formulation of bivariate extreme value distributions with arbitrary marginal distributions is in general difficult due to the construction of the dependence structure and the absence of a finite parametric family, which exists for univariate extreme value distributions. The two most common bivariate models are the mixed and logistic models. Here, we implement the logistic model[197]–[199]:

$$G(x, y) = \exp\left\{-([-\ln(F_1(x))]^m + [-\ln(F_2(y))]^m)^{\frac{1}{m}}\right\} \tag{3.25}$$

where $G(x, y)$ is the bivariate extreme value distribution describing both random extreme variables, x and y, and $F_1(x)$ and $F_2(y)$ are the univariate marginal extreme value distributions. The quantity m is a measure of the dependence between the random variables and is defined as

$$m = \frac{1}{\sqrt{1-\rho}} \tag{3.26}$$

where ρ is the correlation coefficient. A value of m = 1 corresponds to independence of the two variables and leads to the joint distribution $G(x,y) = F_1(x)F_2(y)$. The joint probability density function follows similarly from the univariate definition and is given by

$$g(x,y) = \frac{\partial^2 G}{\partial x \partial y} \tag{3.27}$$

The bivariate extreme value distribution describes the variability and correlation of the two extreme variables: the nucleation temperature, $\langle T_f \rangle$, and nucleation barrier, B. This can then be used in conjunction with Equation (3.24) to solve for the distribution of the nucleation kinetic factor, A.

Determining the relevant extreme value distribution

Now that we have identified the extreme parameters and determined the form of the bivariate distribution, the next task is to identify the type of GEV distribution that describes each of the marginal distributions. Although the asymptotic theory predicts that the process will converge to one of the three types of GEV distributions shown in Table 3.2, we cannot immediately determine which one this is without information about the underlying process or distribution. If the underlying distribution of active sites is known, then the distribution of maximums is also known, and an extreme value analysis is moot. In the worst-case scenario, we cannot make any physical suppositions and are therefore left to fit data directly to the full three-parameter GEV distribution. By considering some properties of the GEV sub-classes however, we may be able to rule out some cases. For instance, we can consider the tail behavior of the distributions.

Both the nucleation temperature and the nucleation barrier are physically bounded. The nucleation temperature cannot be higher than the equilibrium melting point and cannot be lower than the homogeneous limit (roughly –40°C). In bulk systems that are not purified extensively, heterogeneous nucleation usually results in freezing occurring closer to the equilibrium melting point, making the Weibull distribution potentially a natural fit. Similarly, the nucleation barrier must be less than the homogeneous limit but must also be greater than zero. Since the nucleation barrier often varies many orders of magnitude in value, it is convenient to consider the logarithm of the value (i.e., $\ln B$). The logarithm of the nucleation barrier does not inherently have a lower bound (since extreme value analysis deals with maximums, we must consider $-\ln B$ which conversely does not have an inherent upper bound). We can most likely rule out the Weibull distribution, leaving the Fréchet distribution as a plausible choice for the log-distributed nucleation barrier. In this case, the homogeneous nucleation barrier would provide a physically sensible lower limit.

Often the best option for assessing which probability distribution best describes the distribution is using the graphical method of the probability plot[170], [199]. A good fit is indicated by the formation of a straight line when plotting the quantiles of the empirical distribution against the quantiles of a reference distribution. The probability plots in Figure 3.6 are linear in nature, indicating a decent goodness of fit has been obtained for the measured nucleation parameters.

Since there is uncertainty in the underlying active site distribution and little data in the literature on extreme value distributions for either nucleation temperatures or nucleation rate parameters, it is still recommended that each extreme value distribution be explored when studying a new system.

3.2.6 Results from constant cooling rate experiments

The survival curves of the nucleation temperatures are shown in Figure 3.5 for a series of 23 constant cooling rate experiments performed in the 5ml system with PBS at 2°C/min. While the spread of nucleation temperatures for individual trials is typically within 1°C (average standard deviation of 0.33°C), nucleation temperatures across the set of experiments ranges nearly 7°C (standard deviation of average nucleation of 1.55°C). This is consistent with nucleation experiments in the literature that find narrow spreads for individual systems and large spreads for experiments conducted on multiple systems[200], [201]. The stochastic behavior for individual nucleating catalysts is thus quite narrow, yet the characteristic temperature around which this purely stochastic behavior is centered can vary multiple degrees from system to system: a hallmark of non-self-averaging behavior, which indicates the potential suitability of extreme value theory.

The method of maximum likelihood estimation is used to determine the cumulative distribution function from Equation (3.14) and obtain the respective nucleation parameters for each of the survival curves. As a check of whether the observed nucleation process is well described by the proposed empirical nucleation rate $J(T) = A\exp(-B/T^3\Delta T^2)$, we can linearize the constant cooling rate CDF (see Deubener and Schmelzer[202]). The linearized nucleation spectra are shown in Figure 3.4b, and their linear form suggests the observed nucleation process is generally well described by the proposed nucleation rate.

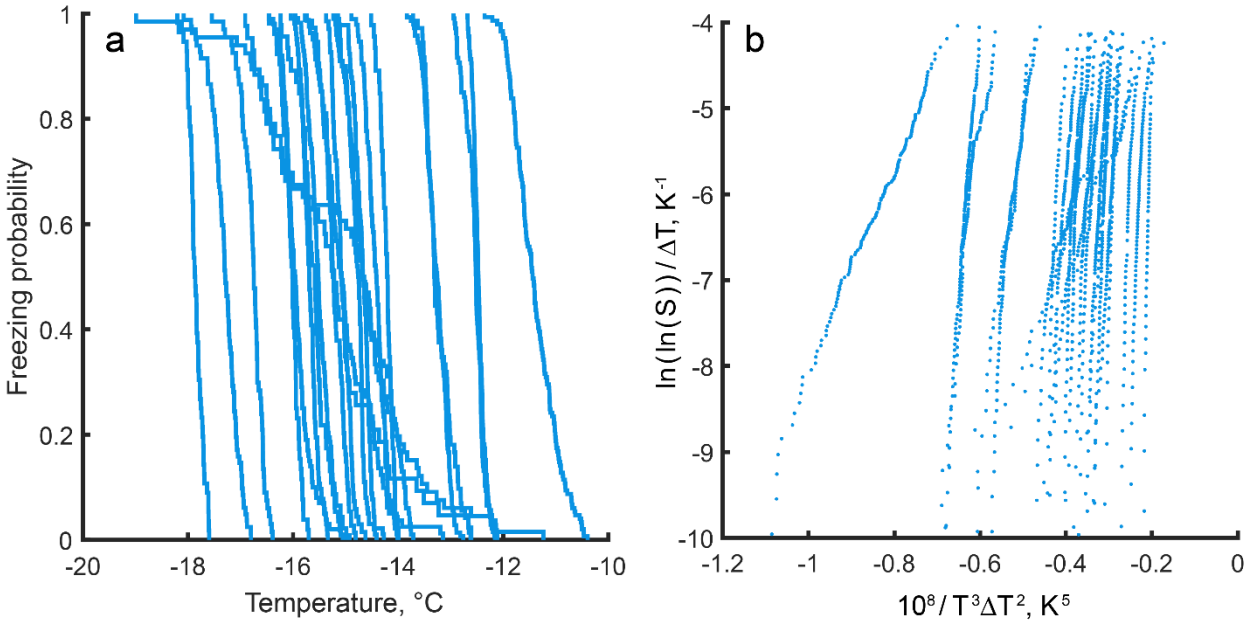

Figure 3.5: Constant cooling rate nucleation temperature data. a) Empirical cumulative distribution functions for a series of 23 constant cooling rate experiments performed in the 5ml

system with PBS at 2°C/min. b) Survival curves from panel a) linearized with respect to the cumulative distribution for the constant cooling rate experiment described by the nonhomogeneous Poisson process in Equation (3.14).

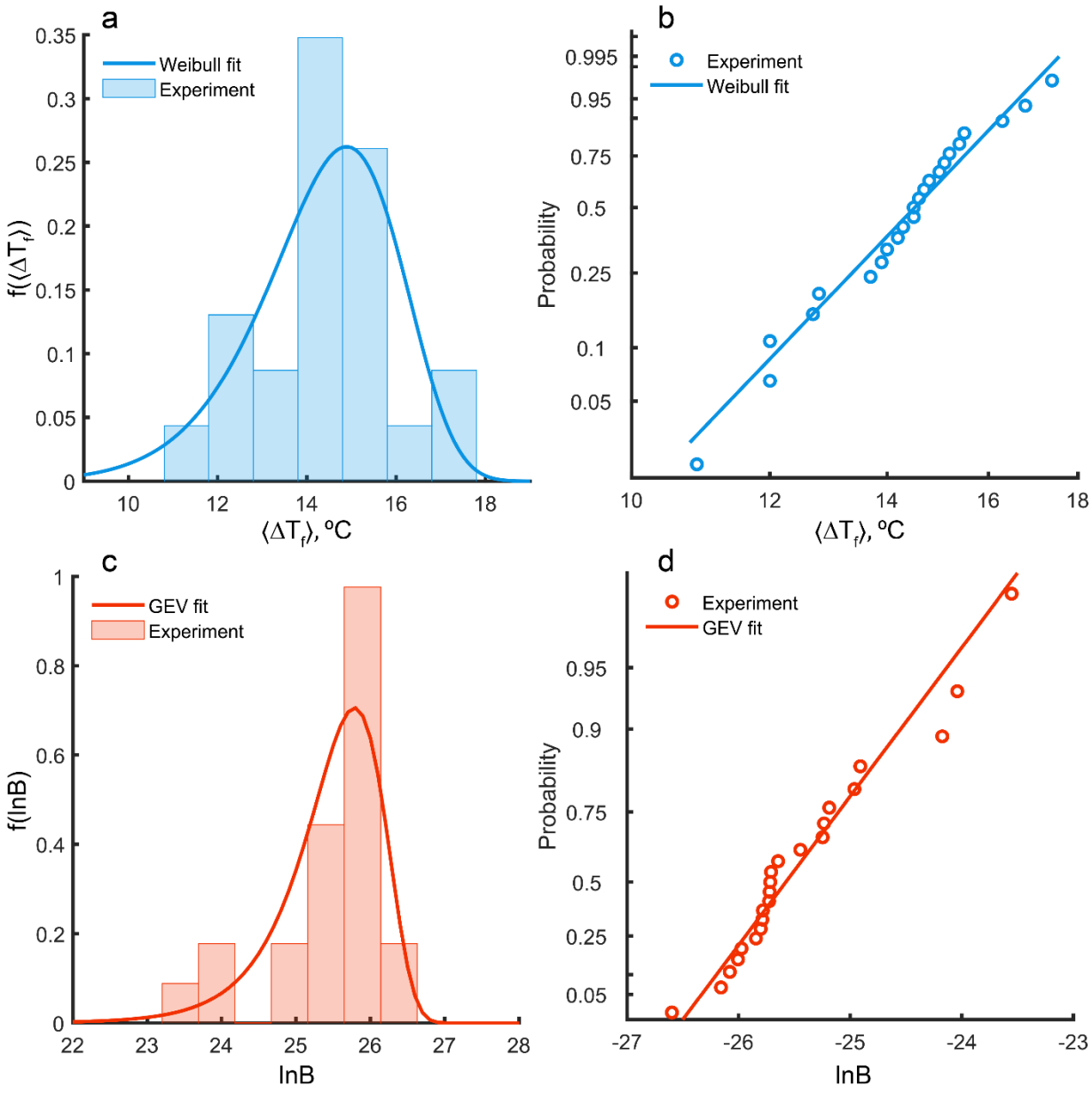

Figure 3.6: Extreme value distributions of mean nucleation temperature and nucleation barrier. a) Histogram and Weibull PDF of average nucleation temperatures from 5ml constant cooling rate experiments (n=23). b) Weibull probability plot of average nucleation temperatures. c) Histogram and GEV PDF for nucleation barrier from same experiments. d) Fréchet probability plot of nucleation barrier parameter.

3.2.7 Distribution of extreme parameters

With the empirical survival curves and inferred nucleation parameters in hand, we can now evaluate the distributions of the extreme variables: average nucleation temperature, $\langle \Delta T_\mathrm{f} \rangle$, and nucleation barrier, $\ln B$. Maximum likelihood estimation is used again for fitting of the extreme value distributions and the resulting distributions are shown in Figure 3.6 for the 5ml constant cooling rate experiments.

As discussed in Section 3.2.5, the Weibull distribution is a physically plausible choice for describing the distribution of nucleation temperatures between samples because of the melting temperature upper bound. A slight modification is first made to the Weibull distribution as defined in Equation (3.23). By considering the degree of supercooling upon freezing, $\Delta T_\mathrm{f} = T_\mathrm{m} - T_\mathrm{f}$, instead of the absolute nucleation temeprature, the location of the upper bound is shifted from T_m to zero. This effectively reduces the number of parameters in the Weibull distribution from three to two. Figure 3.6a depicts a histogram of the average nucleation temperatures along with the probability density function of the Weibull fit, and Figure 3.6b shows the Weibull probability plot of the average nucleation temperatures. Linearity in the probability plot indicates the $\langle \Delta T_\mathrm{f} \rangle$ data are well described by the Weibull distribution. We find an average degree of supercooling upon freezing of $\langle \Delta T_\mathrm{f} \rangle = 14.3°\mathrm{C}$ and standard deviation of $\sigma_{\langle \Delta T_\mathrm{f} \rangle} = 1.6°\mathrm{C}$.

In the case of the nucleation barrier, the full three parameter GEV distribution is fit to the nucleation barrier data and a best fit is found with the Fréchet distribution. This agrees with the intuition discussed in Section 3.2.5 that the homogeneous nucleation barrier represents a natural limit. Wood and Walton[87] found a value of $B_\mathrm{hom} = 1.66 \times 10^{12}\mathrm{K}^5$ ($\ln B_\mathrm{hom} = 28.14$), and though this limit has not been strictly enforced when fitting the Fréchet distribution here, the probability density function evaluated at the homogeneous limit is on the order of 10^{-60} and is small enough to exclude any nonphysical contributions. Figure 3.6c depicts a histogram of the nucleation barriers along with the probability density function of the fitted Fréchet distribution. Figure 3.6d shows the Frechet probability plot and the observed linearity suggests an appropriate fit. We find an average nucleation barrier of $\langle \ln B \rangle = 25.4$ and standard deviation of $\sigma_{\ln B} = 0.7$.

Having determined the marginal distributions, we can now consider the joint distribution. To that end, we first compute the correlation parameter for the two extreme variables using Equation (3.26) and find a value of $m = 1.32$. The joint probability density function, $g(\langle \Delta T_\mathrm{f} \rangle, \ln B)$, is then calculated from Equations (3.25) and (3.27) and is shown in Figure 3.7a. Next, we can perform a variable substitution in order to obtain the PDF in terms of the nucleation rate parameters, A and B, using the definition of the mean nucleation temperature form Equation (3.24). From the result, shown in Figure 3.7b, we see that the there is a narrow band of probable pairings, which indicates that nucleation parameters have a somewhat high degree of correlation and perhaps represents a fundamental property of heterogeneous nucleation.

In the context of classical nucleation theory (and shown in Equation (3.13)), the heterogeneous nucleation barrier, ΔG^*_het, is the product of the homogeneous nucleation barrier, ΔG^*_hom, and a heterogeneous shape factor, f, which accounts for a modified contact area between the growing solid ice cluster and the catalyst particle onto which it nucleates[203]:

$$\Delta G^*_{\text{het}} = \Delta G^*_{\text{hom}} f_{\text{het}}(\theta) \tag{3.28}$$

The shape factor, f_{het}, is a function of the contact angle, θ, between the ice embryo and nucleating surface and can vary between $f(0°) = 0$ (corresponding to complete wetting and no nucleation barrier) and $f(180°) = 1$ (corresponding to complete hydrophobicity and homogeneous nucleation). Hydrophilic surfaces, which have small contact angles and also smaller nucleation barriers, are often polar in nature, and polar surfaces are known to orient liquid water molecules in their close vicinity. Therefore, a potential explanation for the scaling behavior seen in Figure 3.8c and correlation seen in Figure 3.7b could be that the reduction in mobility of liquid molecules caused by more potent hydrophilic nucleating surfaces results in a smaller pre-exponential diffusive coefficient.

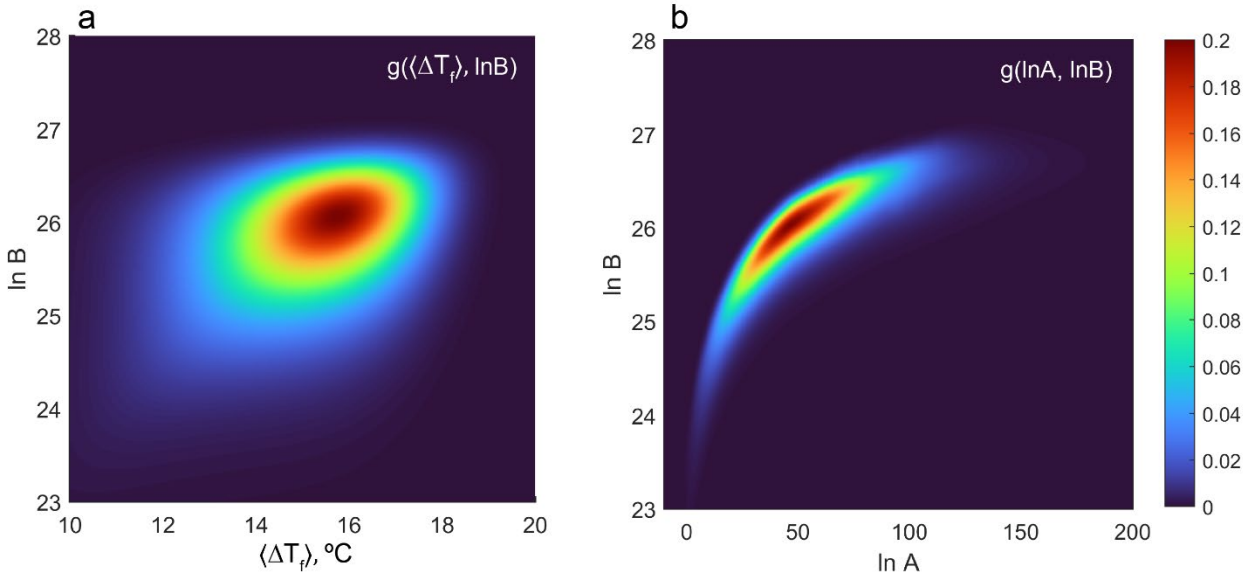

Figure 3.7: Bivariate extreme value distributions. a) Joint probability density function, $g(\langle \Delta T_{\text{f}} \rangle, \ln B)$ computed from the marginal univariate extreme value distributions for the mean freezing temperature, $\langle \Delta T_{\text{f}} \rangle$, and nucleation barrier, B. The distribution is centered at $\langle \Delta T_{\text{f}} \rangle = 14.3°\text{C}$ and $\ln B = 25.4$. b) Probability density function from panel a) with the mean freezing temperature transformed to $\ln A$ using the definition of the mean nucleation temperature for a constant cooling rate experiment from Equation (3.23). A narrow distribution indicates a strong correlation between the kinetic and thermodynamic nucleation parameters.

Now that we have determined the distribution of the nucleation parameters from extreme value statistics, we can apply this model to useful ends. Since the 5ml systems are not a practical size for preserving anything beyond cell suspensions and small tissue constructs, we may be interested in seeing how the model can be used to predict nucleation behavior in larger, more relevant volumes. This will be covered in the following section. Additionally, the experiments from

which the model is constructed, constant cooling rate experiments, do not represent the modality of supercooling employed when actually preserving a biological specimen. In reality, preservation is conducted at a constant temperature and at temperatures warmer than the supercooling limits probed in constant cooling rate experiments. We may therefore be interested in evaluating how the model predicts nucleation behavior in isothermal systems and as a function of time. This will be covered in Section 3.2.9.

3.2.8 Scaling of the nucleation process with system size

A useful property of probability distributions is that the probability of independent events occurring together is the product of the independent probabilities (i.e., $P(A \text{ and } B) = P(A) \cdot P(B)$). If we consider a large system being comprised of a collection of smaller independent systems, we can generalize this rule to predict how probability distributions scale with system size. For example, if $F(x)$ is the cumulative distribution function for a system of size n_1, then the distribution for an identical system of size n_2 is $[F_1(x)]^{n_2/n_1}$. Following this logic, the size of the system can be readily incorporated into the GEV distribution yielding:

$$G(x,V) = [G(x)]^{V/V_0} = \exp\left\{-\frac{V}{V_0}\left[1+\xi\left(\frac{x-\mu}{\sigma}\right)\right]^{-1/\xi}\right\} \tag{3.29}$$

where V_0 is the volume of the system from which the model was developed, and V is the volume of an arbitrary system. If a process were to scale with surface area rather than volume, then the relevant surface area quantity could be used instead. In systems where heterogeneous catalysts are intentionally added in order to study their nucleation behavior or to initiate nucleation, the relative scaling parameter would be the total nucleant surface area which is then often converted to a concentration.

Incorporating the system size into the probability functions in this manner can help assess the validity of the statistical model developed thus far. For example, we can conduct a campaign of constant cooling rate experiments in a larger system and assess the level of agreement with the volume scaling predictions from the statistical model based on the 5ml data.

The 5ml and 20ml systems employed in this study have a volume ratio of $V_{20}{:}\,V_5 = 4$ and a surface area ratio of $S_{20}{:}\,S_5 = 2.2$. Although we can hypothesize that the petrolatum coating removes the possibility of ice nucleation on the container surface since it is a slippery hydrocarbon-based material similar to oils used to study homogeneous nucleation in emulsions, we cannot decisively conclude whether nucleation is initiated on the container surface during the constant cooling rate experiments and thus expect nucleation behavior to scale with surface area, or whether nucleation is initiated in the bulk of the fluid and thus expect nucleation to scale with volume.

An additional factor that must be considered is the temperature gradient that persists within the cylindrical volumes while being cooled at a constant rate. The 5ml chamber has an inner radius of 6.35mm and the 20ml chamber has an inner radius of 12.7mm. From a simple scaling analysis, we can approximate the temperature difference from the wall to the center axis of the cylindrical chamber, as well as the radial thermal penetration depth within which the temperature is

approximately uniform. The radial thermal penetration depth for a constant wall temperature is given by $\delta_r = \sqrt{4\alpha t}$ and during constant cooling becomes:

$$\delta_r = \sqrt{\frac{4\alpha\Delta T}{C}} \tag{3.30}$$

where α is the thermal diffusivity (~0.12 mm^2/s for supercooled water), ΔT is the temperature difference (°C), and C is the cooling rate (°C/s). For the 5ml system and a cooling rate of 2°C/min, we find that the center axis lags the wall temperature by ~2.6°C. For the 20ml system and a cooling rate of 1°C/min, the center lags the wall temperature by ~5.2°C. In the case of volume nucleation, if we assume that nucleation is occurring in the coldest part of the system, the entire volume likely would not contribute to nucleation but rather a portion of the volume within a certain distance from the inner wall.

Due to the radial temperature gradient within the chambers, there is a potential for buoyancy-driven natural convection to develop, which would increase heat transfer within the chamber and reduce the temperature gradient approximated by Equation (3.10). A smaller temperature gradient would ultimately lead to an effective scaling between the limiting scenarios of surface or volume scaling depicted in Figure 3.8. Interestingly, one of water's many anomalous properties is the density maximum that occurs around 4°C. At this temperature the coefficient of thermal expansion is zero and there is no driving force for natural convection. Ultimately, this effect warrants further investigation and future studies should consider incorporating convective transport effects with the aim of developing more accurate scaling predictions.

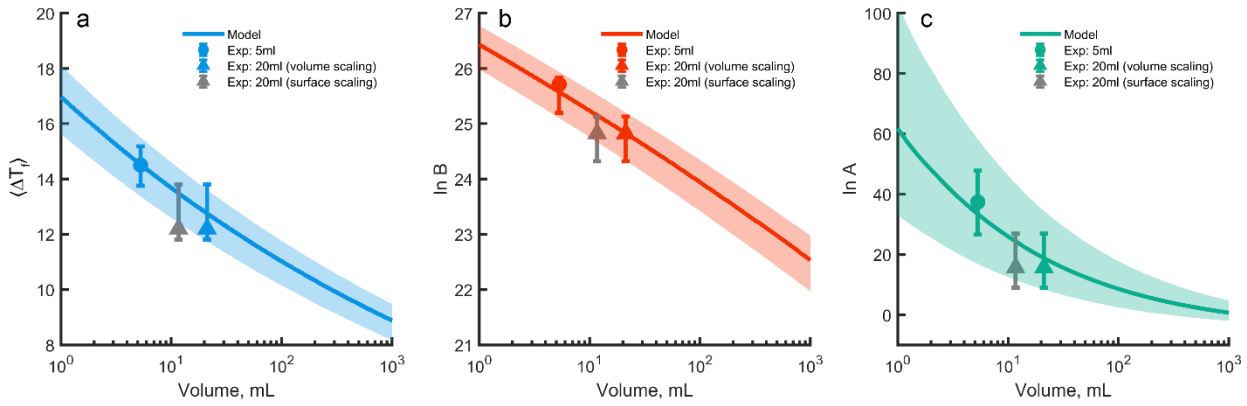

Figure 3.8: Scaling of the nucleation parameters with system volume. Scaling of a) nucleation temperature, $\langle \Delta T_f \rangle$, b) nucleation barrier, $\ln B$, and c) nucleation kinetic factor, $\ln A$, computed from the individual extreme value model based on 5ml data. Scaling of the extreme variables, $\langle \Delta T_f \rangle$ and B, is evaluated following the relation in Equation (3.29). Scaling of the kinetic factor, A, is subsequently computed using the relation in Equation (3.24). Data points are from constant cooling rate experiments in 5ml (●) and 20ml (▲) systems as described in Section 3.2.3. Two points are shown for the 20ml data, corresponding to pure volume scaling (same color as 5ml data),

and surface area scaling (gray). The solid curves correspond to the median value, while error bars and shaded regions denote 25%/75% quartiles.

Shown in Figure 3.8 are the three nucleation parameters $\langle \Delta T_f \rangle$, $\ln B$, and $\ln A$ computed as a function of volume, V. The solid lines represent the median value of each parameter, and the shaded regions are bounded by the 25% and 75% quartiles. The dependence on volume is predicted following the relation in Equation (3.29) which incorporates volume into the GEV distribution. The nucleation temperatures are computed by incorporating volume into the Weibull distribution. Similarly, scaling of the nucleation barrier, $\ln B$, is computed by incorporating volume into the Fréchet distribution. The nucleation pre-exponential factor, $\ln A$, is obtained using Equation (3.24).

The average nucleation temperature (Figure 3.8a) scales relatively linearly with the logarithm of the volume, levelling off at larger volumes. The decreasing trend of the nucleation temperature with volume is caused by an increased likelihood for more potent nucleating catalysts in larger samples. Whereas in very small systems (such as micro-emulsions whose droplet diameters are often on the order of single microns) it may be possible to exclude all or most insoluble impurities (other than the encapsulating oil phase), larger systems inherently will contain more impurities. This result is consistent with the early findings of Bigg[204], [205], Langham and Mason[173], and Mossop[206] and is in accordance with the singular model for the nucleation. The linearity is expected to be a universal property for nucleation of systems containing the same population of nucleating catalysts. The precise slope and position of this curve, however, is dependent on the particular source of water and the population of impurities that it contains. The scaling of the nucleation barrier, $\ln B$, behaves similarly to the scaling of nucleation temperature, i.e., the larger the system is, the higher the likelihood of more potent nucleating agents, and thus larger systems possess smaller characteristic nucleation barriers.

One result that would be difficult to predict without this analysis is how the nucleation pre-exponential factor, A, scales with volume. This factor is often assumed to be the same for heterogeneous nucleation and homogeneous nucleation since in the context of CNT it is related to the diffusion of liquid molecules to the surface of the growing solid nucleus, and thus thought to be solely a property of the liquid and not of the nucleating catalyst. As discussed in Section 3.2.5, for consistency of the bivariate statistical model, this parameter cannot remain constant and is actually constrained by the values of the other two parameters, $\langle \Delta T_f \rangle$ and B. Interestingly, the value of A is predicted to decrease with increasing volume (Figure 3.8c), which is perhaps counterintuitive since a smaller A yields a lower nucleation rate for a constant value of B. This behavior is in fact consistent with many studies of heterogeneous nucleation, and, as discussed in Section 3.2.7, could be a result of reduced molecular mobility in the vicinity of potent active sites that are somewhat polar and hydrophilic. Regarding the width of the distribution, it is quite wide at small volumes and becomes quite narrow for larger volumes. It is difficult to ascribe a physical justification for this behavior since in the scope of this extreme value analysis, the parameter A is not an extreme variable, and as such, we can neither predict its distribution for the most potent active site nor can we comment on the value of A for the remainder of the active sites. Future studies should seek to validate this result and investigate potential physical origins.

Also shown in Figure 3.8 are the median parameters from experiments performed in the 5ml and 20ml systems. The 20ml data is displayed in two instances, corresponding to scaling with volume and surface area. The same general trend (increasing vs. decreasing) is seen between the experiments and model prediction which supports the underlying premises of the model. The volume scaling produces the best agreement, suggesting that nucleation is not necessarily occurring on the container's inner surface. Future experimental studies should investigate this scaling behavior further.

3.2.9 Freezing probability versus time in systems at constant temperature

Having developed a statistical model that describes the random distribution of the kinetic and thermodynamic nucleation parameters and describes how they vary with system size, we can now address the practical objective of this research: determining the freezing probability of supercooled aqueous systems in order to identify conditions under which biological material may be held in a stable supercooled liquid state. The isothermal freezing probability, resulting from the homogeneous Poisson distribution of Equation (3.9) and the nucleation rate from Equation (3.13), is given by

$$P(T,t|A,B) = 1 - \exp\left[-A\exp\left(\frac{-B}{T^3\Delta T^2}\right)t\right] \tag{3.31}$$

For systems with uncharacterized impurities, the nucleation parameters in this expression, A and B, are random variables. The model developed in this study has treated the mean nucleation temperature and the nucleation barrier parameters as extreme variables, which enables the heterogeneous nucleation process to be described by the joint extreme value distribution in Equation (3.25). To incorporate the dependence on system volume, Equation (3.25) can be modified in accordance with Equation (3.29). By further transforming $\langle \Delta T_f \rangle$ to A using the definition of the mean nucleation temperature from Equation (3.24), we can obtain an expression for the probability density function in terms of A and B: $g(\langle T_f \rangle, B) \rightarrow g(A,B)$. Finally, we can obtain a generalized expression for the isothermal freezing probability as a function of volume and time by integrating over all possible values of A and B weighted by their joint probability density.

$$P(T,V,t) = \iint_{A,B} P(T,t|A,B)g(A,B|V)dAdB \tag{3.32}$$

This relation is used to compute the freezing probability, shown in Figure 3.9a, for physiological saline in a 5ml system with petrolatum-coated surfaces. We find that the logarithm of the probability scales approximately linearly with temperature for small probabilities ($p < 0.5$). The trend of freezing behavior with supercooled duration is also interesting. For a given freezing probability, varying the temperature by only a few degrees results in the corresponding induction time varying from one day to one year. This result may have the practical implication of

extrapolating supercooled states observed to be stable on the order of days to being stable for much longer periods of time.

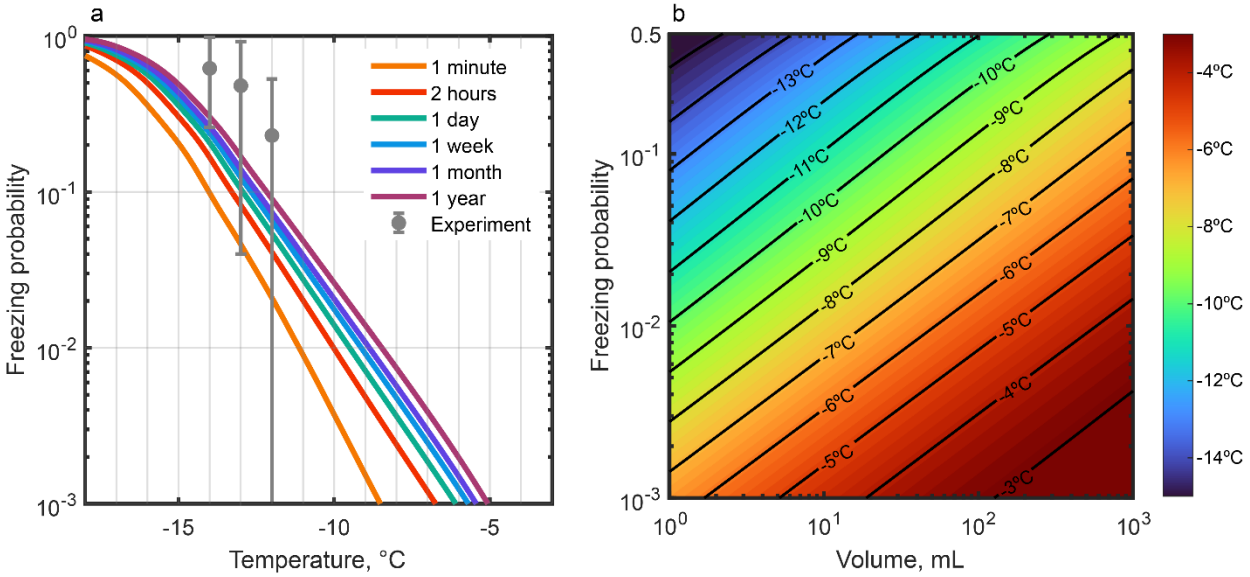

Figure 3.9: Isothermal freezing probabilities. a) Freezing probability for a rigidly confined 5ml system with physiological saline and petrolatum-coated surfaces as a function of temperature and for various durations, computed from Equation (3.32). Data points correspond to average freezing probabilities from the campaign of isothermal nucleation experiments with a cut-off time of two hours. Error bars correspond to +/- one standard deviation. b) Probability of freezing within a time of 24 hours as a function of system volume and temperature, computed from Equation (3.32).

The results of the 5ml isothermal experiments are also shown in Figure 3.9a. In each of these experiments, the effective quantity measured is the probability of the sample freezing within two hours of being supercooled. Average freezing probabilities of 23% (n=10), 48% (n=6), and 62% (n=18) are found for temperatures of –12°C, –13°C, and –14°C, respectively. As anticipated, the freezing probability increases with decreasing temperature, however the experimental values are consistently higher than those predicted by the model.

Considerable variation is observed for the isothermal trials (repeated experiments at individual temperatures yielded standard deviations of roughly +/–30%). Though this, as well as the relatively small number of repeated trials, likely contribute to the disagreement with predictions, this general observation is in fact in accordance with predictions of the statistical model. Due to relatively large variation in active site potency between experiments, a high likelihood is predicted of either observing almost no freezing events within 2 hours or observing a freezing rate of nearly 100%. This highlights the difficulty of performing isothermal nucleation rate experiments as compared to constant cooling rate experiments as well as the difficulty of interpreting results from individual nucleation experiments.

Figure 3.8b depicts the freezing probability as a function of temperature and volume for a supercooling duration of 24 hours. This heat map can be of immediate use to the applied cryobiologist by informing the choice of preservation temperature based on the size of their system and appropriate freezing risk level. For example, accepting a 1% probability compared to a 0.1% chance of freezing would enable the storage temperature to be reduced by roughly 3-4°C. Accepting a 10% chance of freezing could enable the storage temperature to be reduced an additional 3-4°C.

3.2.10 Conclusion

Supercooling, which describes the phenomenon of water remaining in a metastable liquid state below its equilibrium melting temperature, is an attractive premise for preserving biological material at low temperature yet in the absence of ice. Being a metastable process however, there is a nonzero probability at all times for freezing to occur, and this reality represents a significant challenge for the clinical translatability of any supercooling technique. Just as reactor engineers designing nuclear power plants need to know the probability of a meltdown occurring and civil engineers designing a suspension bridge need to know the likelihood of a high-magnitude earthquake, transplantation surgeons need certain assurance that their supercooled organ will not freeze during the storage period. Without methods to arrest ice growth before damage is imparted, quantifying freezing probability is expected to be central to enabling the widespread implementation of supercooling.

Ultimately, heterogeneous nucleation is a complex problem that is both incompletely understood from a molecular level and difficult to characterize from an experimental standpoint. Random active sites, existing as minute insoluble particles floating in solution or adhered to container walls as well as certain water-soluble macromolecules, can remain nearly undetectable in solution and produce seemingly unpredictable freezing behavior across repeated experiments. Predicting nucleation behavior in the presence of uncharacterized impurities remains an unsolved problem with broad implications.

In this study, we leverage the observation that nucleation often occurs repeatedly on the single most potent active site present in a system in order to approach the problem using the statistical theory of extreme values. This enables us to reduce the scope of the problem by circumventing the need to characterize every potential active site. We develop a joint singular and stochastic model based on data from constant cooling rate experiments in order to quantify the sample-to-sample variability and time-dependent intra-sample stochasticity. By capturing the variability of the kinetic and thermodynamic parameters governing heterogeneous nucleation, the model is able to predict the probability of nucleation as a function of temperature, volume, and time. Together, this approach constrains the multi-faceted probabilistic nature of heterogeneous ice nucleation and enables the rational design of supercooled biopreservation protocols.

Chapter 4

Conclusions and Outlook

Clinical methods for solid organ preservation have not changed dramatically over the past half century, still largely involving hypothermic static cold storage on ice. This only permits brief periods of viability during *ex vivo* handling and has contributed substantially to the logistical constraints in transplantation and exacerbated the ongoing organ shortage. A recent resurgence in funding and attention surrounding innovation in transplantation medicine, however, has led to renewed development of advanced preservation techniques such as supercooling.

Supercooling enables preservation at sub-zero temperatures in the absence of ice and may enable significant extension to the preservation durations afforded by static cold storage. This follows from the Arrhenius temperature dependence of metabolism, commonly cited as reducing by 50% for every 10°C [18]. Due to inherent molecular stochasticity and random heterogeneous catalysis, however, the nucleation of ice in supercooled water is random and difficult to reliably predict.

This thesis has identified methods to enhance supercooling stability and developed statistical models to constrain freezing probability. Isochoric (rigid) confinement has been found to protect against external mechanical disturbance. Increased supercooling stability is also found with the application of hydrophobic surface coatings along with the addition of chemical solutes such as traditional cryoprotectant agents and as well as macromolecules. Poisson statistics are employed to describe the inherent stochasticity of nucleation, and hybrid extreme value statistical models are developed to capture the random variability of heterogeneous catalysis by uncharacterized impurities. Notably, these models enable the development of stability maps that enable prediction of freezing probability as a function of supercooled duration, temperature, volume, and solution composition.

These findings also motivate future investigations. For example, preliminary observations about the effect of solutes and viscosity on the nucleation behavior were made, however these effects have not been incorporated into a general model for the nucleation rate. Future efforts could attempt to extend the extreme value statistics model developed in Section 3.2 to describe solutions of arbitrary concentration and viscosity. This may well seem like a lofty goal, however, recent studies have begun developing models of the nucleation rate as a function of the water activity of a solution, finding universal behavior irrespective of the exact nature of the solute [207]–[209].

Furthermore, the nucleation behavior of only two surfaces (bare aluminum and Vaseline) have been studied in this work. Identifying the optimal surface and determining how to incorporate it into a clinically suitable device could prove fruitful. Identifying more precisely whether nucleation scales with container surface area or volume would also strengthen our ability to reliably predict

supercooling stability. Similarly, experiments presented in this thesis have only studied the nucleation behavior aqueous solutions in the absence of tissue or other biological material. It is generally assumed that biological material are poor nucleating substrates (with the exception of certain bacteria, proteins and other macromolecules), a premise that should be explicitly validated.

Ultimately, due to the challenges of stably supercooling large aqueous systems, the effect of low temperature on organs and other biological systems is still largely unclear. This work establishes a framework for the design of robust and scalable supercooling protocols (from device and solution design to selection of a stable storage temperature), and future efforts should build on this foundation to study preservation at supercooled temperatures and identify paths towards clinical translation. While supercooling enables lower temperature preservation and better maintenance of cellular energy reserves (e.g. ATP), poorly understood chilling injury mechanisms may be exacerbated. Experiments should seek to understand these mechanisms and identify how to optimally modify standard preservation solutions. Lastly, with the continuous improvement of profusion techniques, wholistic methods should be developed to optimize the entire preservation protocol.

Bibliography

[1] S. Giwa *et al.*, "The promise of organ and tissue preservation to transform medicine," *Nature Biotechnology*, vol. 35, no. 6. pp. 530–542, 2017. doi: 10.1038/nbt.3889.

[2] G. M. Fahy, B. Wowk, and J. Wu, "Cryopreservation of Complex Systems: The Missing Link in the Regenerative Medicine Supply Chain," *Rejuvenation Res.*, vol. 9, no. 2, pp. 279–291, May 2006, doi: 10.1089/rej.2006.9.279.

[3] B. Rubinsky, "Principles of Low Temperature Cell Preservation," *Heart Fail. Rev.*, vol. 8, no. 3, pp. 277–284, 2003, doi: 10.1023/A:1024734003814.

[4] P. G. Debenedetti, *Metastable Liquids*. Princeton University Press, 2021. doi: doi:10.1515/9780691213941.

[5] L. Weng, S. N. Tessier, K. Smith, J. F. Edd, S. L. Stott, and M. Toner, "Bacterial Ice Nucleation in Monodisperse D2O and H2O-in-Oil Emulsions," *Langmuir*, vol. 32, no. 36, pp. 9229–9236, Sep. 2016, doi: 10.1021/acs.langmuir.6b02212.

[6] K. E. Zachariassen and E. Kristiansen, "Ice Nucleation and Antinucleation in Nature," *Cryobiology*, vol. 41, no. 4, pp. 257–279, 2000, doi: https://doi.org/10.1006/cryo.2000.2289.

[7] J. FARRANT, "Mechanism of Cell Damage During Freezing and Thawing and its Prevention," *Nature*, vol. 205, no. 4978, pp. 1284–1287, 1965, doi: 10.1038/2051284a0.

[8] S. N. Tessier *et al.*, "The role of antifreeze glycopeptides (AFGP) and polyvinyl alcohol/polyglycerol (X/Z-1000) cocktails as ice modulators during partial freezing of rat livers," *bioRxiv*, p. 2021.08.04.455092, Jan. 2021, doi: 10.1101/2021.08.04.455092.

[9] S. N. Tessier *et al.*, "Partial freezing of rat livers extends preservation time by 5-fold," *Nat. Commun.*, vol. 13, no. 1, p. 4008, 2022, doi: 10.1038/s41467-022-31490-2.

[10] G. M. Fahy, D. R. MacFarlane, C. A. Angell, and H. T. Meryman, "Vitrification as an approach to cryopreservation," *Cryobiology*, vol. 21, no. 4, pp. 407–426, Aug. 1984, doi: 10.1016/0011-2240(84)90079-8.

[11] P. M. Zavos and E. F. Graham, "Effects of various degrees of supercooling on motility and fertility of turkey spermatozoa," *Cryo-letters*, 1982.

[12] G. A. Kozlov and V. I. Teodorovich, "Kinetics of isothermal crystallization of supercooled blood drops," *Biofizika*, vol. 15, no. 4, pp. 657–664, 1970.

[13] S. F. Mathias, F. Franks, and R. H. M. Hatley, "Preservation of viable cells in the undercooled state," *Cryobiology*, vol. 22, no. 6, pp. 537–546, 1985, doi: https://doi.org/10.1016/0011-2240(85)90030-6.

BIBLIOGRAPHY

[14] P. M. Zavos and E. F. Graham, "Preservation of Turkey spermatozoa by the use of emulsions and supercooling methods," *Cryobiology*, vol. 18, no. 5, pp. 497–505, 1981, doi: https://doi.org/10.1016/0011-2240(81)90209-1.

[15] D. H. Rasmussen, M. N. Macaulay, and A. P. Mackenzie, "Supercooling and nucleation of ice in single cells," *Cryobiology*, vol. 12, no. 4, pp. 328–339, 1975, doi: https://doi.org/10.1016/0011-2240(75)90006-1.

[16] "36. Deep supercooling of Saccharomyces cerevisiae," *Cryobiology*, vol. 10, no. 6, p. 517, 1973, doi: https://doi.org/10.1016/S0011-2240(73)80040-9.

[17] T. A. Berendsen *et al.*, "Supercooling enables long-term transplantation survival following 4 days of liver preservation," *Nat. Med.*, vol. 20, no. 7, pp. 790–793, Jun. 2014.

[18] R. J. de Vries *et al.*, "Supercooling extends preservation time of human livers," *Nature Biotechnology*, vol. 37, no. 10. pp. 1131–1136, 2019. doi: 10.1038/s41587-019-0223-y.

[19] A. Consiglio, G. Ukpai, B. Rubinsky, and M. J. Powell-Palm, "Suppression of cavitation-induced nucleation in systems under isochoric confinement," *Phys. Rev. Res.*, vol. 2, no. 2, 2020, doi: 10.1103/physrevresearch.2.023350.

[20] A. N. Consiglio, D. Lilley, R. Prasher, B. Rubinsky, and M. J. Powell-Palm, "Methods to stabilize aqueous supercooling identified by use of an isochoric nucleation detection (INDe) device," *Cryobiology*, 2022, doi: https://doi.org/10.1016/j.cryobiol.2022.03.003.

[21] B. M. Guerreiro, A. N. Consiglio, B. Rubinsky, M. J. Powell-Palm, and F. Freitas, "Enhanced Control over Ice Nucleation Stochasticity Using a Carbohydrate Polymer Cryoprotectant," *ACS Biomater. Sci. Eng.*, Apr. 2022, doi: 10.1021/acsbiomaterials.2c00075.

[22] A. N. Consiglio, B. Rubinsky, and M. J. Powell-Palm, "Relating Metabolism Suppression and Nucleation Probability During Supercooled Biopreservation," *J. Biomech. Eng.*, Mar. 2022, doi: 10.1115/1.4054217.

[23] A. N. Consiglio, Y. Ouyang, M. J. Powell-Palm, and B. Rubinsky, "An extreme value statistics model of heterogeneous ice nucleation for quantifying the stability of supercooled aqueous systems," *J. Chem. Phys.*, vol. 159, no. 5, 2023.

[24] E. J. Lavernia and T. S. Srivatsan, "The rapid solidification processing of materials: Science, principles, technology, advances, and applications," *Journal of Materials Science*, vol. 45, no. 2. Springer, pp. 287–325, Jan. 01, 2010. doi: 10.1007/s10853-009-3995-5.

[25] G. G. Stonehouse and J. A. Evans, "The use of supercooling for fresh foods: A review," *Journal of Food Engineering*. 2015. doi: 10.1016/j.jfoodeng.2014.08.007.

[26] R. J. de Vries *et al.*, "Supercooling extends preservation time of human livers," *Nature Biotechnology*. 2019. doi: 10.1038/s41587-019-0223-y.

[27] T. A. Berendsen *et al.*, "Supercooling enables long-term transplantation survival following 4 days of liver preservation," *Nat. Med.*, 2014, doi: 10.1038/nm.3588.

[28] H. Huang, M. L. Yarmush, and O. B. Usta, "Long-term deep-supercooling of large-volume

water and red cell suspensions via surface sealing with immiscible liquids," *Nat. Commun.*, 2018, doi: 10.1038/s41467-018-05636-0.

[29] B. J. Fuller, A. Petrenko, and E. Guibert, "Human organs come out of the deep cold," *Nat. Biotechnol.*, 2019, doi: 10.1038/s41587-019-0264-2.

[30] R. Hickling, "Nucleation of freezing by cavity collapse and its relation to cavitation damage," *Nature*, 1965, doi: 10.1038/206915a0.

[31] R. Hickling, "Transient, high-pressure solidification associated with cavitation in water," *Phys. Rev. Lett.*, vol. 73, no. 21, pp. 2853–2856, 1994, doi: 10.1103/PhysRevLett.73.2853.

[32] M. D. Luque de Castro and F. Priego-Capote, "Ultrasound-assisted crystallization (sonocrystallization)," *Ultrason. Sonochem.*, 2007, doi: 10.1016/j.ultsonch.2006.12.004.

[33] S. W. Young and W. J. Van Sicklen, "The mechanical stimulus to crystallization," *J. Am. Chem. Soc.*, 1913, doi: 10.1021/ja02198a002.

[34] P. C. Myint and J. L. Belof, "Rapid freezing of water under dynamic compression," *J. Phys. Condens. Matter*, vol. 30, no. 23, p. 233002, Jun. 2018, doi: 10.1088/1361-648X/aac14f.

[35] P. C. Myint *et al.*, "Nanosecond Freezing of Water at High Pressures: Nucleation and Growth near the Metastability Limit," *Phys. Rev. Lett.*, vol. 121, no. 15, p. 155701, Oct. 2018, doi: 10.1103/PhysRevLett.121.155701.

[36] M. J. Powell-Palm, A. Koh-Bell, and B. Rubinsky, "Isochoric conditions enhance stability of metastable supercooled water," *Appl. Phys. Lett.*, 2020.

[37] F. R. Gilmore, "The growth or collapse of a spherical bubble in a viscous compressible liquid," California Institute of Technology, Apr. 1952.

[38] "Revised Release on the IAPWS Formulation 1995 for the Thermodynamic Properties of Ordinary Water Substance for General and Scientific Use," Prague, Czech Republic, 2018.

[39] "Revised Release on the Pressure along the Melting and Sublimation Curves of Ordinary Water Substance," Plzeň, Czech Republic, 2011.

[40] G. W. Lee, W. J. Evans, and C.-S. Yoo, "Crystallization of water in a dynamic diamond-anvil cell: Evidence for ice VII-like local order in supercompressed water," *Phys. Rev. B*, vol. 74, no. 13, p. 134112, Oct. 2006, doi: 10.1103/PhysRevB.74.134112.

[41] A. E. Gleason *et al.*, "Compression Freezing Kinetics of Water to Ice VII," *Phys. Rev. Lett.*, vol. 119, no. 2, p. 025701, Jul. 2017, doi: 10.1103/PhysRevLett.119.025701.

[42] D. M. Sterbentz, P. C. Myint, J. P. Delplanque, and J. L. Belof, "Numerical modeling of solid-cluster evolution applied to the nanosecond solidification of water near the metastable limit," *J. Chem. Phys.*, vol. 151, no. 16, p. 164501, Oct. 2019, doi: 10.1063/1.5125948.

[43] P. C. Myint, L. X. Benedict, and J. L. Belof, "Free energy models for ice VII and liquid water derived from pressure, entropy, and heat capacity relations," *J. Chem. Phys.*, vol. 147, no. 8, p. 084505, Aug. 2017, doi: 10.1063/1.4989582.

[44] D. Kashchiev, "Solution of the non-steady state problem in nucleation kinetics," *Surf. Sci.*,

vol. 14, no. 1, pp. 209–220, Mar. 1969, doi: 10.1016/0039-6028(69)90055-7.

[45] K. Kerboua and O. Hamdaoui, "Void fraction, number density of acoustic cavitation bubbles, and acoustic frequency: A numerical investigation," *J. Acoust. Soc. Am.*, 2019, doi: 10.1121/1.5126865.

[46] M. J. Powell-Palm, B. Rubinsky, and W. Sun, "Freezing water at constant volume and under confinement," *Commun. Phys.*, vol. 3, no. 39, 2020, doi: https://doi.org/10.1038/s42005-020-0303-9.

[47] B. Rubinsky, P. A. Perez, and M. E. Carlson, "The thermodynamic principles of isochoric cryopreservation," *Cryobiology*, 2005, doi: 10.1016/j.cryobiol.2004.12.002.

[48] H. G. Flynn, "Cavitation dynamics. I. A mathematical formulation," *Cit. J. Acoust. Soc. Am.*, vol. 57, p. 1379, 1975, doi: 10.1121/1.380624.

[49] R. Hicking and M. S. Plesset, "Collapse and rebound of a spherical bubble in water," *Phys. Fluids*, vol. 7, no. 1, pp. 7–14, 1964, doi: 10.1063/1.1711058.

[50] H. R. Pruppacher and J. D. Klett, "Microstructure of Atmospheric Clouds and Precipitation," pp. 10–73, 2010, doi: 10.1007/978-0-306-48100-0_2.

[51] D. M. Murphy and T. Koop, "Review of the vapour pressures of ice and supercooled water for atmospheric applications," *Q. J. R. Meteorol. Soc.*, vol. 131, no. 608, pp. 1539–1565, Apr. 2005, doi: 10.1256/QJ.04.94.

[52] R. W. SALT, "Role of Glycerol in producing Abnormally Low Supercooling and Freezing Points in an Insect, Bracon cephi (Gahan)," *Nat. 1958 1814618*, vol. 181, no. 4618, pp. 1281–1281, 1958, doi: 10.1038/1811281a0.

[53] A. L. DeVries and D. E. Wohlschlag, "Freezing Resistance in Some Antarctic Fishes," *Science (80-.).*, vol. 163, no. 3871, pp. 1073–1075, Mar. 1969, doi: 10.1126/SCIENCE.163.3871.1073.

[54] H. Huang, C. Rey-Bedón, M. L. Yarmush, and O. B. Usta, "Deep-supercooling for extended preservation of adipose-derived stem cells," *Cryobiology*, vol. 92, pp. 67–75, Feb. 2020, doi: 10.1016/J.CRYOBIOL.2019.11.004.

[55] M. J. Powell-Palm, V. Charwat, B. Charrez, B. Siemons, K. E. Healy, and B. Rubinsky, "Isochoric supercooled preservation and revival of human cardiac microtissues," *bioRxiv*, p. 2021.03.22.436466, Mar. 2021, doi: 10.1101/2021.03.22.436466.

[56] R. J. de Vries *et al.*, "Supercooling extends preservation time of human livers," *Nat. Biotechnol. 2019 3710*, vol. 37, no. 10, pp. 1131–1136, Sep. 2019, doi: 10.1038/s41587-019-0223-y.

[57] T. A. Berendsen *et al.*, "Supercooling enables long-term transplantation survival following 4 days of liver preservation," *Nat. Med. 2014 207*, vol. 20, no. 7, pp. 790–793, Jun. 2014, doi: 10.1038/nm.3588.

[58] E. N. Ashworth, G. A. Davis, and J. A. Anderson, "Factors Affecting Ice Nucleation in Plant Tissues," *Plant Physiol.*, vol. 79, no. 4, pp. 1033–1037, 1985, doi:

10.1104/pp.79.4.1033.

[59] T. Kang, Y. You, and S. Jun, "Supercooling preservation technology in food and biological samples: a review focused on electric and magnetic field applications," *Food Sci. Biotechnol. 2020 293*, vol. 29, no. 3, pp. 303–321, Jul. 2020, doi: 10.1007/S10068-020-00750-6.

[60] P. W. Wilson *et al.*, "Inhibition of ice nucleation by slippery liquid-infused porous surfaces (SLIPS)," *Phys. Chem. Chem. Phys.*, vol. 15, no. 2, pp. 581–585, Jan. 2013, doi: 10.1039/c2cp43586a.

[61] A. Safari, R. Saidur, F. A. Sulaiman, Y. Xu, and J. Dong, "A review on supercooling of Phase Change Materials in thermal energy storage systems," *Renew. Sustain. Energy Rev.*, vol. 70, pp. 905–919, Apr. 2017, doi: 10.1016/J.RSER.2016.11.272.

[62] S. Giwa *et al.*, "The promise of organ and tissue preservation to transform medicine," *Nature Biotechnology*, vol. 35, no. 6. Nature Publishing Group, pp. 530–542, Jun. 07, 2017. doi: 10.1038/nbt.3889.

[63] A. Ward, D. K. Klassen, K. M. Franz, S. Giwa, and J. K. Lewis, "Social, economic, and policy implications of organ preservation advances," *Current Opinion in Organ Transplantation*, vol. 23, no. 3. Lippincott Williams and Wilkins, pp. 336–346, Jun. 01, 2018. doi: 10.1097/MOT.0000000000000532.

[64] †,‡ B. Zobrist, ‡ T. Koop, † B. P. Luo, *,† and C. Marcolli, and T. Peter†, "Heterogeneous Ice Nucleation Rate Coefficient of Water Droplets Coated by a Nonadecanol Monolayer," *J. Phys. Chem. C*, vol. 111, no. 5, pp. 2149–2155, Feb. 2007, doi: 10.1021/JP066080W.

[65] P. C. Myint and J. L. Belof, "Rapid freezing of water under dynamic compression," *J. Phys. Condens. Matter*, vol. 30, no. 23, p. 233002, May 2018, doi: 10.1088/1361-648X/AAC14F.

[66] P. V. Hobbs, *Ice physics*. in Oxford classic texts in the physical sciences. New York: Oxford University Press, 2010.

[67] C. A. Angell, "Supercooled Water," *Ann. Rev. Phys. Chern*, vol. 34, pp. 593–630, 1983, Accessed: Aug. 03, 2021. [Online]. Available: www.annualreviews.org

[68] H. R. Pruppacher, "A New Look at Homogeneous Ice Nucleation in Supercooled Water Drops," *J. Atmos. Sci.*, vol. 52, no. 11, pp. 1924–1933, 1995, doi: 10.1175/1520-0469(1995)052<1924:ANLAHI>2.0.CO;2.

[69] T. Koop, B. Luo, A. Tsias, and T. Peter, "Water activity as the determinant for homogeneous ice nucleation in aqueous solutions," *Nat. 2000 4066796*, vol. 406, no. 6796, pp. 611–614, Aug. 2000, doi: 10.1038/35020537.

[70] O. Mishima and H. E. Stanley, "The relationship between liquid, supercooled and glassy water," *Nat. 1998 3966709*, vol. 396, no. 6709, pp. 329–335, Nov. 1998, doi: 10.1038/24540.

[71] B. J. Murray, D. O'sullivan, J. D. Atkinson, and M. E. Webb, "Ice nucleation by particles immersed in supercooled cloud droplets," *Chem. Soc. Rev.*, vol. 41, no. 19, pp. 6519–6554,

2012.

[72] D. A. Knopf and T. Koop, “Heterogeneous nucleation of ice on surrogates of mineral dust,” *J. Geophys. Res. Atmos.*, vol. 111, no. D12, p. 12201, Jun. 2006, doi: 10.1029/2005JD006894.

[73] Z. A. Kanji *et al.*, “Overview of Ice Nucleating Particles,” *Meteorol. Monogr.*, vol. 58, no. 1, pp. 1.1-1.33, Jan. 2017, doi: 10.1175/AMSMONOGRAPHS-D-16-0006.1.

[74] C. Budke and T. Koop, “BINARY: An optical freezing array for assessing temperature and time dependence of heterogeneous ice nucleation,” *Atmos. Meas. Tech.*, vol. 8, no. 2, pp. 689–703, Feb. 2015, doi: 10.5194/amt-8-689-2015.

[75] T. Koop and B. Zobrist, “Parameterizations for ice nucleation in biological and atmospheric systems,” *Phys. Chem. Chem. Phys.*, vol. 11, no. 46, pp. 10839–10850, Nov. 2009, doi: 10.1039/B914289D.

[76] R. A. Shaw, A. J. Durant, and Y. Mi, “Heterogeneous Surface Crystallization Observed in Undercooled Water,” *J. Phys. Chem. B*, vol. 109, no. 20, pp. 9865–9868, May 2005, doi: 10.1021/jp0506336.

[77] Y. S. Djikaev, A. Tabazadeh, P. Hamill, and H. Reiss, “Thermodynamic Conditions for the Surface-Stimulated Crystallization of Atmospheric Droplets,” *J. Phys. Chem. A*, vol. 106, no. 43, pp. 10247–10253, Oct. 2002, doi: 10.1021/jp021044s.

[78] A. Tabazadeh, Y. S. Djikaev, and H. Reiss, “Surface crystallization of supercooled water in clouds,” *Proc. Natl. Acad. Sci.*, vol. 99, no. 25, pp. 15873 LP – 15878, Dec. 2002, doi: 10.1073/pnas.252640699.

[79] H. Huang, M. L. Yarmush, and O. B. Usta, “Long-term deep-supercooling of large-volume water and red cell suspensions via surface sealing with immiscible liquids,” *Nat. Commun.*, vol. 9, no. 1, pp. 1–10, Dec. 2018, doi: 10.1038/s41467-018-05636-0.

[80] J. A. W. Elliott, “Surface thermodynamics at the nanoscale,” *J. Chem. Phys.*, vol. 154, no. 19, p. 190901, May 2021, doi: 10.1063/5.0049031.

[81] Y. Zhao *et al.*, “Phase change interface stability during isochoric solidification of an aqueous solution,” *Appl. Phys. Lett.*, vol. 117, no. 13, p. 133701, Sep. 2020, doi: 10.1063/5.0019878.

[82] A. Consiglio, G. Ukpai, B. Rubinsky, and M. J. Powell-Palm, “Suppression of cavitation-induced nucleation in systems under isochoric confinement,” *Phys. Rev. Lett.*, 2020.

[83] A. F. Heneghan, P. W. Wilson, G. Wang, and A. D. J. Haymet, “Liquid-to-crystal nucleation: Automated lag-time apparatus to study supercooled liquids,” *J. Chem. Phys.*, vol. 115, no. 16, pp. 7599–7608, 2001.

[84] D. Lilley, J. Lau, C. Dames, S. Kaur, and R. Prasher, “Impact of size and thermal gradient on supercooling of phase change materials for thermal energy storage,” *Appl. Energy*, vol. 290, p. 116635, May 2021, doi: 10.1016/j.apenergy.2021.116635.

[85] P. W. Wilson *et al.*, “Inhibition of ice nucleation by slippery liquid-infused porous surfaces

(SLIPS)," *Phys. Chem. Chem. Phys.*, vol. 15, no. 2, pp. 581–585, Dec. 2012, doi: 10.1039/C2CP43586A.

[86] P. Stöckel, I. M. Weidinger, H. Baumgärtel, and T. Leisner, "Rates of Homogeneous Ice Nucleation in Levitated H2O and D2O Droplets," *J. Phys. Chem. A*, vol. 109, no. 11, pp. 2540–2546, Mar. 2005, doi: 10.1021/jp047665y.

[87] G. R. Wood and A. G. Walton, "Homogeneous Nucleation Kinetics of Ice from Water," *J. Appl. Phys.*, vol. 41, no. 7, pp. 3027–3036, 1970, doi: 10.1063/1.1659359.

[88] N. E. Dorsey, "The Freezing of Supercooled Water," *Trans. Am. Philos. Soc.*, vol. 38, no. 3, pp. 247–328, 1948, [Online]. Available: http://www.jstor.org/stable/1005602

[89] A. F. Heneghan, P. W. Wilson, and A. D. J. Haymet, "Heterogeneous nucleation of supercooled water, and the effect of an added catalyst," *Proc. Natl. Acad. Sci.*, vol. 99, no. 15, pp. 9631–9634, 2002, doi: 10.1073/pnas.152253399.

[90] N. Reicher, L. Segev, and Y. Rudich, "The WeIzmann Supercooled Droplets Observation on a Microarray (WISDOM) and application for ambient dust," *Atmos. Meas. Tech.*, vol. 11, no. 1, pp. 233–248, Jan. 2018, doi: 10.5194/amt-11-233-2018.

[91] D. A. Knopf and P. A. Alpert, "A water activity based model of heterogeneous ice nucleation kinetics for freezing of water and aqueous solution droplets," *Faraday Discuss.*, vol. 165, no. 0, pp. 513–534, 2013, doi: 10.1039/C3FD00035D.

[92] P. A. Perez, J. Preciado, G. Carlson, R. DeLonzor, and B. Rubinsky, "The effect of undissolved air on isochoric freezing," *Cryobiology*, vol. 72, no. 3, pp. 225–231, Jun. 2016, doi: 10.1016/J.CRYOBIOL.2016.04.002.

[93] P. W. Wilson, A. F. Heneghan, and A. D. J. Haymet, "Ice nucleation in nature: supercooling point (SCP) measurements and the role of heterogeneous nucleation," *Cryobiology*, vol. 46, no. 1, pp. 88–98, Feb. 2003, doi: 10.1016/S0011-2240(02)00182-7.

[94] R. P. Sear, "Nucleation at contact lines where fluid-fluid interfaces meet solid surfaces," vol. 19, no. 46, p. 466106, Oct. 2007, doi: 10.1088/0953-8984/19/46/466106.

[95] A. Kar, A. Bhati, M. Lokanathan, and V. Bahadur, "Faster Nucleation of Ice at the Three-Phase Contact Line: Influence of Interfacial Chemistry," *Langmuir*, vol. 37, no. 43, pp. 12673–12680, Nov. 2021, doi: 10.1021/ACS.LANGMUIR.1C02044.

[96] J. Luengo-Márquez and L. G. MacDowell, "Lifshitz theory of wetting films at three phase coexistence: The case of ice nucleation on Silver Iodide (AgI)," *J. Colloid Interface Sci.*, vol. 590, pp. 527–538, May 2021, doi: 10.1016/J.JCIS.2021.01.060.

[97] T. F. Whale, M. A. Holden, T. W. Wilson, D. O'sullivan, and B. J. Murray, "The enhancement and suppression of immersion mode heterogeneous ice-nucleation by solutes," 2018, doi: 10.1039/c7sc05421a.

[98] A. P. MacKenzie, "Non-equilibrium freezing behaviour of aqueous systems," *Philos. Trans. R. Soc. London. B, Biol. Sci.*, vol. 278, no. 959, pp. 167–189, Mar. 1977, doi: 10.1098/RSTB.1977.0036.

[99] D. H. Rasmussen, "Thermodynamics and nucleation phenomena — A set of experimental observations," *J. Cryst. Growth*, vol. 56, no. 1, pp. 56–66, Jan. 1982, doi: 10.1016/0022-0248(82)90012-4.

[100] W. Que *et al.*, "Prolonged Cold Ischemia Time in Mouse Heart Transplantation Using Supercooling Preservation," *Transplantation*, pp. 1879–1889, 2020, doi: 10.1097/TP.0000000000003089.

[101] A. P. MacKenzie, "Non-equilibrium freezing behaviour of aqueous systems," *Philos. Trans. R. Soc. London. B, Biol. Sci.*, vol. 278, no. 959, pp. 167–189, Mar. 1977, doi: 10.1098/RSTB.1977.0036.

[102] K. E. Zachariassen, "Physiology of cold tolerance in insects," *https://doi.org/10.1152/physrev.1985.65.4.799*, vol. 65, no. 4, pp. 799–832, 1985, doi: 10.1152/PHYSREV.1985.65.4.799.

[103] W. Sun and G. Ceder, "Induction time of a polymorphic transformation," *CrystEngComm*, vol. 19, no. 31, pp. 4576–4585, Aug. 2017, doi: 10.1039/C7CE00766C.

[104] G. M. Maggioni and M. Mazzotti, "Stochasticity in Primary Nucleation: Measuring and Modeling Detection Times," *Cryst. Growth Des.*, vol. 17, no. 7, pp. 3625–3635, Jul. 2017, doi: 10.1021/ACS.CGD.6B01781.

[105] J. Bokeloh, R. E. Rozas, J. Horbach, and G. Wilde, "Nucleation Barriers for the Liquid-To-Crystal Transition in Ni: Experiment and Simulation," *Phys. Rev. Lett.*, vol. 107, no. 14, p. 145701, Sep. 2011, doi: 10.1103/PhysRevLett.107.145701.

[106] T. Kang, Y. You, and S. Jun, "Supercooling preservation technology in food and biological samples: a review focused on electric and magnetic field applications," *Food Sci Biotechnol*, vol. 29, no. 3, pp. 303–321, 2020.

[107] T. V. J. Charpentier, A. Neville, P. Millner, R. Hewson, and A. Morina, "An Investigation of Freezing of Supercooled Water on Anti-Freeze Protein Modified Surfaces," *J. Bionic Eng.*, vol. 10, no. 2, pp. 139–147, Apr. 2013.

[108] M. J. Powell-Palm, V. Charwat, B. Charrez, B. Siemons, K. E. Healy, and B. Rubinsky, "Isochoric supercooled preservation and revival of human cardiac microtissues," *Commun. Biol. 2021 41*, vol. 4, no. 1, pp. 1–7, Sep. 2021.

[109] L. Wan, M. J. Powell-Palm, M. G. Clemens, and B. Rubinsky, "Time-dependent Effects of Pressure during Preservation of Rat Hearts in an Isochoric System at Subfreezing Temperatures," *Cryo Letters*, vol. 40, no. 1, pp. 64–70, Jan. 2019.

[110] M. J. Powell-Palm, B. Rubinsky, and W. Sun, "Freezing water at constant volume and under confinement," *Commun. Phys.*, vol. 3, no. 1, pp. 1–8, Feb. 2020.

[111] M. J. Powell-Palm, A. Koh-Bell, and B. Rubinsky, "Isochoric conditions enhance stability of metastable supercooled water," *Appl. Phys. Lett.*, vol. 116, no. 12, p. 123702, Mar. 2020.

[112] A. Consiglio, D. Lilley, R. Prasher, B. Rubinsky, and M. J. Powell-Palm, "Methods to stabilize aqueous supercooling identified by use of an isochoric nucleation detection (INDe)

device," *arXiv*, p. 2108.10404, Aug. 2021.

[113] N. Kimizuka and T. Suzuki, "Supercooling Behavior in Aqueous Solutions," *J. Phys. Chem. B*, vol. 111, no. 9, pp. 2268–2273, 2007.

[114] N. Kimizuka, C. Viriyarattanasak, and T. Suzuki, "Ice nucleation and supercooling behavior of polymer aqueous solutions," *Cryobiology*, vol. 56, no. 1, pp. 80–87, Feb. 2008.

[115] V. D. Alves *et al.*, "Rheological and morphological characterization of the culture broth during exopolysaccharide production by Enterobacter sp.," *Carbohydr. Polym.*, vol. 81, no. 4, pp. 758–764, Jul. 2010.

[116] F. Freitas *et al.*, "Controlled Production of Exopolysaccharides from Enterobacter A47 as a Function of Carbon Source with Demonstration of Their Film and Emulsifying Abilities," *Appl. Biochem. Biotechnol. 2013 1722*, vol. 172, no. 2, pp. 641–657, Oct. 2013.

[117] B. M. Guerreiro, F. Freitas, J. C. Lima, J. C. Silva, M. Dionísio, and M. A. M. Reis, "Demonstration of the cryoprotective properties of the fucose-containing polysaccharide FucoPol," *Carbohydr. Polym.*, vol. 245, p. 116500, Oct. 2020.

[118] B. M. Guerreiro *et al.*, "Development of a Cryoprotective Formula Based on the Fucose-Containing Polysaccharide FucoPol," *ACS Appl. Bio Mater.*, vol. 4, no. 6, pp. 4800–4808, Jun. 2021.

[119] C. A. V. Torres *et al.*, "Rheological studies of the fucose-rich exopolysaccharide FucoPol," *Int. J. Biol. Macromol.*, vol. 79, pp. 611–617, Aug. 2015.

[120] F. Freitas *et al.*, "Fucose-containing exopolysaccharide produced by the newly isolated Enterobacter strain A47 DSM 23139," *Carbohydr. Polym.*, vol. 83, no. 1, pp. 159–165, Jan. 2011.

[121] C. B. Marshall, A. Chakrabartty, and P. L. Davies, "Hyperactive Antifreeze Protein from Winter Flounder Is a Very Long Rod-like Dimer of α-Helices," *J. Biol. Chem.*, vol. 280, no. 18, pp. 17920–17929, May 2005.

[122] C. R. Shurer *et al.*, "Physical Principles of Membrane Shape Regulation by the Glycocalyx," *Cell*, vol. 177, no. 7, pp. 1757-1770.e21, Jun. 2019.

[123] D. Lilley, J. Lau, C. Dames, S. Kaur, and R. Prasher, "Impact of size and thermal gradient on supercooling of phase change materials for thermal energy storage," *Appl. Energy*, vol. 290, p. 116635, May 2021.

[124] T. Chang and G. Zhao, "Ice Inhibition for Cryopreservation: Materials, Strategies, and Challenges," *Adv. Sci.*, vol. 8, no. 6, p. 2002425, Mar. 2021.

[125] G. L. Fletcher, C. L. Hew, and P. L. Davies, "Antifreeze Proteins of Teleost Fishes," *Annu. Rev. Physiol.*, vol. 63, pp. 359–390, 2001.

[126] C. A. V. Torres *et al.*, "Kinetics of production and characterization of the fucose-containing exopolysaccharide from Enterobacter A47," *J. Biotechnol.*, vol. 156, no. 4, pp. 261–267, Dec. 2011.

BIBLIOGRAPHY

[127] A. R. V. Ferreira, C. A. V. Torres, F. Freitas, M. A. M. Reis, V. D. Alves, and I. M. Coelhoso, "Biodegradable films produced from the bacterial polysaccharide FucoPol," *Int. J. Biol. Macromol.*, vol. 71, pp. 111–116, Nov. 2014.

[128] K. M. C. Tjørve and E. Tjørve, "The use of Gompertz models in growth analyses, and new Gompertz-model approach: An addition to the Unified-Richards family," *PLoS One*, vol. 12, no. 6, p. e0178691, Jun. 2017.

[129] S. M. Gaber, A.-G. Johansen, S. B. Skeie, E.-O. Rukke, and R. B. Schüller, "Analysis of Rheological Time Series Data," *Annu. Trans. Nord. Rheol. Soc.*, vol. 27, pp. 127–131, 2019.

[130] P. W. Wilson and A. D. J. Haymet, "The Spread of Nucleation Temperatures of a Sample of Supercooled Liquid Is Independent of the Average Nucleation Temperature," *J. Phys. Chem. B*, vol. 116, no. 45, pp. 13472–13475, Nov. 2012.

[131] S. Mercier, S. Villeneuve, M. Mondor, and I. Uysal, "Time–Temperature Management Along the Food Cold Chain: A Review of Recent Developments," *Compr. Rev. Food Sci. Food Saf.*, vol. 16, pp. 647–667, 2017.

[132] W. Dou, MJ; Lu, CN; Rao, W; Dou, Mengjia; Lu, Chennan; Rao, "Bioinspired materials and technology for advanced cryopreservation," *Trends Biotechnol.*, vol. 40, no. 1, pp. 93–106, 2022.

[133] T. Arutyunyan, I; Elchaninov, A; Fatkhudinov, T; Arutyunyan, Irina; Elchaninov, Andrey; Sukhikh, Gennady; Fatkhudinov, "Cryopreservation of Tissue-Engineered Scaffold-Based Constructs: from Concept to Reality," *Stem Cell Rev. Reports*, p. https://doi.org/10.1007/s12015-021-10299-4, 2021.

[134] C. Polge, A. U. Smith, and A. S. Parkes, "Revival of spermatozoa after vitrification and dehydration at low temperatures. ," *Nature*, vol. 164, no. 4172, p. 666, 1949, doi: 10.1038/164666a0.

[135] P. Mazur, "Freezing of living cells: mechanisms and implications," *Am. J. Physiol. Physiol.*, vol. 247, no. 3, pp. C125–C142, 1984, doi: 10.1152/ajpcell.1984.247.3.C125.

[136] M. J. Powell-Palm, V. Charwat, B. Charrez, B. Siemons, K. E. Healy, and B. Rubinsky, "Isochoric supercooled preservation and revival of human cardiac microtissues," *Commun. Biol. 2021 41*, vol. 4, no. 1, pp. 1–7, Sep. 2021, doi: 10.1038/s42003-021-02650-9.

[137] G.-P. Park, DH; Lee, S; Hong, GP; Park, Dong Hyeon; Lee, SangYoon; Lee, Jiseon; Kim, Eun Jeong; Jo, Yeon-Ji; Kim, Honggyun; Choi, Mi-Jung; Hong, "Stepwise cooling mediated feasible supercooling preservation to extend freshness of mackerel fillets," *LWT-Food Sci. Technol.*, vol. 152, p. 112389, 2021.

[138] J. F. Gillooly, J. H. Brown, G. B. West, V. M. Savage, and E. L. Charnov, "Effects of size and temperature on metabolic rate," *Science (80-.).*, vol. 293, no. 5538, pp. 2248–2251, Sep. 2001, doi: 10.1126/science.1061967.

[139] V. L. Arcus *et al.*, "On the Temperature Dependence of Enzyme-Catalyzed Rates," *Biochemistry*, vol. 55, no. 12, pp. 1681–1688, Mar. 2016, doi: 10.1021/ACS.BIOCHEM.5B01094/SUPPL_FILE/BI5B01094_SI_001.PDF.

[140] A. Consiglio, D. Lilley, R. Prasher, B. Rubinsky, and M. J. Powell-Palm, "Methods to stabilize aqueous supercooling identified by use of an isochoric nucleation detection (INDe) device," Aug. 2021, Accessed: Jan. 10, 2022. [Online]. Available: https://arxiv.org/abs/2108.10404v1

[141] R. V. Devireddy, D. J. Smith, and J. C. Bischof, "Effect of Microscale Mass Transport and Phase Change on Numerical Prediction of Freezing in Biological Tissues," *J. Heat Transfer*, vol. 124, no. 2, pp. 365–374, Apr. 2002, doi: 10.1115/1.1445134.

[142] T. Acharya and R. V. Devireddy, "Cryomicroscopic Investigations of Freezing Processes in Cell Suspensions," *Open Biotechnol. J.*, vol. 4, no. 1, pp. 26–35, May 2010, doi: 10.2174/1874070701004010026.

[143] B. C. Goh, S. Thirumala, G. Kilroy, R. V. Devireddy, and J. M. Gimble, "Cryopreservation characteristics of adipose-derived stem cells: maintenance of differentiation potential and viability," *J. Tissue Eng. Regen. Med.*, vol. 1, no. 4, pp. 322–324, Jul. 2007, doi: 10.1002/TERM.35.

[144] D. Turnbull, "Kinetics of Solidification of Supercooled Liquid Mercury Droplets," *J. Chem. Phys.*, vol. 20, no. 3, pp. 411–424, 1952, doi: 10.1063/1.1700435.

[145] V. P. Skripov, V. P. Koverda, and G. T. Butorin, "Crystal Nucleation Kinetics in Small Volumes," in *Рост Кристаллов / Rost Kristallov / Growth of Crystals: Volume 11*, A. A. Chernov, Ed., Boston, MA: Springer US, 1979, pp. 22–25. doi: 10.1007/978-1-4615-7113-1_3.

[146] C. W. Morton, W. H. Hofmeister, R. J. Bayuzick, and M. B. Robinson, "A statistical approach to understanding nucleation phenomena," *Mater. Sci. Eng. A*, vol. 178, no. 1–2, pp. 209–215, Apr. 1994, doi: 10.1016/0921-5093(94)90545-2.

[147] A. Filipponi, A. Di Cicco, and E. Principi, "Crystalline nucleation in undercooled liquids: A Bayesian data-analysis approach for a nonhomogeneous Poisson process," *Phys. Rev. E - Stat. Nonlinear, Soft Matter Phys.*, vol. 86, no. 6, p. 066701, Dec. 2012, doi: 10.1103/PHYSREVE.86.066701/FIGURES/11/MEDIUM.

[148] T. Koop, B. Luo, U. M. Biermann, P. J. Crutzen, and T. Peter, "Freezing of HNO3/H2SO4/H2O Solutions at Stratospheric Temperatures: Nucleation Statistics and Experiments," *J. Phys. Chem. A*, vol. 101, no. 6, pp. 1117–1133, Feb. 1997, doi: 10.1021/JP9626531.

[149] V. I. Kalikmanov, "Classical Nucleation Theory," in *Nucleation Theory*, Dordrecht: Springer Netherlands, 2013, pp. 17–41. doi: 10.1007/978-90-481-3643-8_3.

[150] K. F. Kelton and A. L. Greer, "Chapter 2 - The Classical Theory," in *Nucleation in Condensed Matter*, K. F. Kelton and A. L. Greer, Eds., in Pergamon Materials Series, vol. 15. Pergamon, 2010, pp. 19–54. doi: https://doi.org/10.1016/S1470-1804(09)01502-8.

[151] N. Kubota, "Analysis of the effect of volume on induction time and metastable zone width using a stochastic model," *J. Cryst. Growth*, vol. 418, pp. 15–24, May 2015, doi: 10.1016/J.JCRYSGRO.2015.02.021.

[152] R. W. Salt, “Principles of Insect Cold-Hardiness,” *Annu. Rev. Entomol.*, vol. 6, no. 1, pp. 55–74, Jan. 1961, doi: 10.1146/annurev.en.06.010161.000415.

[153] B. M. Barnes, “Freeze Avoidance in a Mammal: Body Temperatures Below 0°C in an Arctic Hibernator,” *Science (80-.).*, vol. 244, no. 4912, pp. 1593–1595, 1989, doi: 10.1126/SCIENCE.2740905.

[154] M. Dalvi-Isfahan, N. Hamdami, E. Xanthakis, and A. Le-Bail, “Review on the control of ice nucleation by ultrasound waves, electric and magnetic fields,” *J. Food Eng.*, vol. 195, pp. 222–234, 2017, doi: https://doi.org/10.1016/j.jfoodeng.2016.10.001.

[155] F. Franks and M. Jones, “Biophysics and biochemistry at low temperatures,” *FEBS Lett.*, vol. 220, no. 2, p. 391, Aug. 1987, doi: https://doi.org/10.1016/0014-5793(87)80854-2.

[156] J. K. Lewis *et al.*, “The Grand Challenges of Organ Banking: Proceedings from the first global summit on complex tissue cryopreservation,” *Cryobiology*, vol. 72, no. 2, pp. 169–182, 2016, doi: https://doi.org/10.1016/j.cryobiol.2015.12.001.

[157] R. J. de Vries *et al.*, “Supercooling extends preservation time of human livers,” *Nat. Biotechnol.*, vol. 37, no. 10, pp. 1131–1136, Oct. 2019, doi: 10.1038/s41587-019-0223-y.

[158] C. A. Angell, “Supercooled Water,” *Water Aqueous Solut. Subzero Temp.*, pp. 1–81, 1982, doi: 10.1007/978-1-4757-6952-4_1.

[159] S. L. Broadley *et al.*, “Immersion mode heterogeneous ice nucleation by an illite rich powder representative of atmospheric mineral dust,” *Atmos. Chem. Phys.*, vol. 12, no. 1, pp. 287–307, 2012, doi: 10.5194/acp-12-287-2012.

[160] R. J. Herbert, B. J. Murray, T. F. Whale, S. J. Dobbie, and J. D. Atkinson, “Representing time-dependent freezing behaviour in immersion mode ice nucleation,” *Atmos. Chem. Phys.*, vol. 14, no. 16, pp. 8501–8520, 2014, doi: 10.5194/acp-14-8501-2014.

[161] C. Marcolli, S. Gedamke, T. Peter, and B. Zobrist, “Efficiency of immersion mode ice nucleation on surrogates of mineral dust,” *Atmos. Chem. Phys.*, vol. 7, no. 19, pp. 5081–5091, 2007, doi: 10.5194/acp-7-5081-2007.

[162] B. J. Murray, S. L. Broadley, T. W. Wilson, J. D. Atkinson, and R. H. Wills, “Heterogeneous freezing of water droplets containing kaolinite particles,” *Atmos. Chem. Phys.*, vol. 11, no. 9, pp. 4191–4207, 2011, doi: 10.5194/acp-11-4191-2011.

[163] L.-T. Deck and M. Mazzotti, “Characterizing and measuring the ice nucleation kinetics of aqueous solutions in vials,” *Chem. Eng. Sci.*, vol. 272, p. 118531, 2023, doi: https://doi.org/10.1016/j.ces.2023.118531.

[164] R. P. Sear, “On the Interpretation of Quantitative Experimental Data on Nucleation Rates Using Classical Nucleation Theory,” *J. Phys. Chem. B*, vol. 110, no. 43, pp. 21944–21949, Nov. 2006, doi: 10.1021/JP064692A.

[165] R. P. Sear, “Statistical theory of nucleation in the presence of uncharacterized impurities,” *Phys. Rev. E*, vol. 70, no. 2, p. 21605, Aug. 2004, doi: 10.1103/PhysRevE.70.021605.

[166] R. P. Sear, “Non-self-averaging nucleation rate due to quenched disorder,” *J. Phys.*

Condens. Matter, vol. 24, no. 5, p. 52205, 2012, doi: 10.1088/0953-8984/24/5/052205.

[167] M. A. Holden *et al.*, "High-speed imaging of ice nucleation in water proves the existence of active sites," *Sci. Adv.*, vol. 5, no. 2, Feb. 2019, doi: 10.1126/sciadv.aav4316.

[168] J. M. Campbell, F. C. Meldrum, and H. K. Christenson, "Observing the formation of ice and organic crystals in active sites," *Proc. Natl. Acad. Sci. U. S. A.*, vol. 114, no. 5, pp. 810–815, Jan. 2017, doi: 10.1073/pnas.1617717114.

[169] A. Taloni, M. Vodret, G. Costantini, and S. Zapperi, "Size effects on the fracture of microscale and nanoscale materials," *Nat. Rev. Mater.*, vol. 3, no. 7, pp. 211–224, 2018, doi: 10.1038/s41578-018-0029-4.

[170] E. Castillo, "Extreme value theory in engineering," p. 389, 1988.

[171] J. Levine, "STATISTICAL EXPLANATION OF SPONTANEOUS FREEZING OF WATER DROPLETS," 1950.

[172] R. P. Sear, "Generalisation of Levine's prediction for the distribution of freezing temperatures of droplets: A general singular model for ice nucleation," *Atmos. Chem. Phys.*, vol. 13, no. 14, pp. 7215–7223, Jul. 2013, doi: 10.5194/ACP-13-7215-2013.

[173] E. J. Langham and B. J. Mason, "The heterogeneous and homogeneous nucleation of supercooled water," *Proc. R. Soc. London. Ser. A. Math. Phys. Sci.*, vol. 247, no. 1251, pp. 493–504, Oct. 1958, doi: 10.1098/RSPA.1958.0207.

[174] W. E. Bardsley and M. M. Khatep, "A General Model for Temperature of Heterogeneous Nucleation of Supercooled Water Droplets," *J. Atmos. Sci.*, vol. 41, no. 5, pp. 856–862, Mar. 1984, doi: 10.1175/1520-0469(1984)041<0856:AGMFTO>2.0.CO;2.

[175] R. P. Sear, "Quantitative studies of crystal nucleation at constant supersaturation: experimental data and models," *CrystEngComm*, vol. 16, no. 29, pp. 6506–6522, Jul. 2014, doi: 10.1039/C4CE00344F.

[176] A. N. Consiglio, D. Lilley, R. Prasher, B. Rubinsky, and M. J. Powell-Palm, "Methods to stabilize aqueous supercooling identified by use of an isochoric nucleation detection (INDe) device," *Cryobiology*, 2022, doi: 10.1016/j.cryobiol.2022.03.003.

[177] A. Consiglio, G. Ukpai, B. Rubinsky, and M. J. Powell-Palm, "Suppression of cavitation-induced nucleation in systems under isochoric confinement," *Phys. Rev. Res.*, vol. 2, no. 2, p. 023350, Jun. 2020, doi: 10.1103/PhysRevResearch.2.023350.

[178] M. J. Powell-Palm, A. Koh-Bell, and B. Rubinsky, "Isochoric conditions enhance stability of metastable supercooled water," *Appl. Phys. Lett.*, vol. 116, no. 12, p. 123702, Mar. 2020, doi: 10.1063/1.5145334.

[179] S. F. Mathias, F. Franks, and K. Trafford, "Nucleation and growth of ice in deeply undercooled erythrocytes," *Cryobiology*, vol. 21, no. 2, pp. 123–132, Jun. 1984, doi: 10.1016/0011-2240(84)90203-7.

[180] M. Toner, E. G. Cravalho, and M. Karel, "Thermodynamics and kinetics of intracellular ice formation during freezing of biological cells," *J. Appl. Phys.*, vol. 67, no. 3, pp. 1582–1593,

Feb. 1990, doi: 10.1063/1.345670.

[181] B. G. Pummer, H. Bauer, J. Bernardi, S. Bleicher, and H. Grothe, "Suspendable macromolecules are responsible for ice nucleation activity of birch and conifer pollen," *Atmos. Chem. Phys.*, vol. 12, no. 5, pp. 2541–2550, 2012, doi: 10.5194/acp-12-2541-2012.

[182] D. Kashchiev, *Nucleation basic theory with applications* . Oxford ; Butterworth-Heinemann, 2000.

[183] B. Zobrist, T. Koop, B. P. Luo, C. Marcolli, and T. Peter, "Heterogeneous ice nucleation rate coefficient of water droplets coated by a nonadecanol monolayer," *J. Phys. Chem. C*, vol. 111, no. 5, pp. 2149–2155, Feb. 2007, doi: 10.1021/JP066080W/ASSET/IMAGES/LARGE/JP066080WF00004.JPEG.

[184] L. Ickes, A. Welti, and U. Lohmann, "Classical nucleation theory of immersion freezing: sensitivity of contact angle schemes to thermodynamic and kinetic parameters," *Atmos. Chem. Phys.*, vol. 17, no. 3, pp. 1713–1739, 2017, doi: 10.5194/acp-17-1713-2017.

[185] P. V. Hobbs, *Ice physics*. Oxford: Clarendon Press, 1974.

[186] J. D. Hoffman, "Thermodynamic driving force in nucleation and growth processes," *The Journal of Chemical Physics*, vol. 29, no. 5. American Institute of PhysicsAIP, pp. 1192–1193, Nov. 13, 1958. doi: 10.1063/1.1744688.

[187] R. G. Wylie, "The Freezing of Supercooled Water in Glass," *Proc. Phys. Soc. Sect. B*, vol. 66, no. 3, p. 241, Mar. 1953, doi: 10.1088/0370-1301/66/3/311.

[188] Y. Diao, A. S. Myerson, T. A. Hatton, and B. L. Trout, "Surface Design for Controlled Crystallization: The Role of Surface Chemistry and Nanoscale Pores in Heterogeneous Nucleation," *Langmuir*, vol. 27, no. 9, pp. 5324–5334, May 2011, doi: 10.1021/la104351k.

[189] A. D. Harrison *et al.*, "Not all feldspars are equal: a survey of ice nucleating properties across the feldspar group of minerals," *Atmos. Chem. Phys.*, vol. 16, no. 17, pp. 10927–10940, 2016, doi: 10.5194/acp-16-10927-2016.

[190] L. Eickhoff *et al.*, "Ice nucleation in aqueous solutions of short- and long-chain poly(vinyl alcohol) studied with a droplet microfluidics setup," *J. Chem. Phys.*, vol. 158, no. 15, p. 154504, Apr. 2023, doi: 10.1063/5.0136192.

[191] C. W. Gurganus, J. C. Charnawskas, A. B. Kostinski, and R. A. Shaw, "Nucleation at the Contact Line Observed on Nanotextured Surfaces," *Phys. Rev. Lett.*, vol. 113, no. 23, p. 235701, Dec. 2014, doi: 10.1103/PhysRevLett.113.235701.

[192] R. Sear, "What do crystals nucleate on? What is the microscopic mechanism? How can we model nucleation?," *MRS Bull.*, vol. 41, no. 5, pp. 363–368, May 2016, doi: 10.1557/MRS.2016.88.

[193] I. De Almeida Ribeiro, K. Meister, and V. Molinero, "HUB: A method to model and extract the distribution of ice nucleation temperatures from drop-freezing experiments," *ChemRxiv*, Mar. 2023, doi: 10.26434/CHEMRXIV-2022-DDZV8-V3.

[194] E. J. Gumbel, *Statistics of extremes* , Dover edit. Mineola, N.Y: Dover Publications, 2004.

[195] R. P. Sear, "Estimation of the scaling of the nucleation time with volume when the nucleation rate does not exist," *Cryst. Growth Des.*, vol. 13, no. 3, pp. 1329–1333, Mar. 2013, doi: 10.1021/CG301849F/ASSET/IMAGES/MEDIUM/CG-2012-01849F_0004.GIF.

[196] P. W. Wilson and A. D. J. Haymet, "The spread of nucleation temperatures of a sample of supercooled liquid is independent of the average nucleation temperature," *J. Phys. Chem. B*, vol. 116, no. 45, pp. 13472–13475, Nov. 2012, doi: 10.1021/jp308177b.

[197] E. J. Gumbel and C. K. Mustafi, "Some Analytical Properties of Bivariate Extremal Distributions," *J. Am. Stat. Assoc.*, vol. 62, no. 318, pp. 569–588, Jun. 1967, doi: 10.1080/01621459.1967.10482930.

[198] N. Balakrishna and C. D. Lai, "Bivariate Extreme-Value Distributions BT - Continuous Bivariate Distributions: Second Edition," C. D. Lai and N. Balakrishnan, Eds., New York, NY: Springer New York, 2009, pp. 563–590. doi: 10.1007/b101765_13.

[199] J. Beirlant, Y. Goegebeur, J. Teugels, and J. Segers, *Statistics of Extremes*. in Wiley Series in Probability and Statistics. Wiley, 2004. doi: 10.1002/0470012382.

[200] G. Vali, "Repeatability and randomness in heterogeneous freezing nucleation," *Atmos. Chem. Phys.*, vol. 8, no. 16, pp. 5017–5031, Aug. 2008, doi: 10.5194/ACP-8-5017-2008.

[201] G. Vali, "Interpretation of freezing nucleation experiments: singular and stochastic; sites and surfaces," *Atmos. Chem. Phys.*, vol. 14, no. 11, pp. 5271–5294, 2014, doi: 10.5194/acp-14-5271-2014.

[202] J. Deubener and J. W. P. Schmelzer, "Statistical Approach to Crystal Nucleation in Glass-Forming Liquids," *Entropy 2021, Vol. 23, Page 246*, vol. 23, no. 2, p. 246, Feb. 2021, doi: 10.3390/E23020246.

[203] D. Turnbull, "Kinetics of heterogeneous nucleation," *J. Chem. Phys.*, vol. 18, no. 2, pp. 198–203, Feb. 1950, doi: 10.1063/1.1747588.

[204] E. K. Bigg, "The Supercooling of Water," *Proc. Phys. Soc. Sect. B*, vol. 66, no. 8, p. 688, Aug. 1953, doi: 10.1088/0370-1301/66/8/309.

[205] E. K. Bigg, "The formation of atmospheric ice crystals by the freezing of droplets," *Q. J. R. Meteorol. Soc.*, vol. 79, no. 342, pp. 510–519, Oct. 1953, doi: 10.1002/QJ.49707934207.

[206] S. C. Mossop, "The Freezing of Supercooled Water," *Proc. Phys. Soc. Sect. B*, vol. 68, no. 4, p. 193, Apr. 1955, doi: 10.1088/0370-1301/68/4/301.

[207] D. Barahona, "Analysis of the effect of water activity on ice formation using a new thermodynamic framework," *Atmos. Chem. Phys.*, vol. 14, no. 14, pp. 7665–7680, 2014, doi: 10.5194/acp-14-7665-2014.

[208] D. Barahona, "Thermodynamic derivation of the activation energy for ice nucleation," *Atmos. Chem. Phys.*, vol. 15, no. 24, pp. 13819–13831, 2015, doi: 10.5194/acp-15-13819-2015.

[209] D. Barahona, "On the thermodynamic and kinetic aspects of immersion ice nucleation,"

BIBLIOGRAPHY

Atmos. Chem. Phys., vol. 18, no. 23, pp. 17119–17141, 2018, doi: 10.5194/acp-18-17119-2018.